General Disclaimer

One or more of the Following Statements may affect this Document

- This document has been reproduced from the best copy furnished by the organizational source. It is being released in the interest of making available as much information as possible.

- This document may contain data, which exceeds the sheet parameters. It was furnished in this condition by the organizational source and is the best copy available.

- This document may contain tone-on-tone or color graphs, charts and/or pictures, which have been reproduced in black and white.

- This document is paginated as submitted by the original source.

- Portions of this document are not fully legible due to the historical nature of some of the material. However, it is the best reproduction available from the original submission.

MEASUREMENTS OF THE SURFACE ENERGY BUDGET IN THE SOUTHERN GOBI DESERT OF CHINA, AND IN THE ROCKY MOUNTAINS OF COLORADO

Elmar R. Reiter, Principal Investigator

Eric A. Smith and John D. Sheaffer

Department of Atmospheric Science
Colorado State University
Fort Collins, CO 80523

Progress Report
NASA Grant NAGW601
for Period
February 15, 1984 to February 28, 1985

ABSTRACT

Observations of the land surface energy balance were made in the Gobi desert and at two mountain sites in northern Colorado. The Gobi study included 12 days of observations in spring (April 8-20, 1984) and 31 days in summer at the same site (June 17-July 18, 1984). The Colorado study included 126 days (March 13-July 17, 1984) at a valley site and 34 days (July 31-September 3, 1984) at a mountain top location. The data for each study included continuous observations of upward and downward radiative fluxes in three wave bands, soil temperature and moisture at four levels, air temperature and humidity at four levels and UVW wind components at three levels. Analyses of the Gobi data include definition of the impact of variable atmospheric moisture on the surface energy balance between spring and summer. In addition, diurnal wind circulations forced by heating of the northern edge of the Tibetan Plateau were observed during both periods. The measurements in northern Colorado also document the variable effects of atmospheric moisture on the radiative flux components as well as strong differences in subsurface heat and moisture fluxes, effects of snow cover, surface litter, and relatively localized adiabatic heating and cooling in response to terrain forced circulations. Unexpected results in the Colorado data include the failure to observe typical diurnal (valley) wind circulations at the valley site and the occurrence of a very pronounced diurnal wind cycle at the mountain top site. Several deficiencies in the configuration of the turbulent flux monitors diminished the quality of these measurements and precluded closure of the energy budgets in the preliminary data. These problems and recent remedial actions are described in a critique of the flux monitoring systems.

1.0 INTRODUCTION

This report summarizes three 1984 data collection programs funded by NASA Grant NAGW-601. These programs included detailed measurement and analyses of surface energy fluxes in the Gobi Desert and at two remote locations in the Rocky Mountains of northern Colorado. Section 2.0 contains a summary of the Gobi experiment and a brief description of the monitoring procedures. The monitoring systems are described in detail in Appendix A. The Gobi report also includes an extended display of the various types of data collected and the methods of analysis being used. Observations for both Rocky Mountain sites are described in Section 3.0. Although this section emphasizes comparative analyses of conditions at the two sites, intercomparisons between these and the Gobi data are presently limited to only a few variables. A critical review of the performance of the monitoring systems and a description of several modifications currently being made are given in Section 4.0.

2.0 THE GOBI EXPERIMENT: INTRODUCTION

Measurements of the surface energy budget were conducted during the spring and summer of 1984 in the western Gobi desert near the northern flank of the Tibetan Plateau in Gansu Province, P.R.C. The experimental site for the Gobi study is located near the village of Zhangye [38°55'N; 100°28'E] at an elevation of approximately 1500 meters. This experiment served as a field test of a specialized set of surface instrumentation which will be deployed at three sites on the Tibetan Plateau in the summer of 1985. Measurements from these stations will be used to diagnose the surface energy budget and structure of the lower boundary layer of the plateau during summer. This site was chosen on the basis of

its proximity to the plateau and because the desert characteristics of the western Gobi are, in part, maintained by the vertical circulations driven by the elevated heat source associated with the plateau. The data presented in this report are part of a much larger data base that is being collected by investigators at U.S. and Chinese Scientific institutions as part of a cooperative science and technology program established by the National Science Agencies of the two countries.

The Gobi experiment involved a scientific team from Colorado State University, lead by E.R. Reiter and a Chinese team from the Institute of Plateau Physics, lead by Professor You-Xi Gao. A member of Professor Reiter's team, Professor E.A. Smith is now affiliated with the Department of Meteorology at Florida State University; he will continue to participate in the Tibetan field phase and follow-up data analysis phase under a coordinated research plan.

2.1 Design of Experiment

The Gobi experiment was designed to investigate the nature of the surface energetics of the western Gobi including the temporal variations and diurnally averaged properties of three key components. These include: (1) radiative exchange processes; (2) heat/moisture storage processes; and (3) sensible and latent heat exchange between the ground and the atmosphere. There are definite constraints which govern field measurement procedures in desert and plateau environments. These constraints, in turn, limit the possibilities for measuring and calculating components of the surface energy budget and, in conjunction with the measurements and calculations, establish the limits of accuracy in the final retrieval of surface exchange terms. Hence, a secondary objective was the testing of various combinations of sensors and numerical methodologies to optimally retrieve these terms in remote terrain.

The constraints that we have been guided by are the necessity of using low cost, but fully automated measurement stations, which require no external power sources to drive either the sensors or the data-logging/recording devices, which employ easily maintained and relatively uncomplicated sensors, and which are portable and can be deployed by no more than two people. Furthermore, the measurement systems have to be able to withstand a harsh environment. In meeting these requirements we have developed a dual station monitoring system which utilizes a combination of conventional sensors of modest to high performance standards, and incorporates relatively sophisticated data logging/data reduction electronics which interface to standard tape cassette recording units for archiving and follow-up computer anaysis.

The present system is configured in two parts - a radiation, rainfall, wind, state parameters, and subsurface heat and moisture monitoring station (referred to hereafter as the Radiation Station), and a 4-level tower eddy flux monitoring station (hereafter referred to as the Tower Station). Schematic illustrations of the Radiation Station and the Tower Station are provided in Figs. 1 and 2. All sensors on the two systems are interfaced with programmable, microprocessor-driven data loggers which periodically record their memory contents onto conventional cassette tape recorders. The data logger and recording electronics are powered by rechargeable battery packs which, during sunny conditions, are charged by single-panel solar energy collector-converter systems marketed by Campbell Scientific Incorporated (CSI). Complete descriptions of the flux monitoring systems and data processing procedures are given in Appendix A.

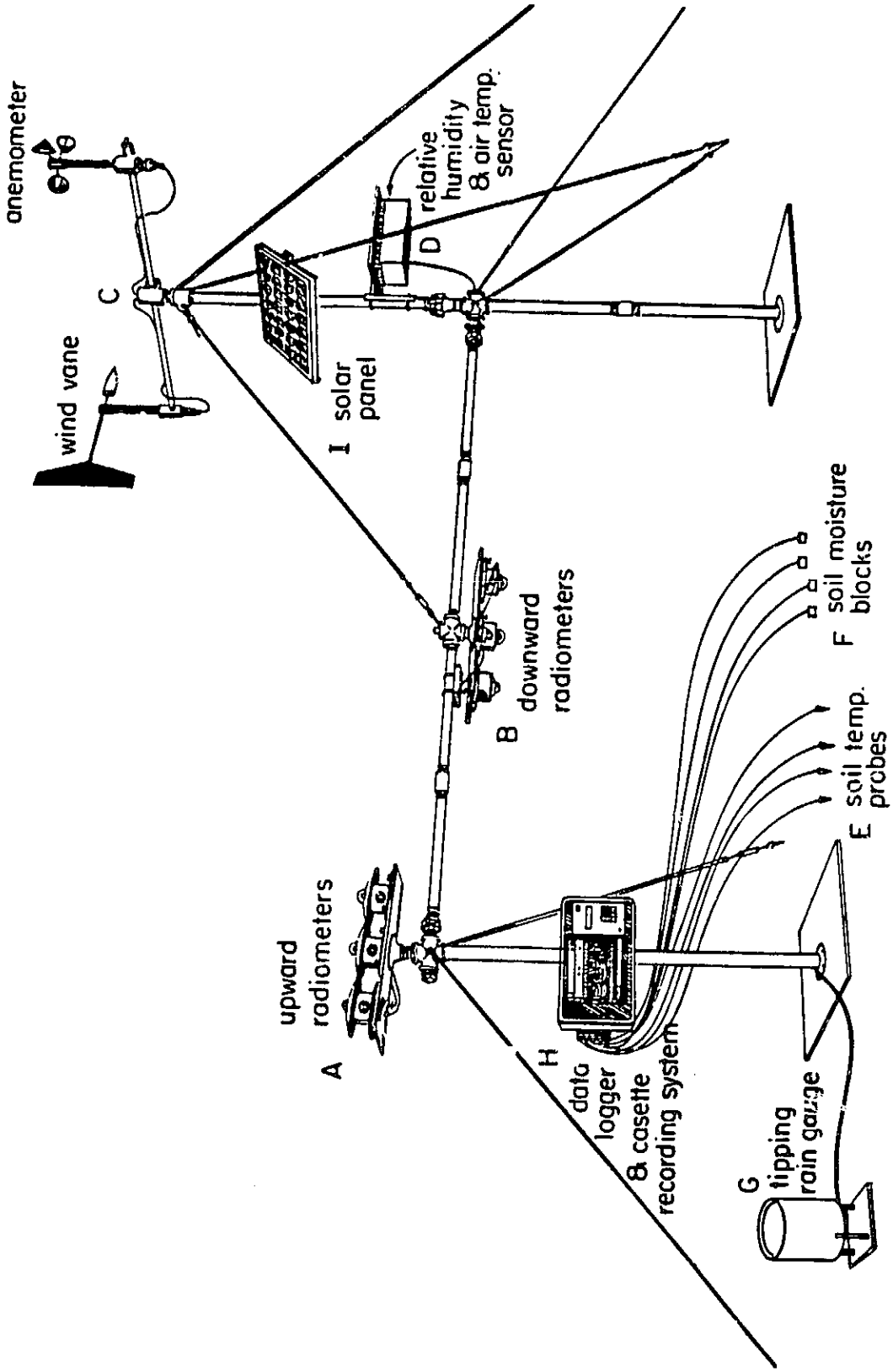

Fig. 1 Schematic illustration of the Radiation Station.

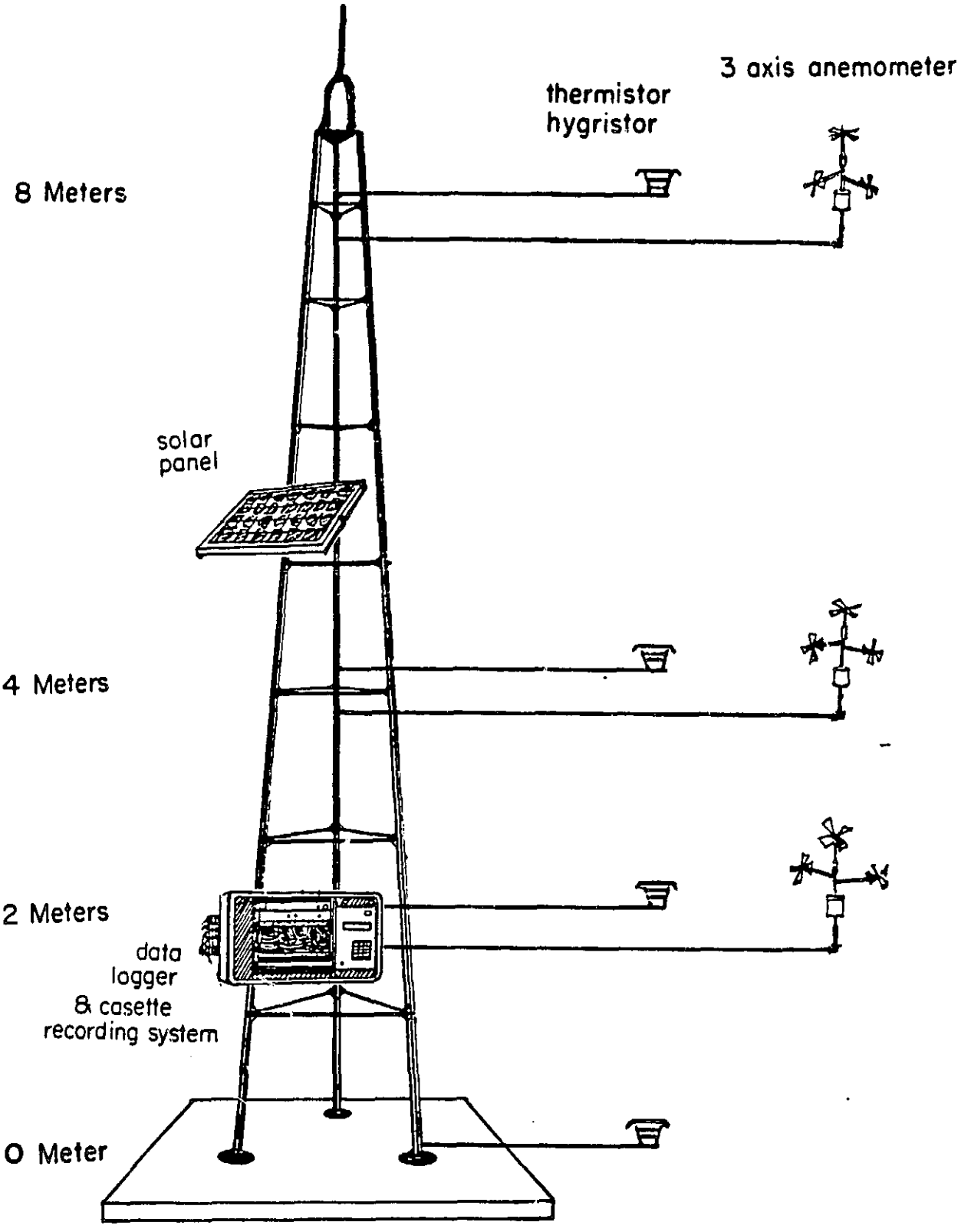

Fig. 2 Schematic illustration of the Tower Station.

2.2 Analysis of Spring and Summer Data

a. Site Conditions

The results in this section were compiled during two intensive data collection periods. THe first measurement period took place in spring [April 8 to April 20], the second took place in summer [June 17 - July 18]. Conditions at the Gobi site during the spring period included generally clear skies with intermittent high cirrus, extensive wind blown dust, and low humidities with no detectable precipitation. The nights were cold and early morning temperatures would occasionally fall below 0°C. Nevertheless, surface heating was significant as the combination of dry convection and mechanical turbulence served to trigger frequent dust devils. Figures 3 and 4 show the conditions around the site; note that there is sparse scrub vegetation and a large portion of the surface was covered with small pebbles. Chinese shepherds would drive their flocks over this area to gain access to the Tibetan Plateau foothills. The lack of clarity of the Plateau silhouette in Fig. 3c is due to the heavy dust loading in the desert boundary layer.

During the summer period there was intermittent cloudiness and light rain showers. The dust loading in the boundary layer diminished whereas atmospheric moisture increased dramatically. In the following sections the surface conditions and energy budgets of the spring and summer periods are discussed.

b. Surface Thermodynamic Conditions

The primary difference between the spring and summer periods is the increase in boundary layer moisture. Figure 5 shows diurnal air temperature (AT)-relative humidity (RH) traces for the spring and summer periods. The mean RH in spring of approximately 25 percent was

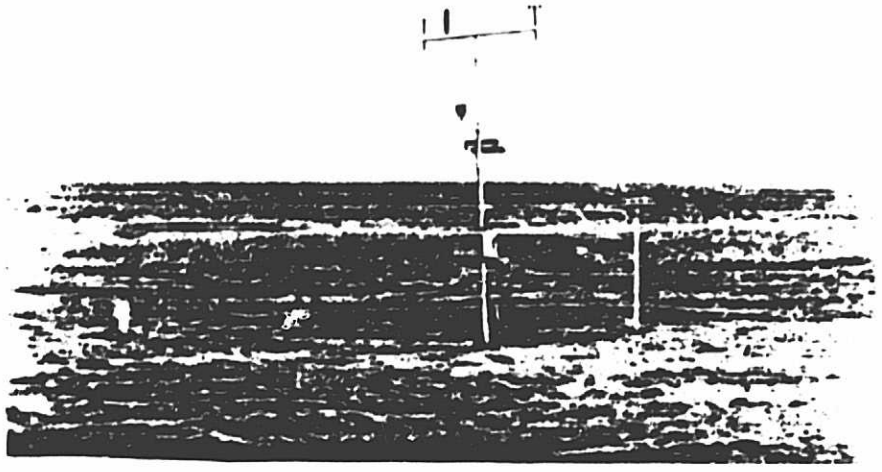

Figure 3a. A view to the east of the desert terrain centered on the Radiation Station. The electronics package is about 3 feet above ground attached to the main station support. The rain gauge is to the left of the photo.

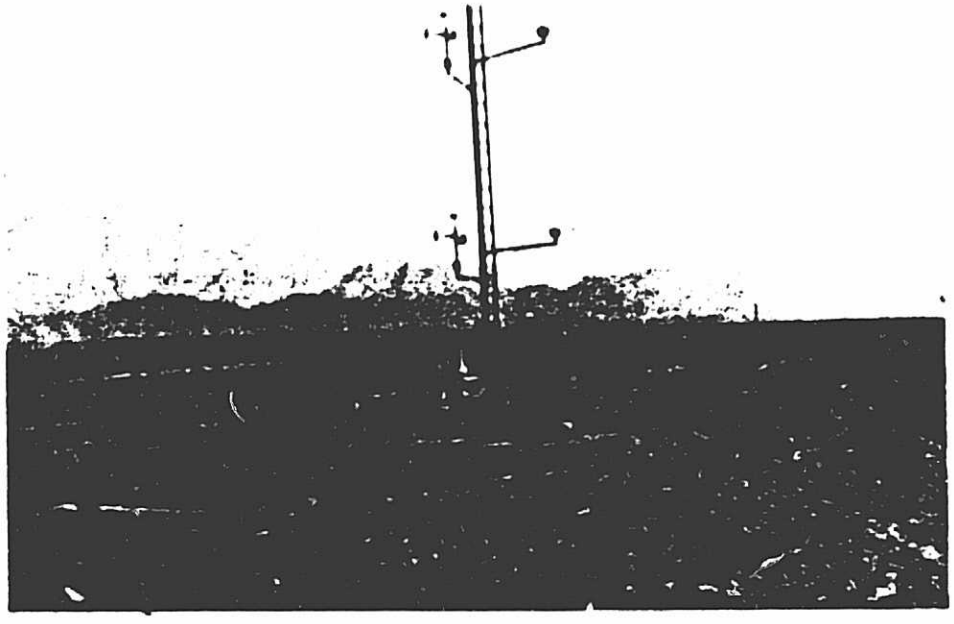

Figure 3b. A view to the southeast centered on the Tower Station. The Tibetan Plateau is visible in the background although obscured by the heavy dust loading in the boundary layer.

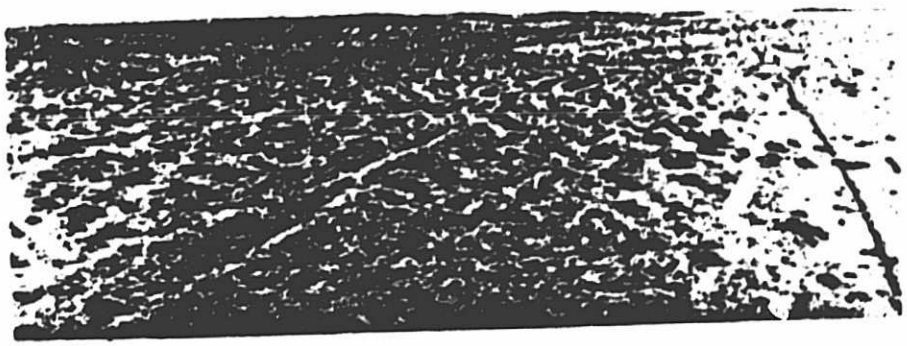

Figure 4. A view to the southeast about 300 km from the observational site showing a herd of sheep grazing on desert scrub.

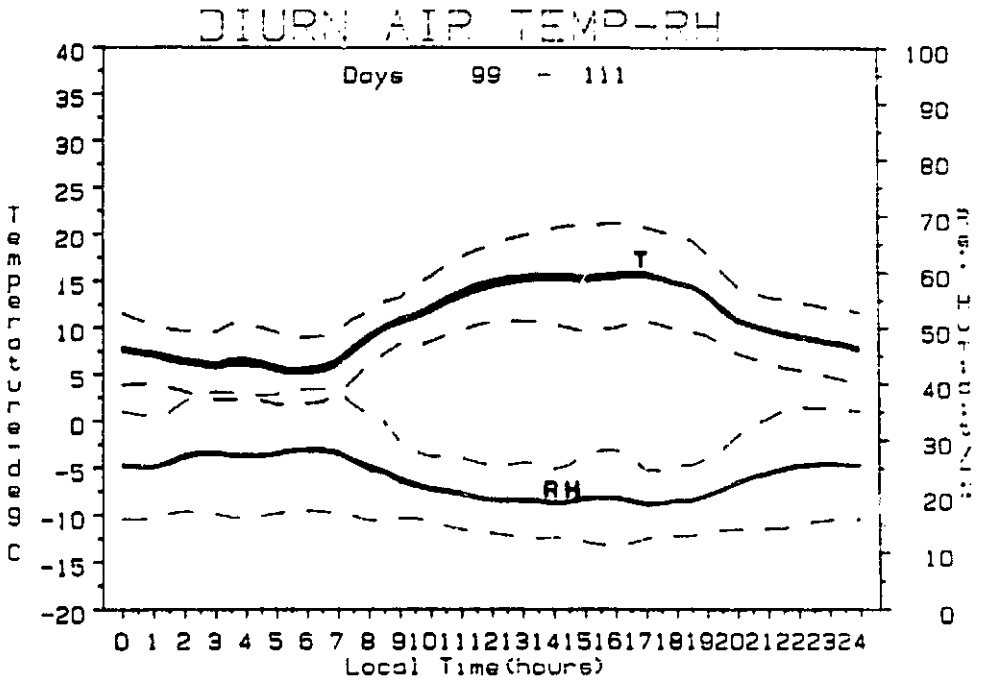

Figure 5a. Diurnal air temperature (T) and relative humidity (RH) for spring period--RH is the lower trace. The traces are plotted along with the ±one-sigma "local" standard-deviation characterizing diurnal turbulence (solid lines) and the ±one-sigma diurnal standard-deviation lines characterizing natural diurnal variability.

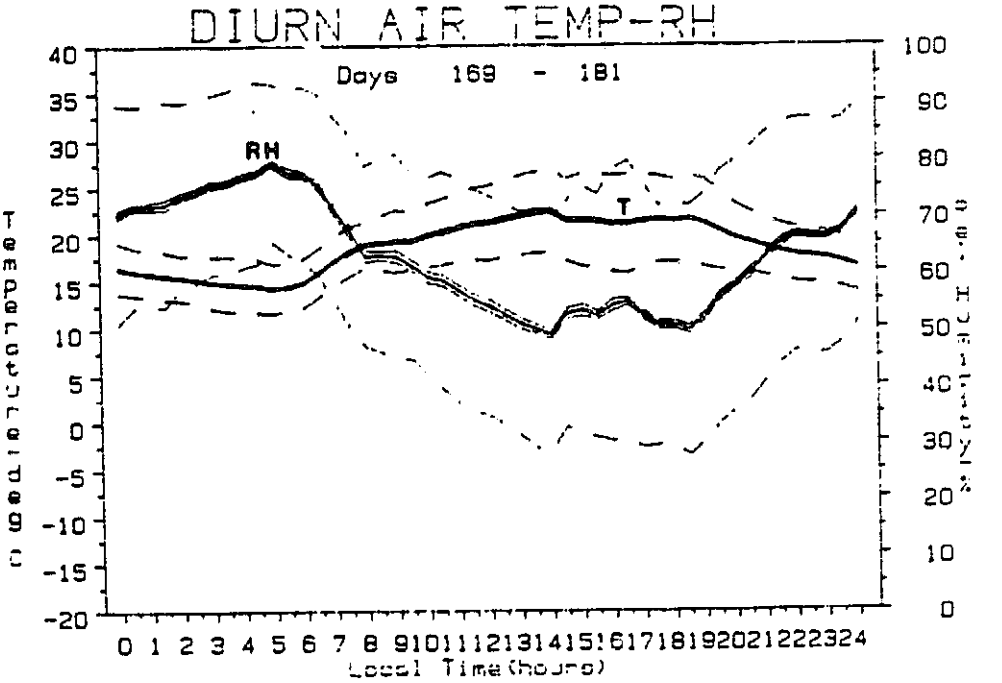

Figure 5b. As in Fig. 5a but for summer period (the RH trace is concave and intersects the T trace at early morning and early evening).

associated with daily air temperatures of approximately 10°C. During the summer period humidities were on the order of 60 percent and mean daily air temperatures were approximately 20°C. In Figure 6, the diurnal mixing ratio curves associated with these AT-RH functions are shown. Springtime values vary between 2.0-2.5 $gm \cdot kg^{-1}$ with little evidence of a diurnal fluctuation. Summer levels are on the order of 10-11 $gm \cdot kg^{-1}$ with a slight dirunal cycle (nighttime minimum and late night maximum).

The time series of 15-minute measurements that were used to composite the diurnal plots provide a glimpse of both the diurnal regularity of the Gobi desert environment and also the rather interesting extremes that characterize the region. These time series are shown in Figure 7. Note in Fig. 7b, for example, that humidities range from ten percent up to saturation during this two week summer period. The springtime period, on the other hand, appears less variable.

c. Surface Wind Conditions

There is a pronounced diurnal slope effect on surface winds in the Zhangye region. Figures 8 and 9 demonstrates that in both the spring and summer periods, plateau heating appears to reverse the sign of the v-component of the surface wind from a downslope nighttime flow to an upslope daytime flow. The u-component of the surface wind maintains a westerly direction throughout most of the day, shifting to weak easterly flow during a continued portion of the upslope period (mid-day in spring; morning in summer). The scalar wind speed plots in Fig. 10 illustrate that at the two nodes when north-south flow changes sign (early morning and late afternoon), there are momentary lulls in the total wind. Plotted along with the scalar diurnal wind speed are two

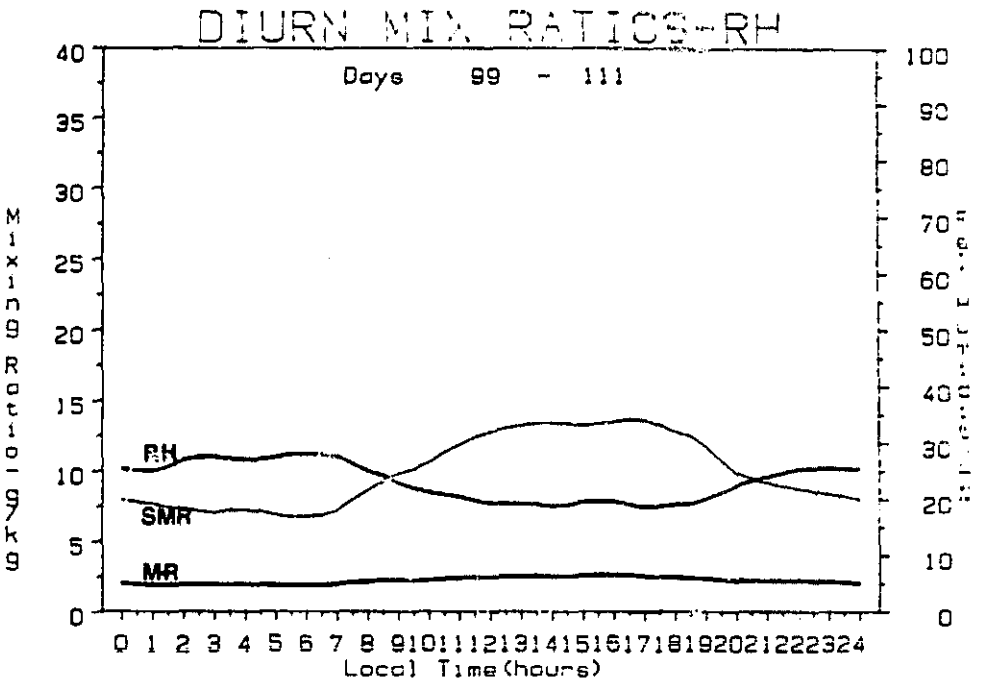

Figure 6a. Spring period diurnal mixing ratio (MR), saturation mixing ratio (SMR), and relative humidity.

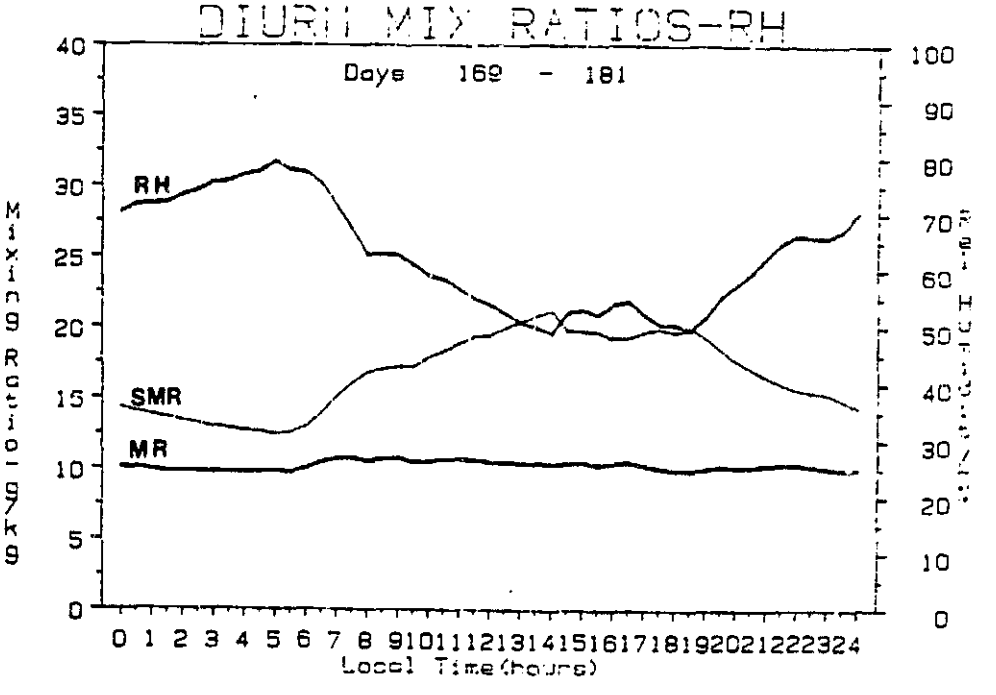

Figure 6b. As in Fig. 6a but for summer period.

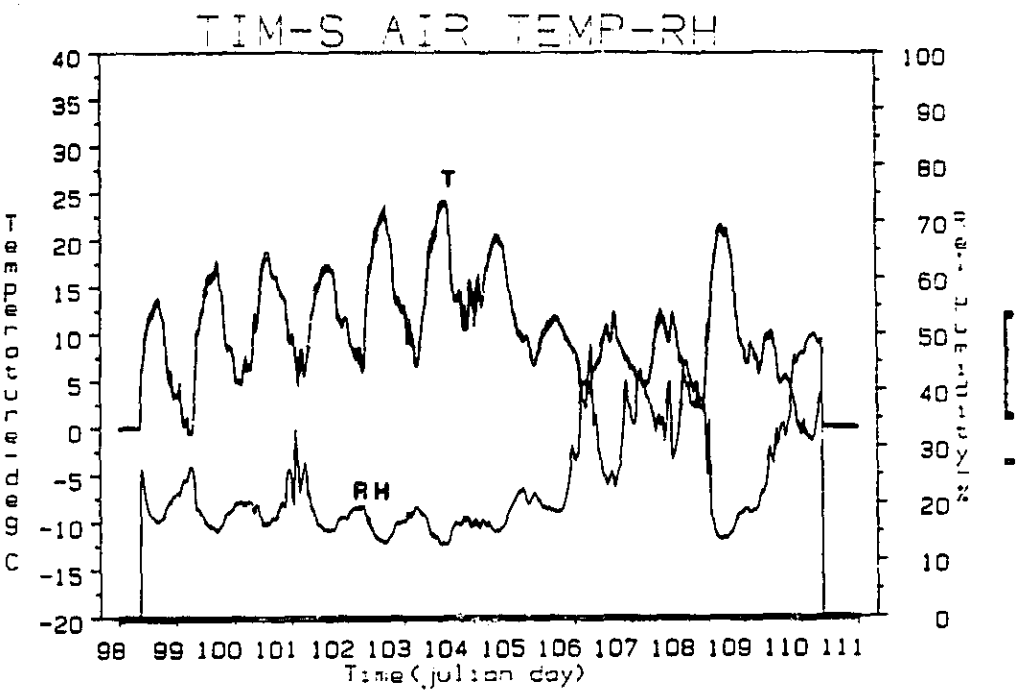

Figure 7a. Time series of air temperature and relative humidity for the spring period.

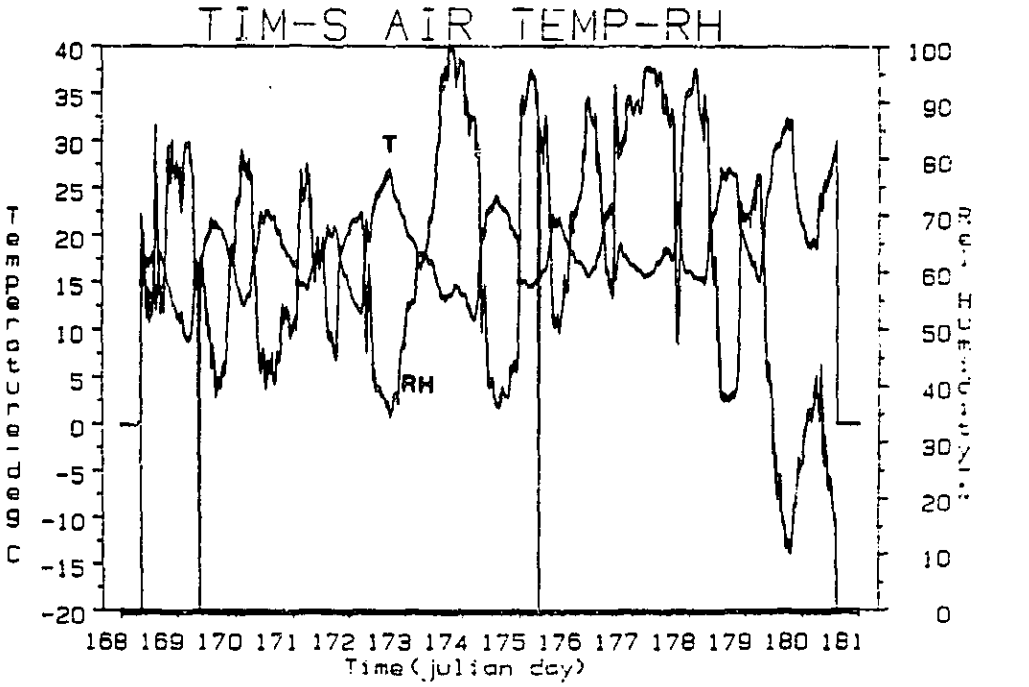

Figure 7b. As in Fig. 7a but for summer period.

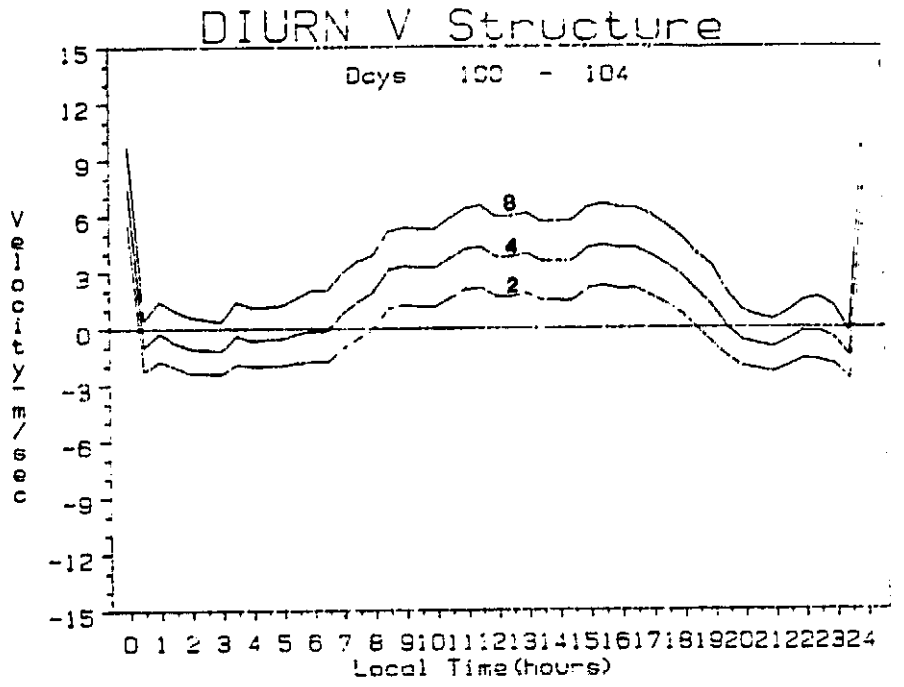

Figure 8a. Diurnally-averaged v-component of the surface wind at three tower levels (2.0, 4.0, 8.0 meters) during a five-day spring period. In order to distinguish the plots, the 4.0 meter has 2.0 $m \cdot sec^{-1}$ added to it; the 8.0 meter trace has 4.0 $m \cdot sec^{-1}$ added to it.

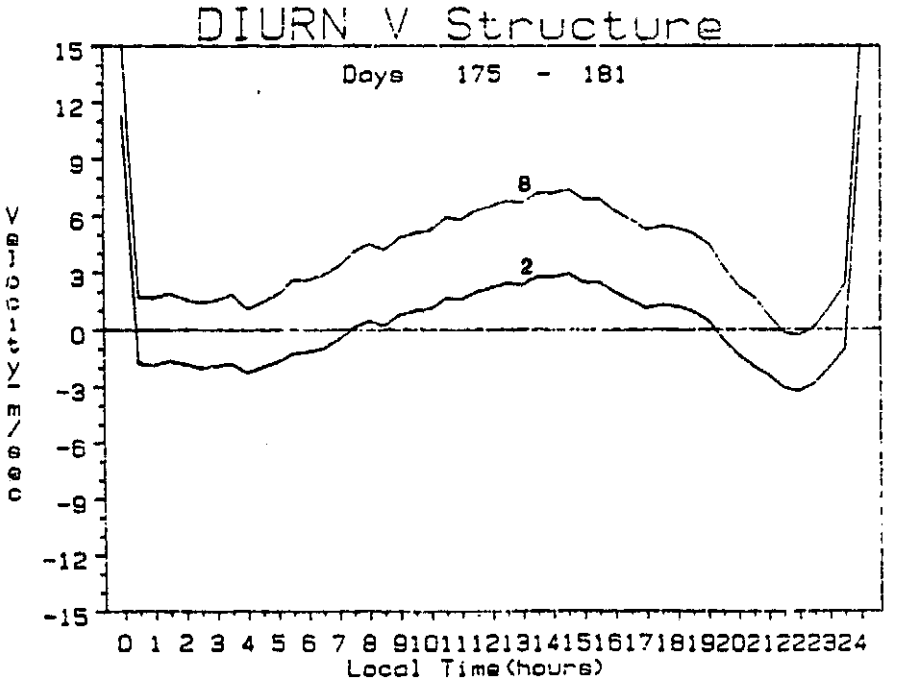

Figure 8b. As in Fig. 8a but for seven-day summer period (only the 2.0 and 8.0 meter traces are shown).

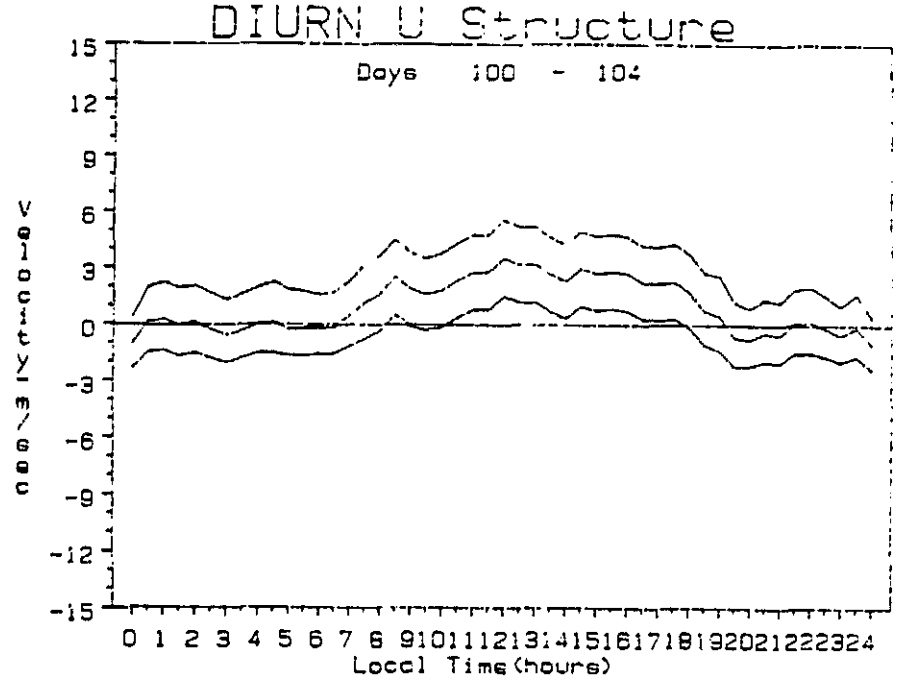

Figure 9a. As in Fig. 8a but for u-component.

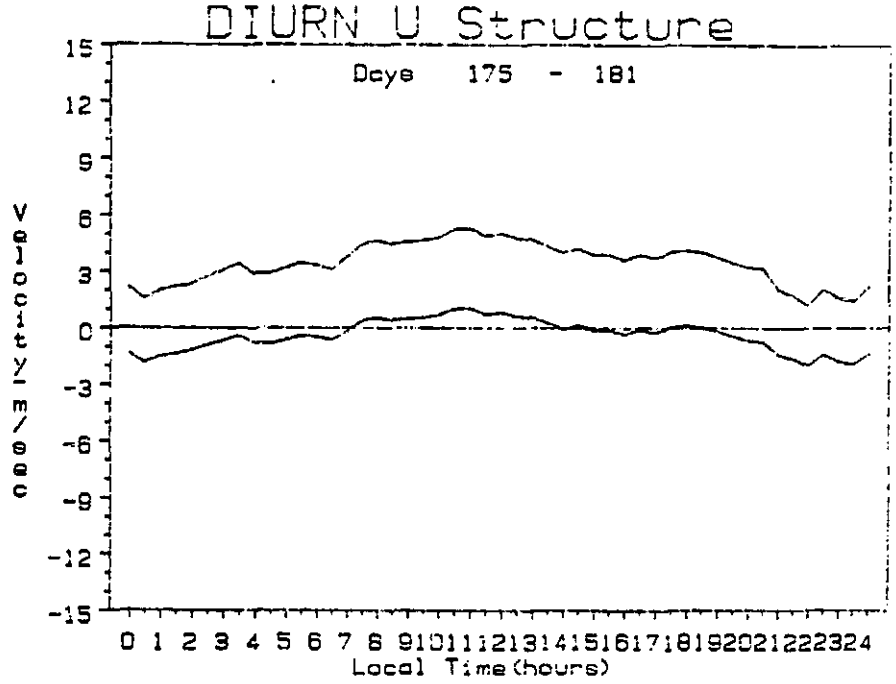

Figure 9b. As in Fig. 8b but for u-component.

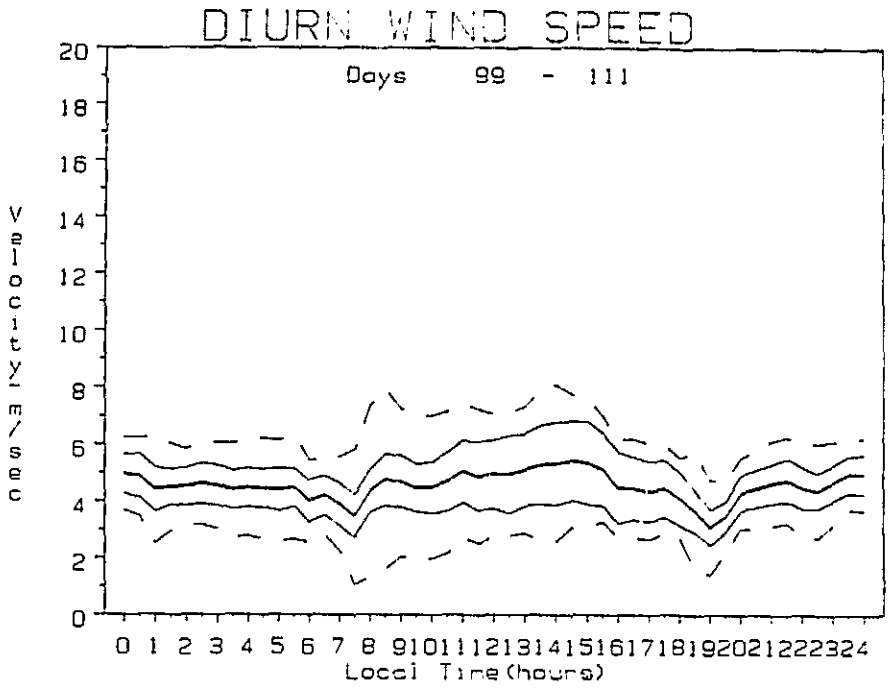

Figure 10a. Diurnally-averaged wind speed from the radiation station (3 meters) along with ±one "local" standard deviation lines (solid) and "diurnal period" standard deviation lines (dashed).

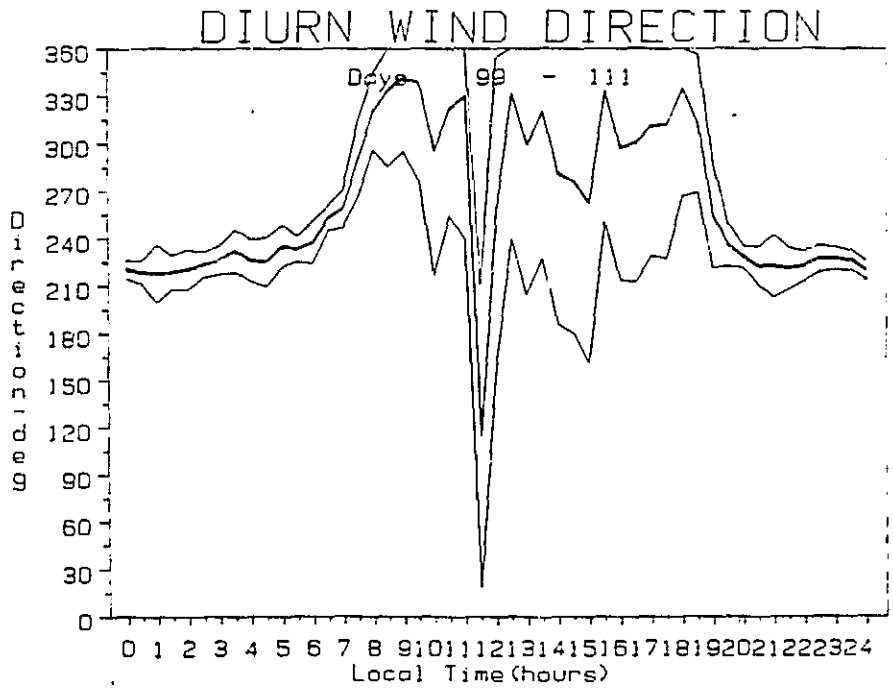

Figure 10b. Diurnally-averaged wind direction from radiation station.

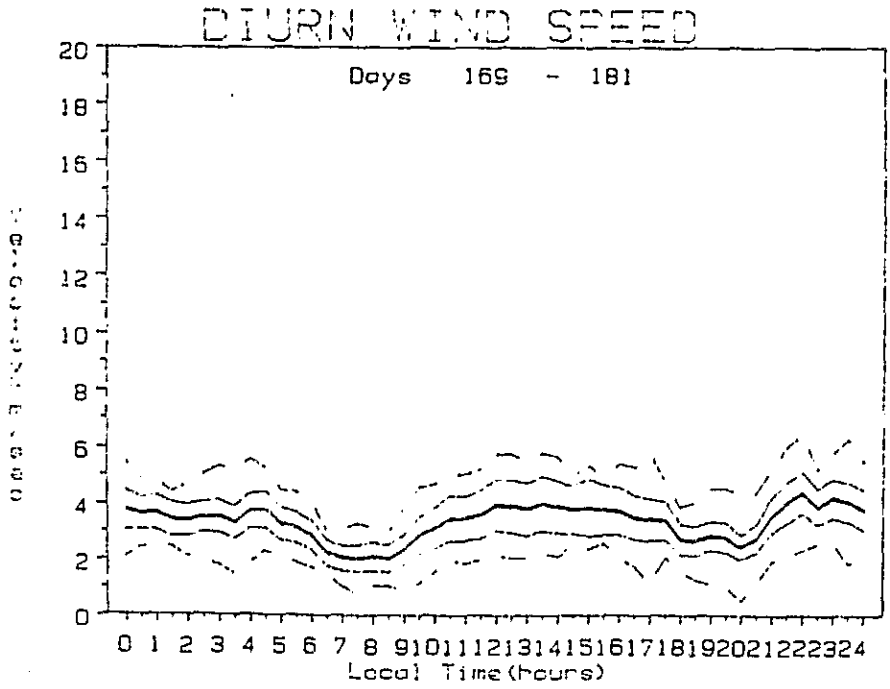

Figure 10c. As in Fig. 10a but for summer period.

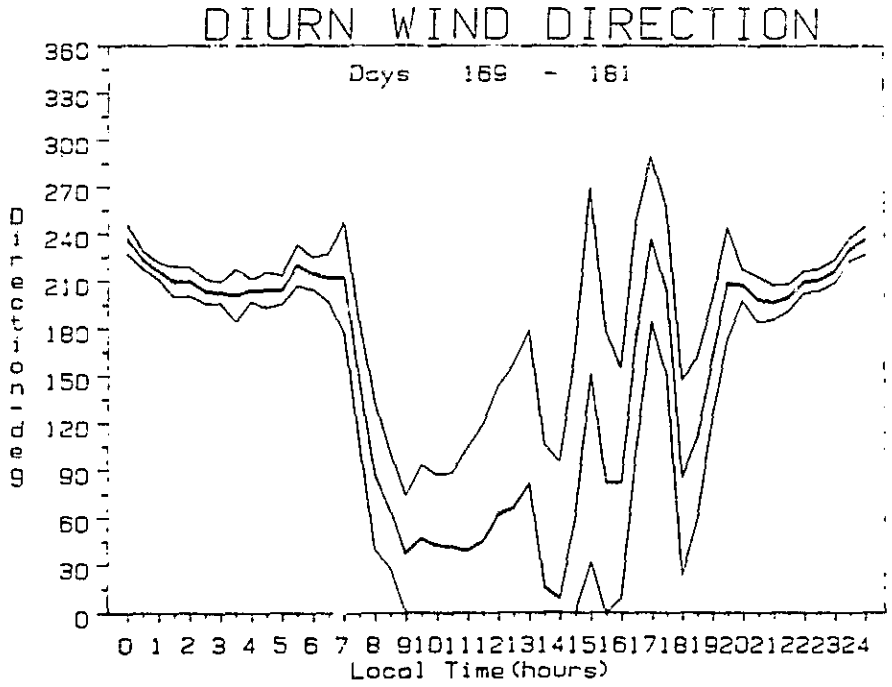

Figure 10d. As in Fig. 10b but for summer period.

sets of ±one standard deviation (sigma) lines. The first set (solid lines) illustrates the diurnally averaged local standard deviation, where "local" implies the standard deviation for a 15-minute observation. The dashed lines, illustrate the diurnal standard deviation, derived from the samples used to construct a diurnal average (i.e., the first statistical moment about a single diurnal mean value). Note that the "local" variability of wind speed presented in diurnally-averaged form, is approximately half of the total variability over a diurnal averaging period for any given time of day. The ratio of these two terms provides a signature of the degree of inter-diurnal kinetic energy variation due to local turbulence, since the "local" standard deviation is effectively a measure of turbulent fluctuations in the wind field. Diurnally-averaged wind direction from the radiation station (Fig. 10) also illustrates these same effects. Note that whereas the spring winds tend to veer to the northwest during the morning hours, the summer winds back to the northeast.

d. Surface Radiation Budget

The surface radiation budget of the western Gobi exhibits distinct differences between the spring and summer periods. These differences are shown in Figs. 11-18. Figure 11 illustrates diurnal plots of upward and downward solar and terrestrial flux terms for the two periods. The major difference is that during spring conditions, when the heavy dust layer is still in evidence, the near-infrared (0.7-3.0 μm) insolation term is notably greater than the shortwave (0.2-0.7 μm) insolation term. The dust layer serves to reflect shortwave energy back to space, a portion of which would otherwise go into surface heating. During summer conditions, the two insolation terms are effectively equal. (Assuming

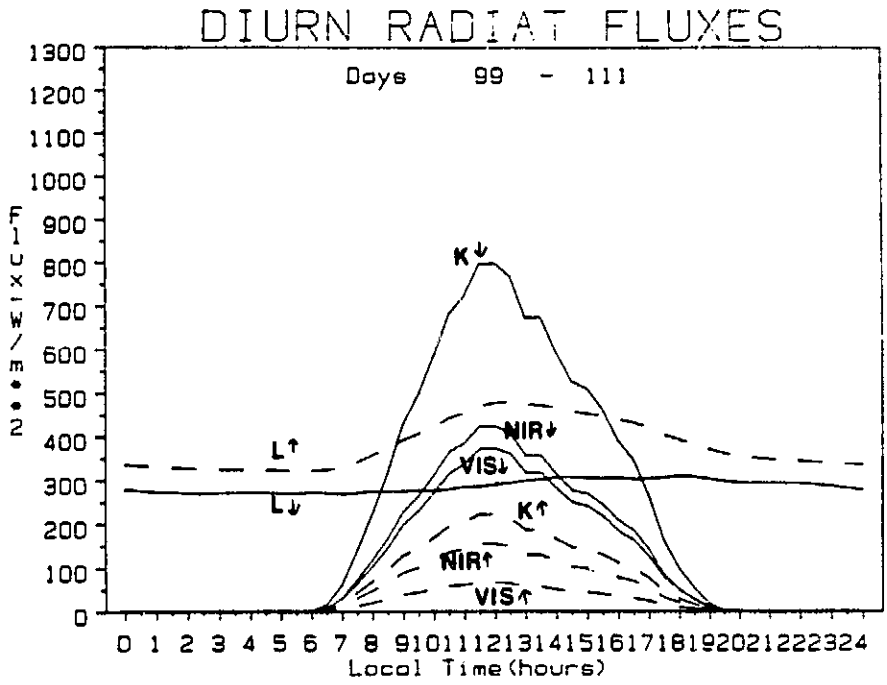

Figure 11a. Diurnally-averaged solar and terrestrial radiation fluxes in both the upward and downward direction for spring. The solar terms are in order from largest to smallest, total downward (K↓), near IR downward (NIR↓), shortwave downward (VIS↓), total upward (K↑), near-IR upward (NIR↑), and shortwave upward (VIS↑). The terrestrial infrared terms are emitted upward (L↑-dashed line), and emitted downward (L↓-solid line).

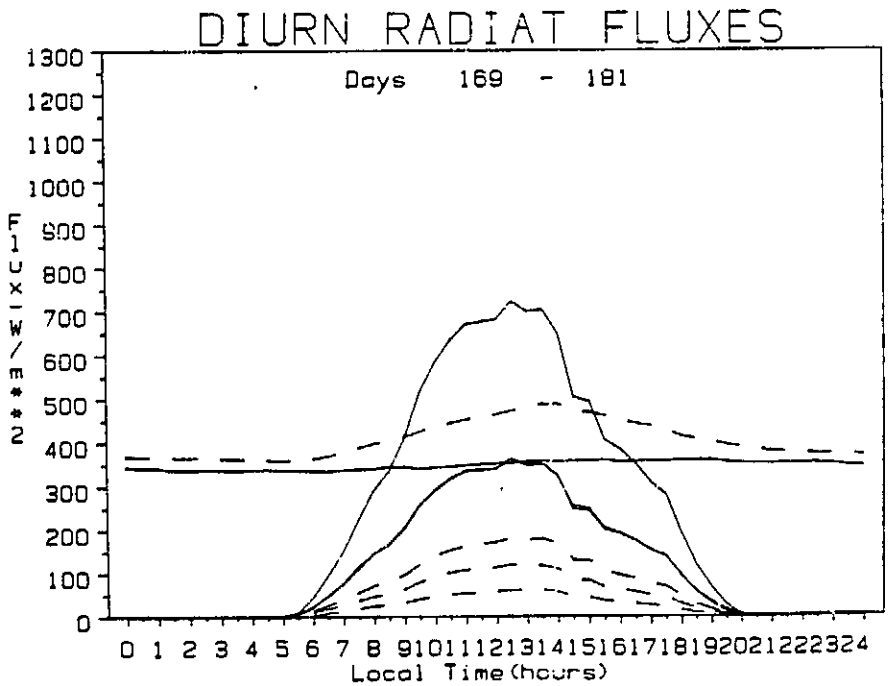

Figure 11b. As in Fig. 11a but for summer.

that the shortwave portion of the spectrum is defined by the near-infrared filter cutoff (0.7 μm), 48 percent of total available top-of-atmosphere insolation is present in the short wavelengths and 52 percent in the near-infrared wavelengths.) A secondary contrast between spring and summer periods, apparent in Fig. 11, is that the terrestrial infrared terms are less decoupled in the summer than in the spring. This difference is due to the presence of boundary layer moisture which tends to drive the surface land-air interface toward infrared equilibrium.

Figure 12 shows the total solar and terrestrial upward and downward flux terms along with the ±one standard deviation lines. Note that the summer period exhibits much higher variability due to the greater role of moisture processes and cloudiness.

The diurnally-averaged and daily averaged net radiation budgets are shown in Figs. 13 and 14. A close inspection of Fig. 13 reveals that the magnitudes (negative amplitudes) of the diurnal net radiation functions (Q*) are approximately equal. However, the integrated summer Q* curve contains substantially more energy than the springtime Q* curve (Fig. 14). This difference in total integrated radiative energy illustrates how differences in the surface radiation budget control surface heating. The larger summer period integral means that radiative exchange in summer is more effective in heating the surface. However, in the spring period the energy packet defined by the boundaries of both the Q* and L* curves is nearly equivalent to that of the summer period. Both the magnitude of the energy within this bounded region and its position relative to the zero line determine the role of the surface radiation budget. Since the total energy integrals within the bounded regions are equivalent, this suggests that seasonal differences in the

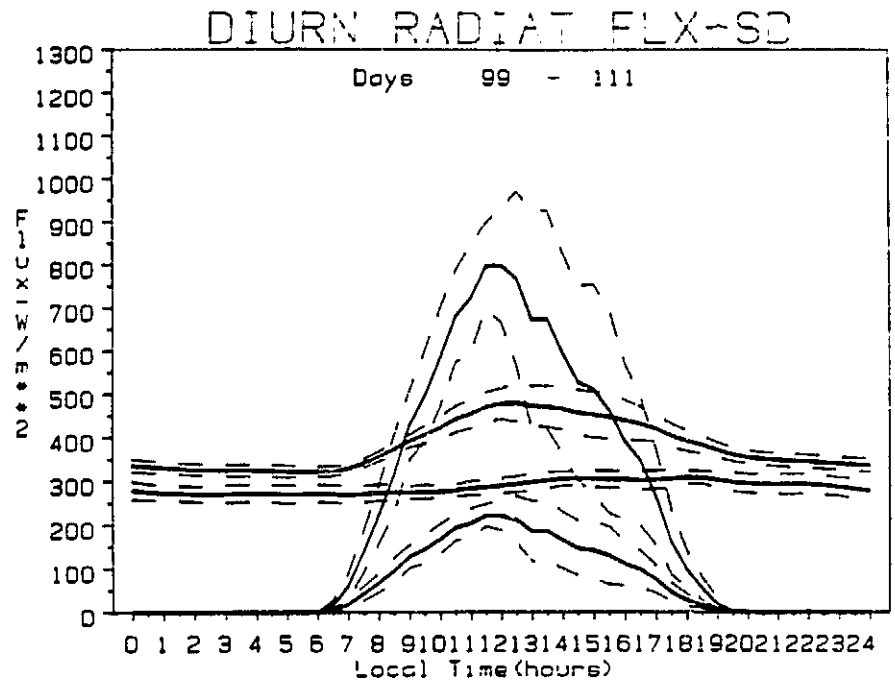

Figure 12a. Diurnally-averaged K↓, K↑, L↑, and L↓ terms along with the ±one "diurnal period" standard deviation lines for the spring period.

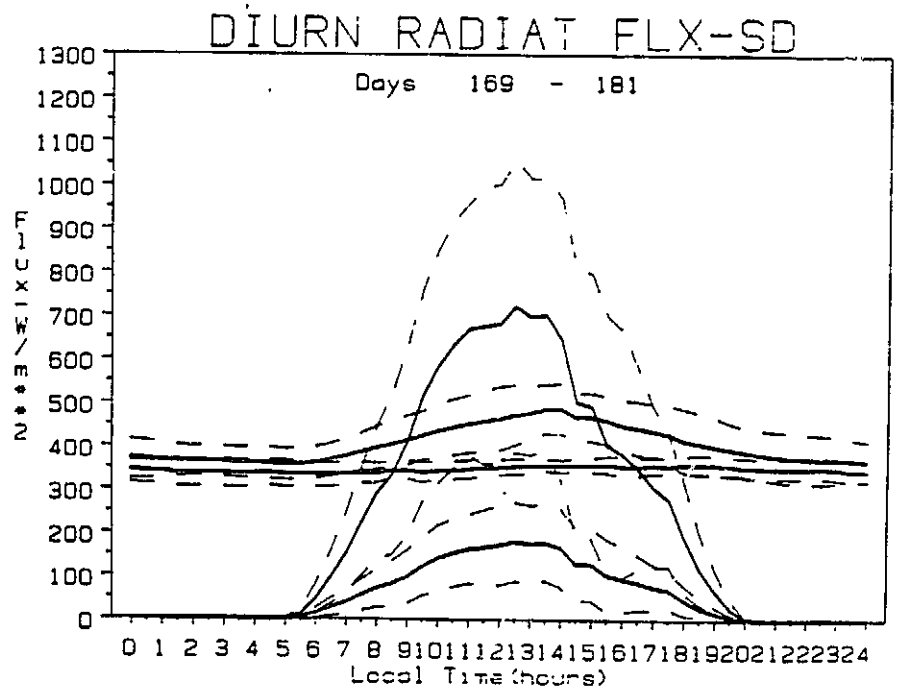

Figure 12b. As in Fig. 12a but for summer.

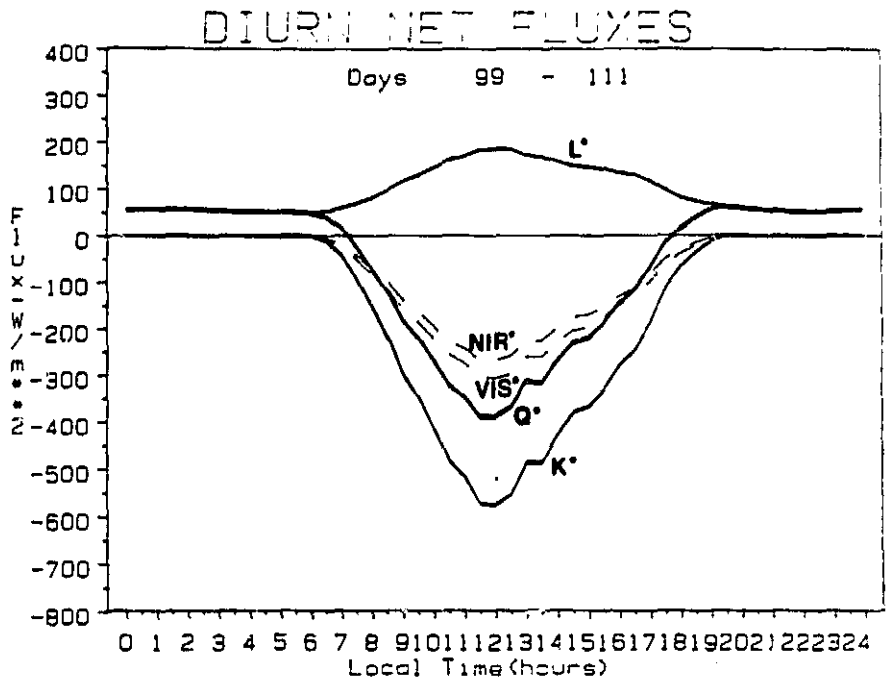

Figure 13a. Diurnally-averaged net radiation budget terms for spring. The curve above the zero line is L*; the curve furthest below zero line is K*; the thick solid curve falling between L* and K* is Q*. The two dashed curves portray NIR* (closest to zero line and hence, smaller) and VIS (farthest from zero line).

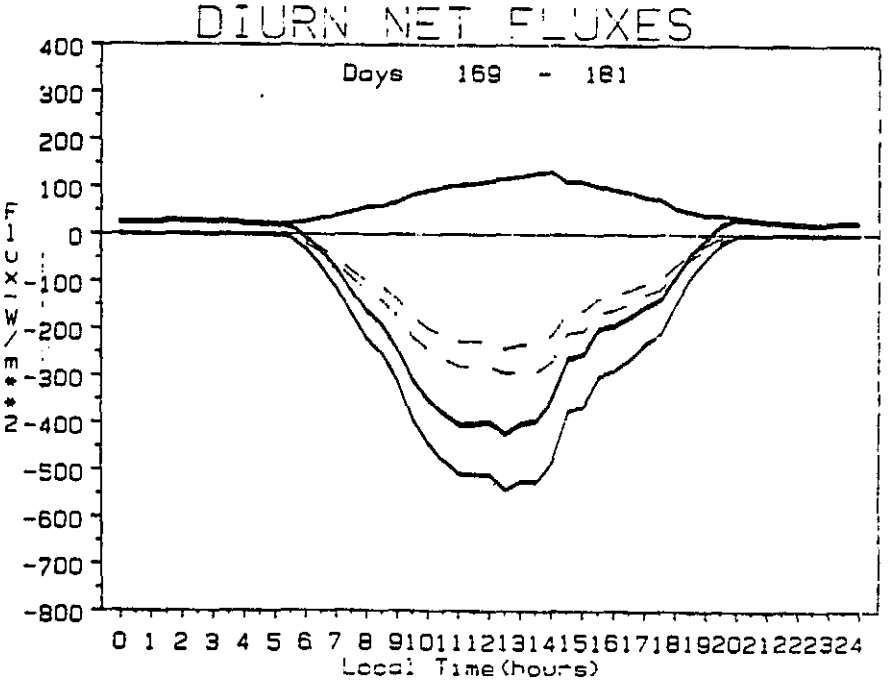

Figure 13b. As in Fig. 13a but for summer.

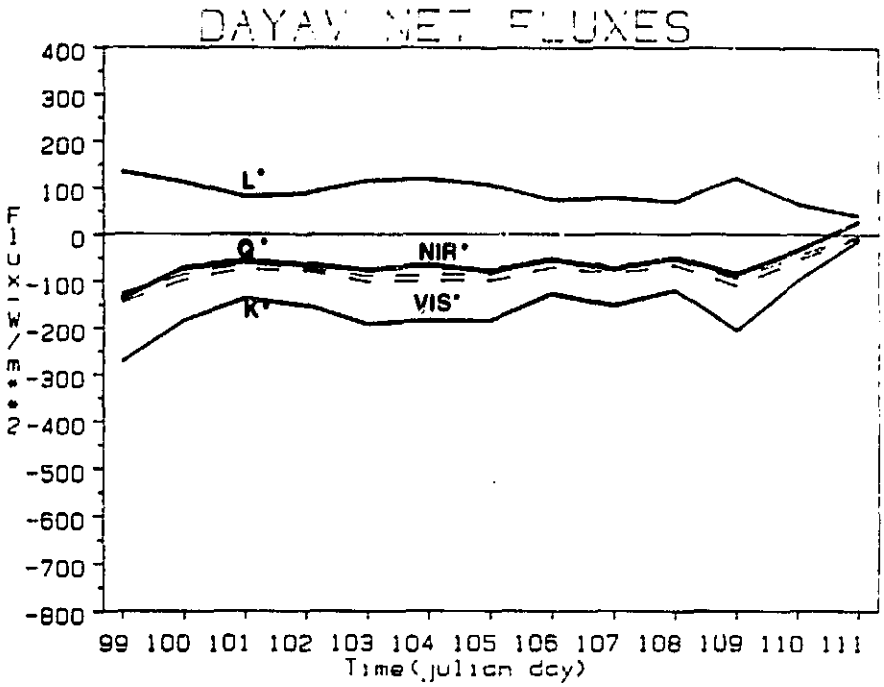

Figure 14a. Daily averaged net radiation budget terms for spring. The ordering of these terms is equivalent to that explained in Fig. 13.

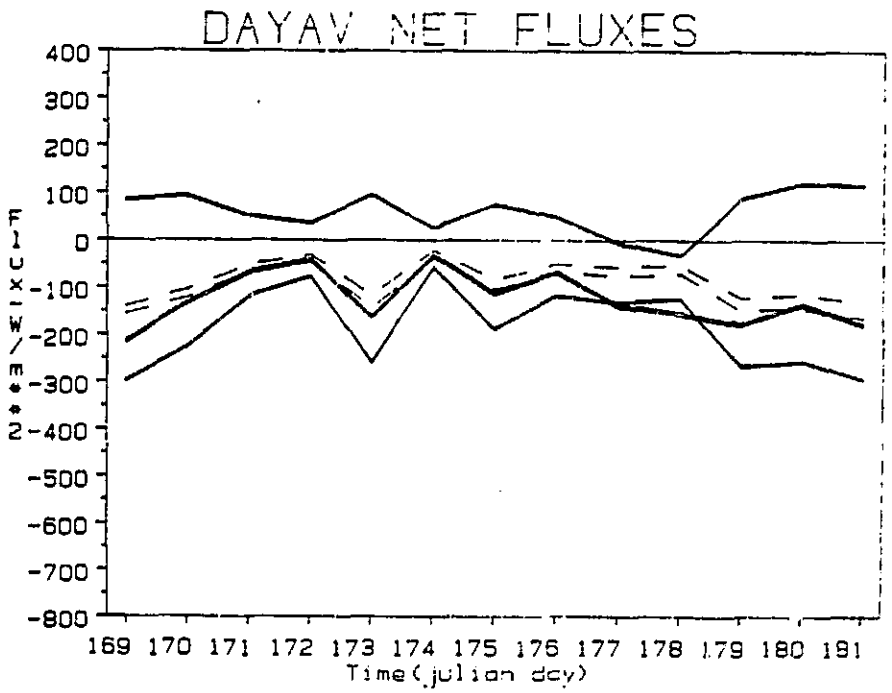

Figure 14b. As in Fig. 14a but for summer.

Gobi desert are not characterized by differences in total available surface radiation energy, but instead by how this radiation is distributed to either the atmosphere and surface.

The difference in the position of the spring and summer energy packets with respect to the zero line is accounted for by differences in the surface infrared radiation budget. This budget, in turn, is largely controlled by boundary layer moisture. Due to drier conditions, the amplitude of the L* term is larger in spring than in summer. This means that the total springtime surface radiation budget is larger than the summertime budget. Since L* represents the difference in L↑ and L↓ at the land-air interface, a difference which is highly sensitive to atmospheric moisture, it is concluded that the effectiveness in surface radiation exchange in heating either the atmosphere or surface is more dependent on atmospheric moisture availability, than it is on the absolute value of the individual exchange terms entering the surface budget. This phenomenon is easily observed at night when only infrared exchange is operative. The nature of the integral of the region bounded by the Q* and L* curves shall be closely observed in future investigations to determine if its effectiveness is a signature of the energetics at earth surfaces.

If the daily averaged net radiation budget terms are plotted for the two periods, as shown in Fig. 14, we note from a different perspective how summertime cloudiness tends to increase the variation of surface radiation exchange. Of greater interest, however, is the role of the net infrared term (L*). In springtime, the larger value of L* controls the daily averaged value of Q* such that Q* is approximately equivalent to either VIS* or NIR*. In summer, on the other hand, the

magnitude of the daily averaged Q* term is always greater than either the VIS* or NIR* terms which themselves have not changed a great deal in the mean from spring values. Phenomonologically these processes may not be of great interest. However, these inequalities are of value for parameterizing surface energy budget processes.

The time series of directional reflectance [$R(\theta_Q)$] and equivalent black-body temperatures (EBBT) associated with these flux quantities are shown in Fig. 15. It is easily observed in these plots that the radiative characteristics of the desert surface undergo seasonal changes, particularly in regards to albedo which decreases by approximately 5 percent between spring and summer. However, the net radiation budget is not particularly sensitive to these changes. The diurnal variations of the $R(\theta_Q)$ and EBBT functions are shown in Fig. 16. Two features in this figure are of significance. First, the near-infrared albedo is greater than twice that of the shortwave albedo; secondly, the classic concave appearance of the directional reflectance functions (i.e., diurnal albedo curves), is partially offset in the summertime by the diurnal cycle in the absolute moisture term. During the daytime, soil moisture is evaporated into the atmosphere, thereby increasing the near surface mixing ratio (see Fig. 6). At the same time, drying the surface leads to an increase in albedo. This explains the slightly convex appearance of the directional reflectance function at midday.

Finally, in Fig. 17, the diurnally averaged broad-band $R(\theta_Q)$ curve and the upward and downward EBBT curves are plotted along with ±one "diurnal period" standard deviation lines. Note again the larger variability in the summertime case. However, as the summer surface dries during midday, the variance over the diurnal period decreases,

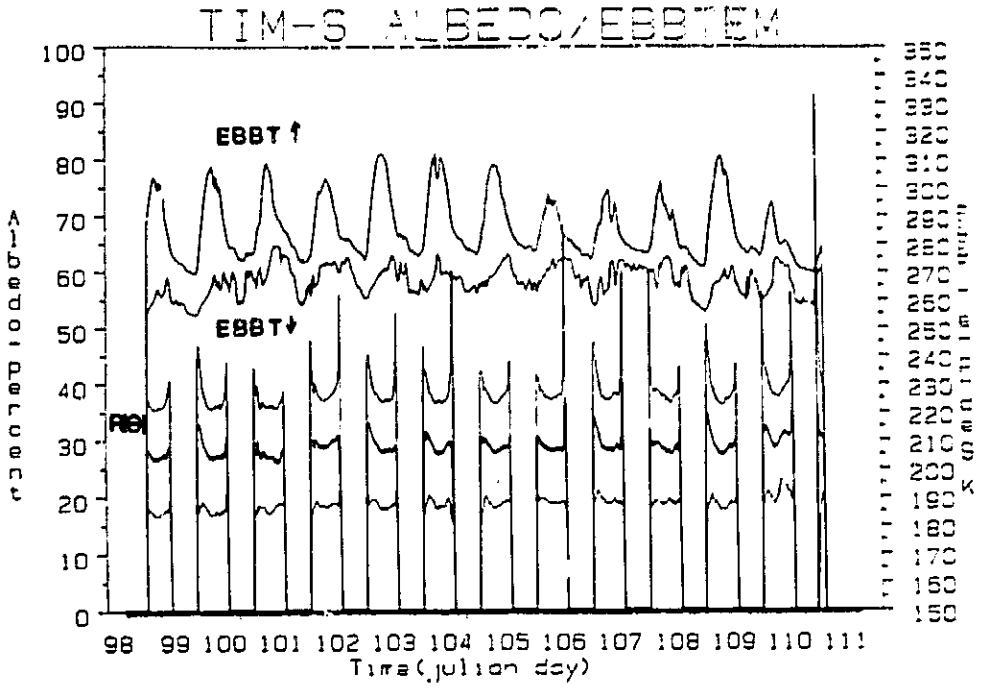

Figure 15a. Time series of directional reflectance and EBBT↑, EBBT↓ for spring. The three lower traces correspond to R(θ) for NIR, K, and VIS.

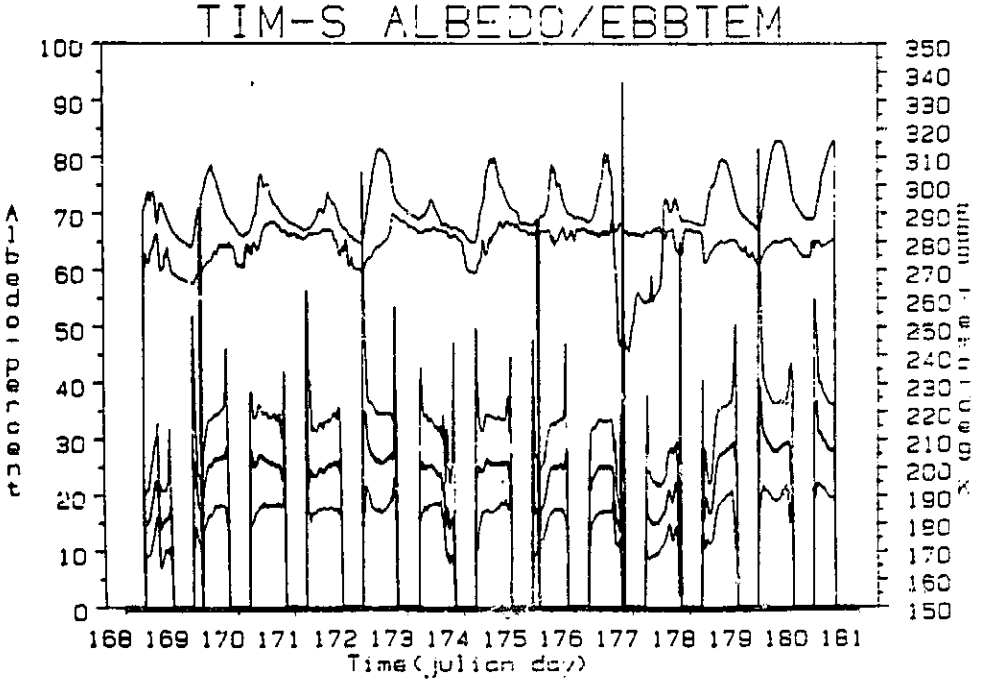

Figure 15b. As in Fig. 15a but for summer.

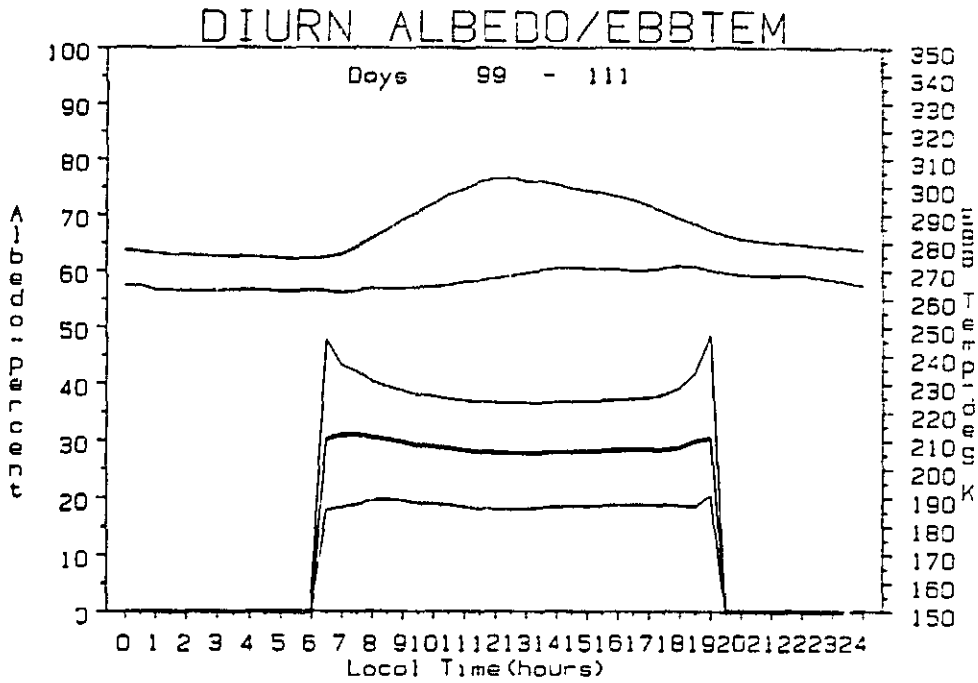

Figure 16a. Diurnally-averaged R(θ) and EBBT terms for spring.

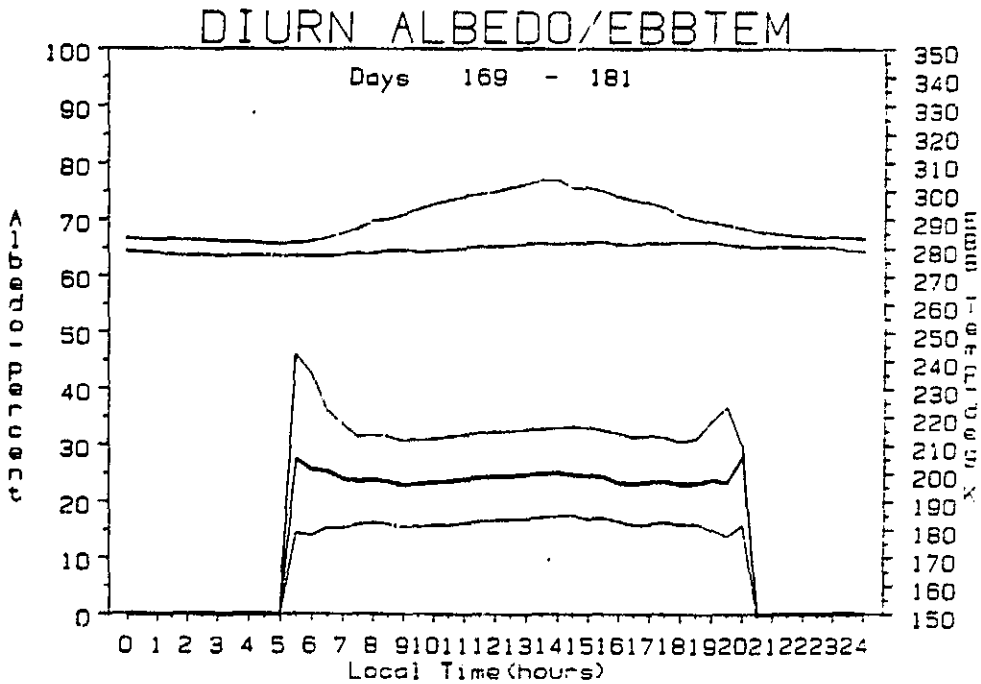

Figure 16b. As in Fig. 16a but for summer.

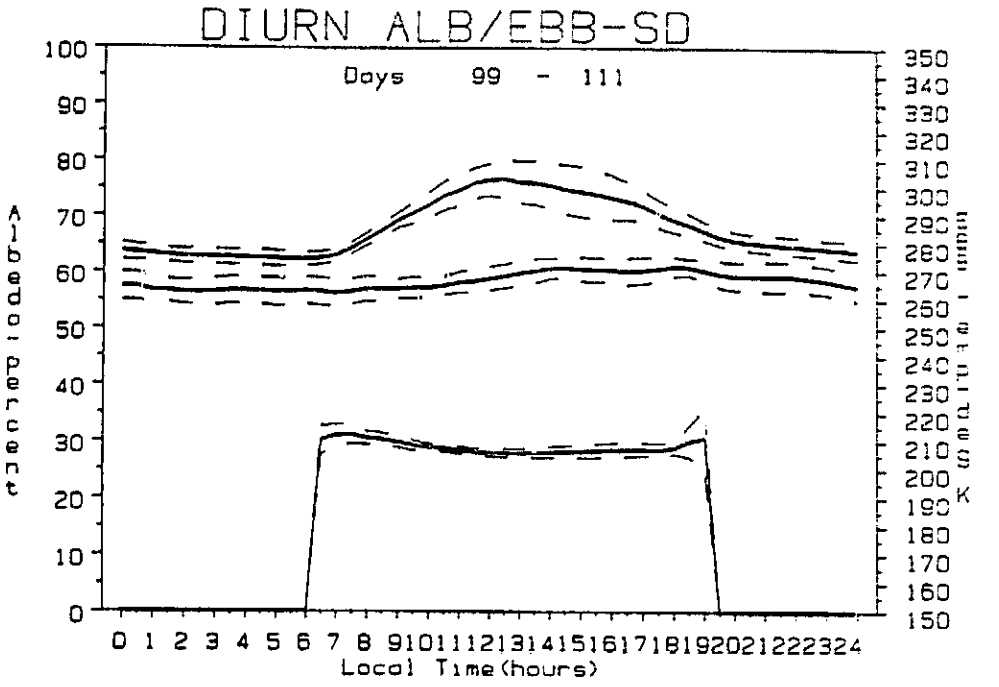

Figure 17a. Diurnally-averaged R(θ) for K and EBBT↑, EBGT↓ along with the "diurnal period" ±one standard deviation lines for spring.

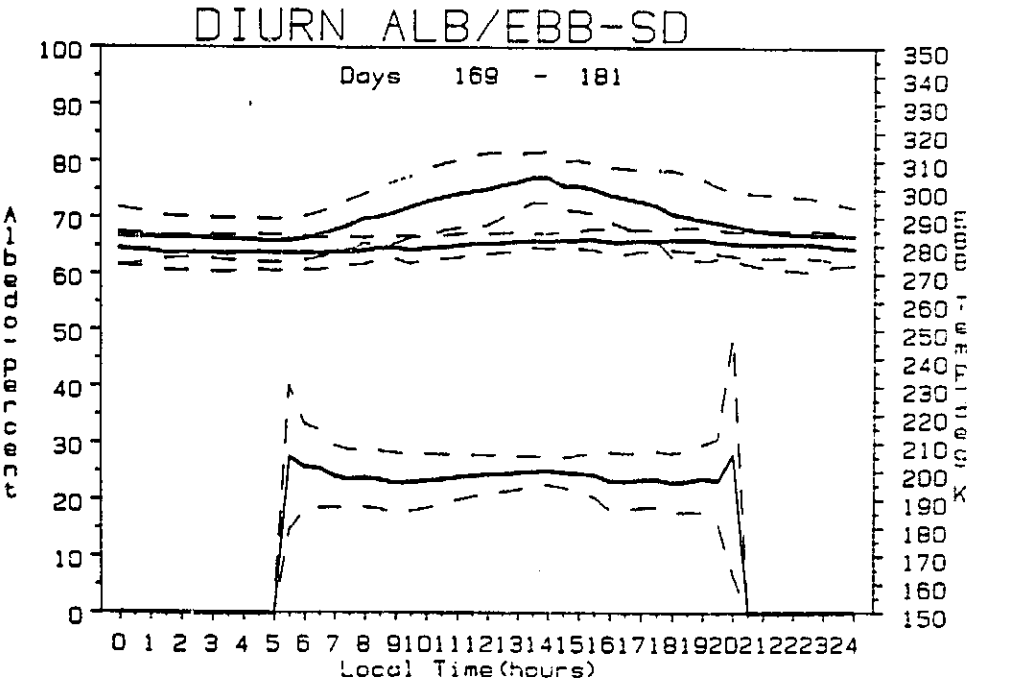

Figure 17b. As in Fig. 17a but for summer.

pointing out another important aspect of boundary layer moisture in controlling the desert's surface radiation budget. That is, as a land surface tends toward a desert, its albedo tends toward an invariant value and thus limits its ability to perturbe any imbalance in the energy exchange process.

e. Subsurface Thermal Storage

The calculation of soil heat storage is based on applying a finite-distance summation operator to the soil thermistor data taken at 4 levels (2, 8, 20, and 40 cm). The following table indicates the depths and layer thicknesses used in computing subsurface thermal storage.

Layer	Thermistor Depth (cm)	Layer Depth (cm)	Layer Thickness (cm)
1	2	0-4	4
2	8	4-12	8
3	20	12-28	16
4	40	28-52	24

The heat capacity of the dry sand-soil mixture was established at $0.8 \cdot 10^{-3}$ $J \cdot Kg^{-1} \cdot deg^{-1}$, with a density of $1.45 \cdot 10^{3}$ $kg \cdot m^{3}$. Time series of the subsurface thermal waves at the four depths are shown in Fig. 18 for the spring and summer periods. Note that for the upper two probes the day-night extremes (temperature amplitudes) are higher in the spring than in the summer, denoting how a drier atmosphere allows more effective infrared cooling of the upper soil surface layer. The impact on the lower layers, on the other hand, is insignificant. The diurnally-averaged plots are shown in Fig. 19. These plots illustrate the mean amplitudes of the thermal waves as a function of depth; also note how the thermal waves are phase-shifted as a function of depth.

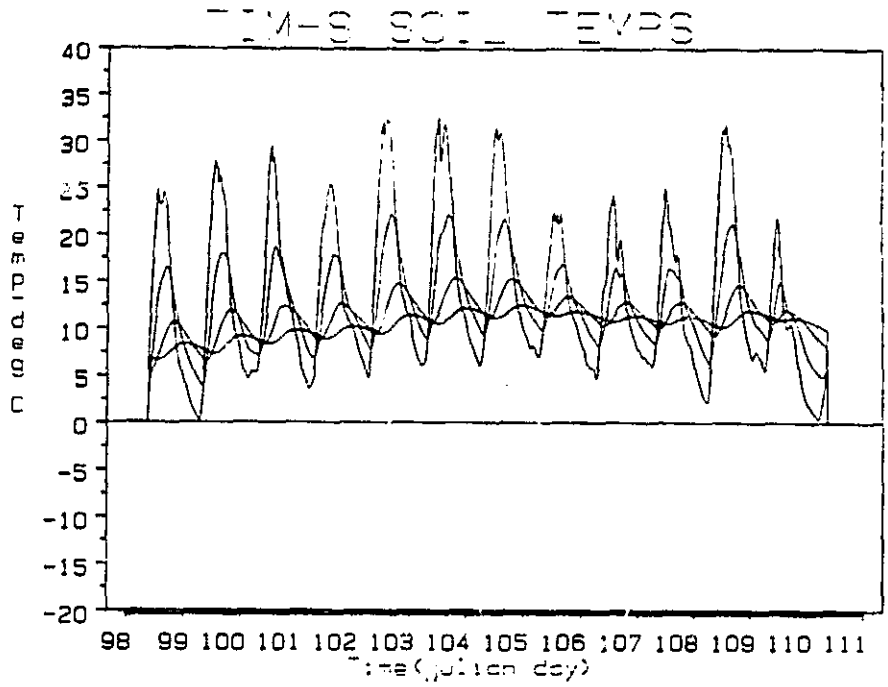

Figure 18a. Time series of soil temperatures at four depth (2, 8, 20, 40 cm) during spring.

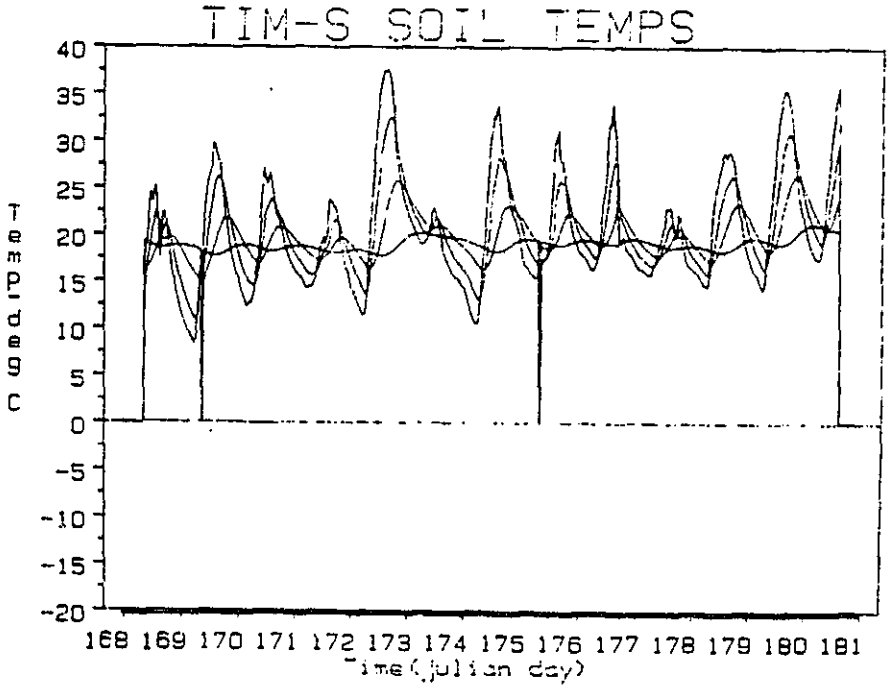

Figure 18b. As in Fig. 18a but for summer.

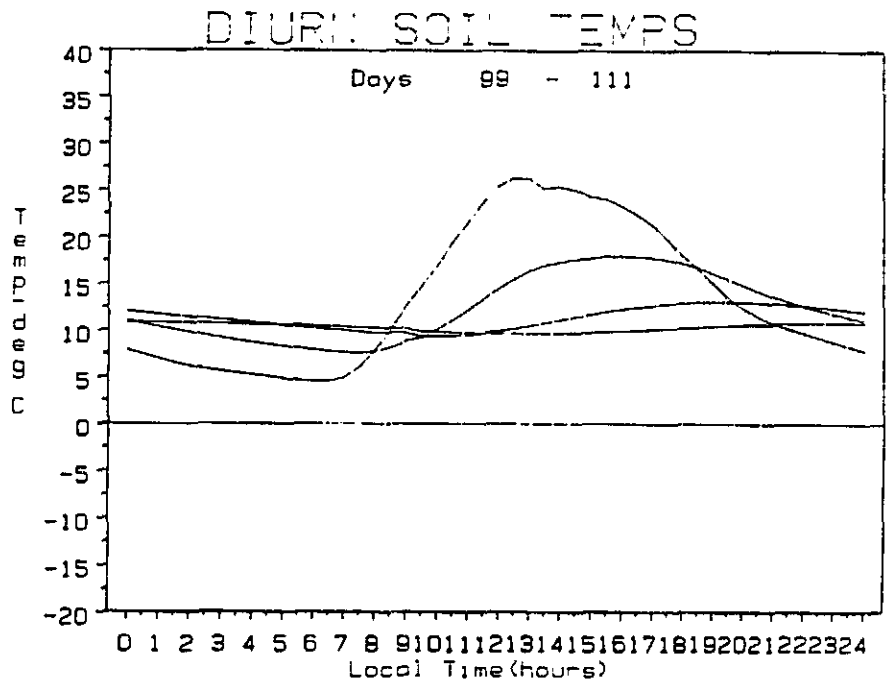

Figure 19a. Diurnally-averaged soil temperature as a function of depth (2, 8, 20, 40 cm) during spring.

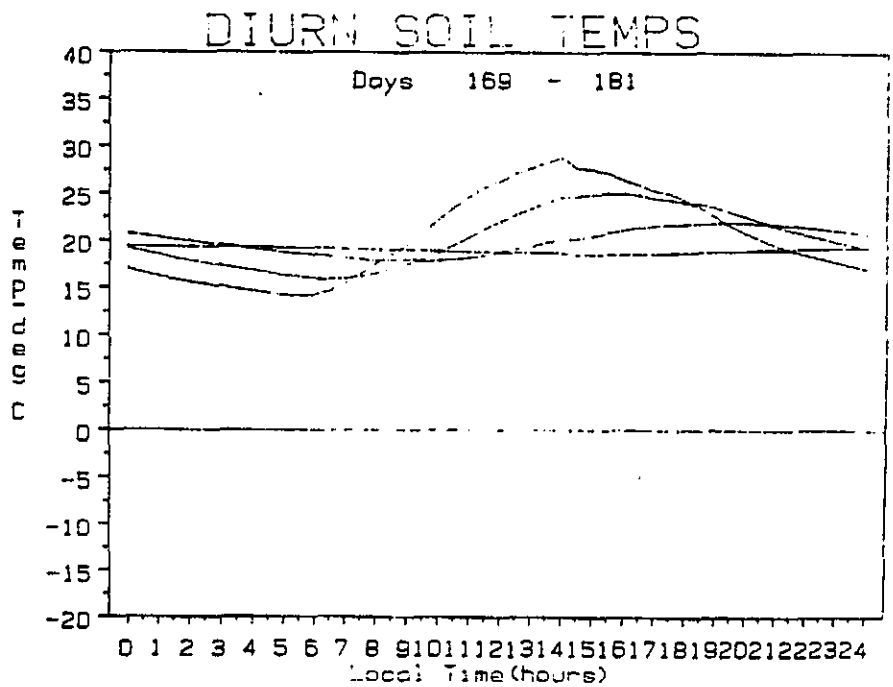

Figure 19b. As in Fig. 19a but for summer.

f. Subsurface Moisture Storage

We have made preliminary examinations of the soil-moisture but have not yet converted the engineering scale (resistance potential) of the sensors to field capacity or partial pressure for various soil types. Precise calibration is needed in order to estimate exchange of water mass between the land-air interface. Nevertheless the results (given in bars) for the spring and summer, illustrate some of the key features of moisture exchange in the western Gobi. In Fig. 20a the two upper probes are seen to dry out soon after placement in the ground after they are presoaked to saturation. (The values go off scale and are interpreted by the data processing scheme as missing data.) The third probe (20 cm) slowly drys out from its initial presoaked condition but does not go off scale. The modest fluctuations of the third level are apparently caused by thermally-forced distillation processes which are described in detail in Section 3.2. The deep probe (40 cm) did not undergo any changes throughout the course of the spring measurement period.

During the summer period (Fig. 20b), there were three recorded precipitation events (spikes on the abscissa). Note how the top probe goes off scale (dries) on day 172, but then returns on-scale on day 178 after the largest precipitation event on day 177. The diurnal fluctuation of soil moisture is clearly evident at all levels during summer. Recently we discovered an intermittent failure mode in the rain gauge that probably led to missing rainfall events (see Table 1, Section 3.2). This problem was corrected in the U.S. observation programs and a more substantive discussion of soil moisture observations is given in Section 3.2.

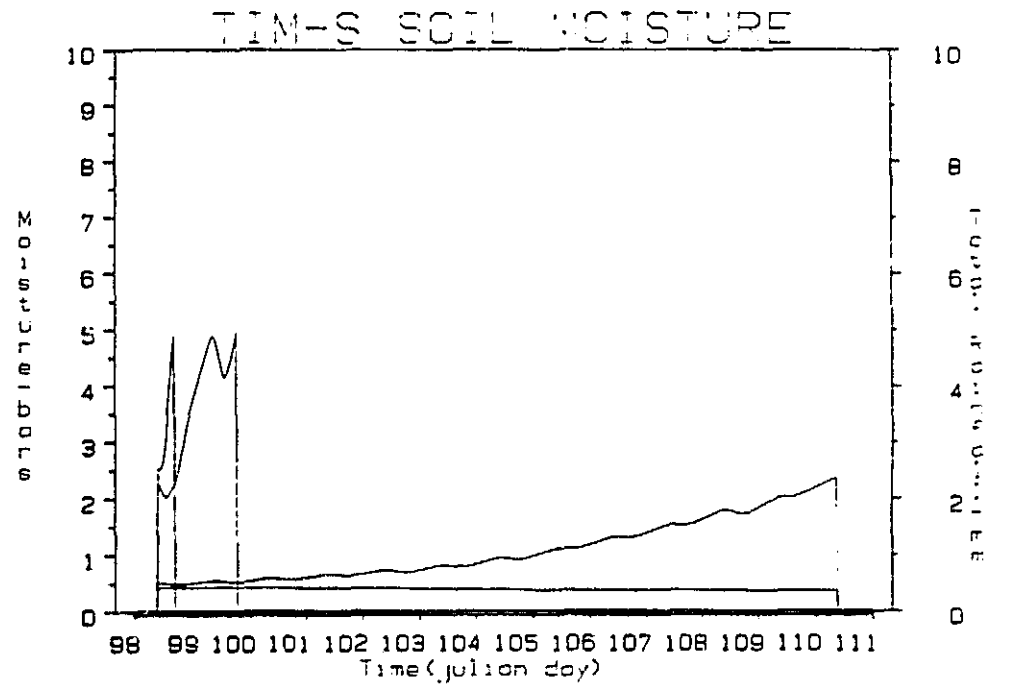

Figure 20a. Time series of soil moisture at four depths (2, 8, 20, 40 cm) during spring. Note the top two probes (2 and 8 cm) go off scale on days 98 and 100, respectively.

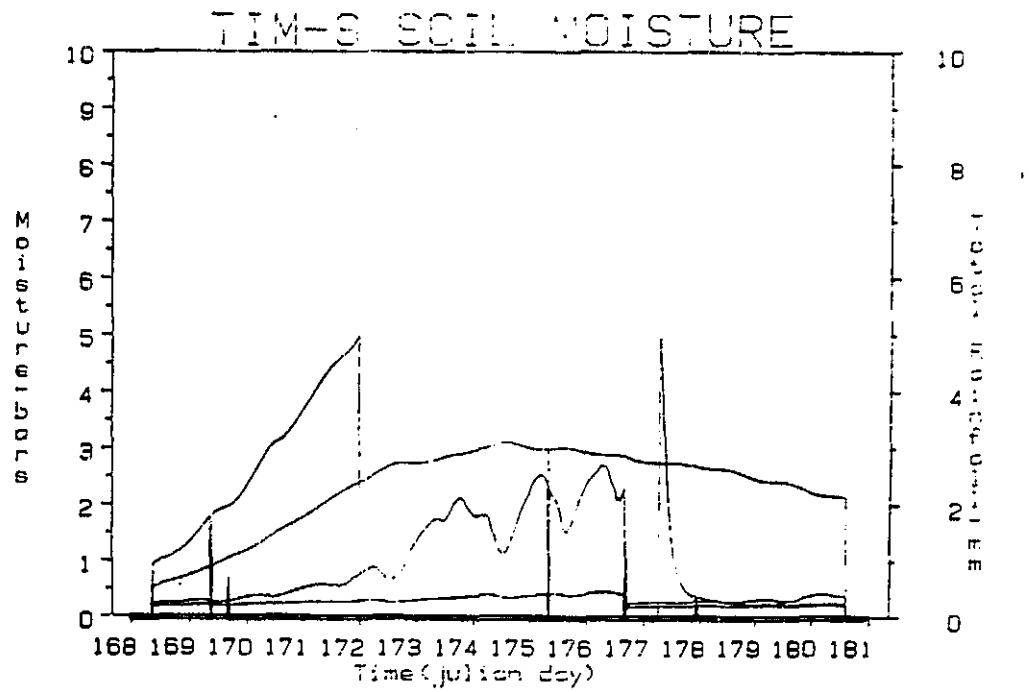

Figure 20b. As in Fig. 20a during summer. The top (2 cm) probe goes off scale on day 172--returns to scale on day 178.

g. Complete Surface Energy Budget Derived from the Radiation Station

Initially we have used the Radiation Station data in a stand-alone mode to calculate all of the energy fluxes and thus complete a depiction of the complete surface energy budget. The turbulent fluxes (sensible and latent heat) are arrived at by first estimating a total or bulk turbulent flux (sensible plus latent) based on the residual difference between net radiation (Q^*) and thermal storage in the soil (S). The sensible heat term is then calculated independently from the bulk aerodynamic formula. Here we utilize the EBBT↑ term as an estimate of surface skin temperature in conjunction with a constant drag coefficient of $1.0 \cdot 10^{-3}$ (representative of the desert). The difference between the total turbulent flux and the sensible heat flux is then an estimate of latent heat flux. Diurnal averages for these terms are presented in Fig. 21 for the spring and summer periods. The results are then combined with the Q^* and S terms to illustrate the complete surface energy budget for the western Gobi (Fig. 22).

The immediate conclusion that can be drawn from these diagrams is that the surface radiation budget leads to a larger overall heating of the atmosphere during summer. However, much of this increase is apparently due to latent heat effects since the spring and summer cycles of sensible heating are nearly equivalent. The amplitudes of total turbulent heating computed in this way are approximately 300 and 350 $w \cdot m^{-2}$ for spring and summer, respectively.

We recognize that there are remaining problems with the sensible heat calculations since, for example, nighttime values of sensible heat flux are much too large. This discrepancy forces the improbable positive nighttime latent heat fluxes shown in Figs. 21 and 22. The

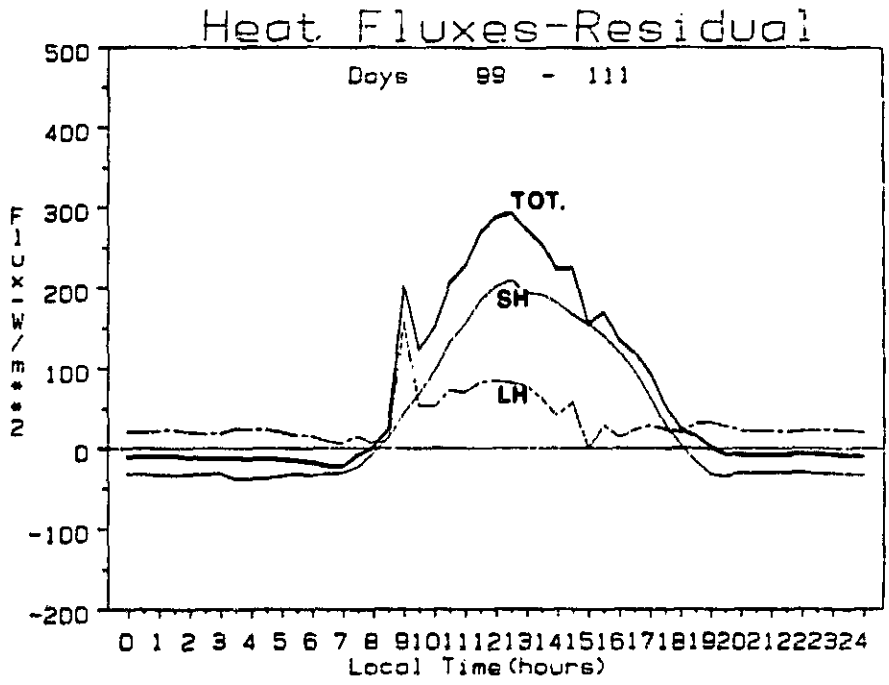

Figure 21a. Dirunally-averaged heat fluxes during spring. The thick solid line is total; thin solid is sensible (SH), dashed is latent (LH).

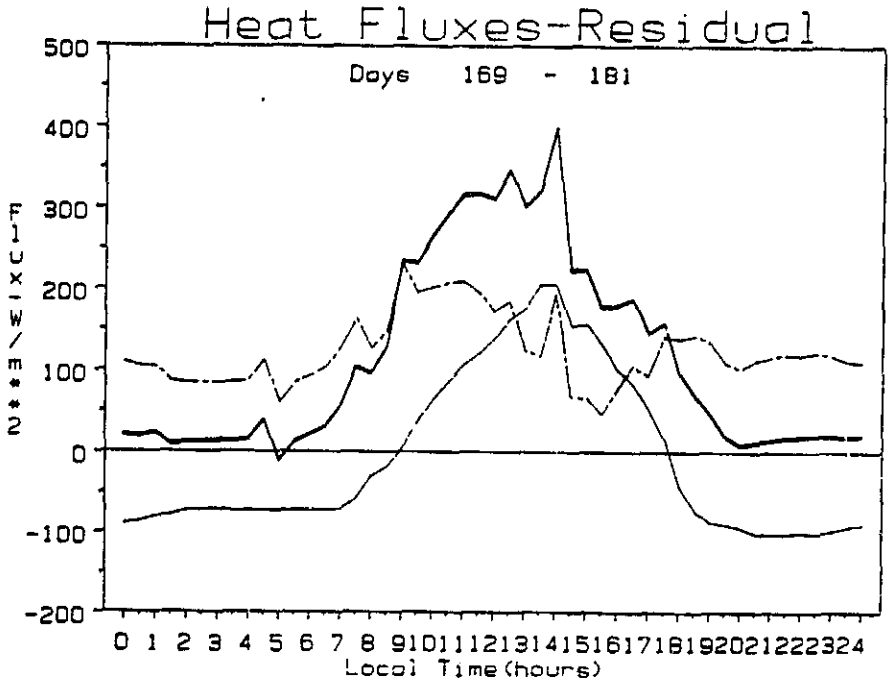

Figure 21b. As in Fig. 21a but for summer.

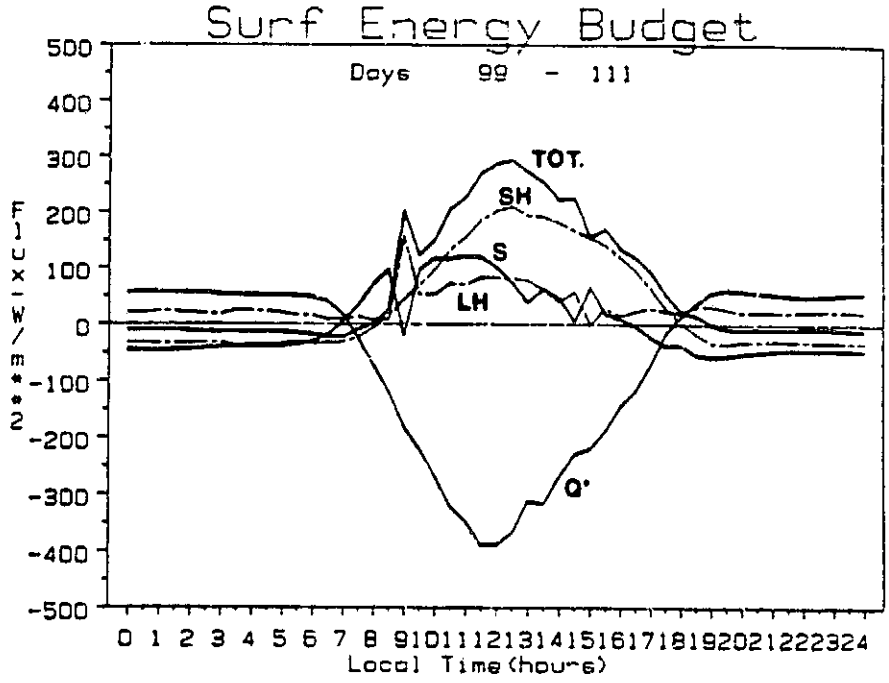

Figure 22a. Diurnally-averaged surface energy budget during spring. The three solid curves are TH, S, and Q*. The two dashed curves represent SH and LH.

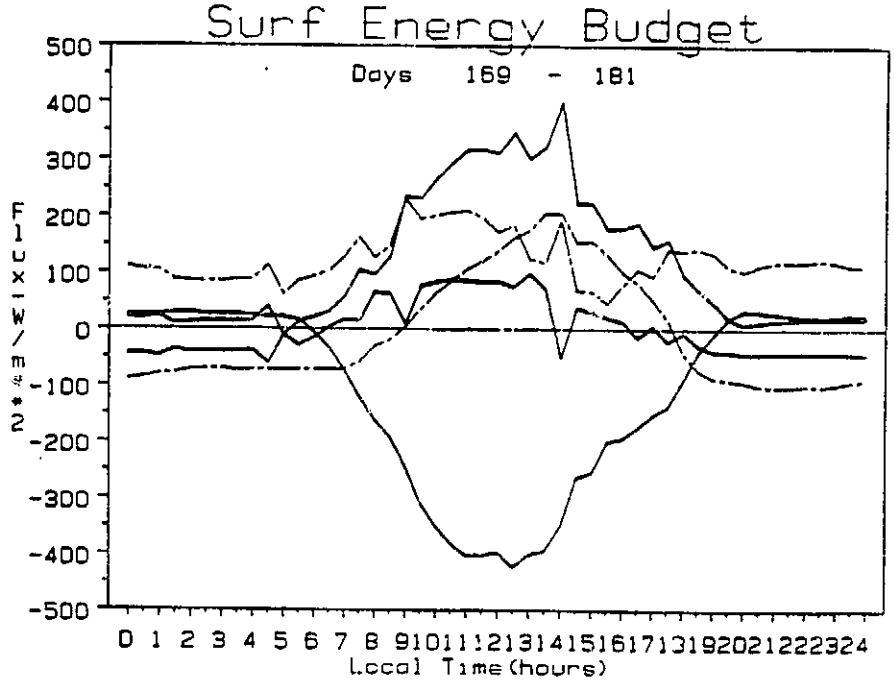

Figure 22b. As in Fig. 22a but for summer. In this try SH and LH are labeled.

principal reason for these errors is the use of a constant drag coefficient which, in this case, leads to overestimates of downward sensible heat fluxes under stable nighttime conditions. Moreover, under unstable conditions an optimum drag coefficient (derived for neutral conditions) will typically lead to systematic overestimates of turbulent fluxes for strong winds and to underestimates for light winds. Scaling the drag coefficient by a simple bulk Richardson number should greatly improve these results. In addition, we have not attempted to use soil moisture data to vary our estimates of the soil heat capacity, an adjustment that will also improve the overall accuracy of the flux estimates.

h. Measurement and Calculation of Heat Fluxes from the Tower Station

We have examined the sensible and latent heat exchange terms measured directly by the tower station at 3 levels. Furthermore we have experimented with the application of similarity theory in five different modes [corresponding to different methods of estimating the scaling temperature (T^*) and friction velocity (V^*)], based on the profiles of the mean values. These results have not yet been synthesized so that they could be interpreted. However, Figures 22-28 are used to present examples of various of the reduced profile data. These types of plots are used to diagnose data quality and to identify interesting and/or spurious perturbations.

Our initial analyses have identified several problems which serve to degrade the quality of the tower derived sensible and latent heat exchange terms. These problems, described in the Section 4.0 of this report, are being corrected for the Tibetan field phase.

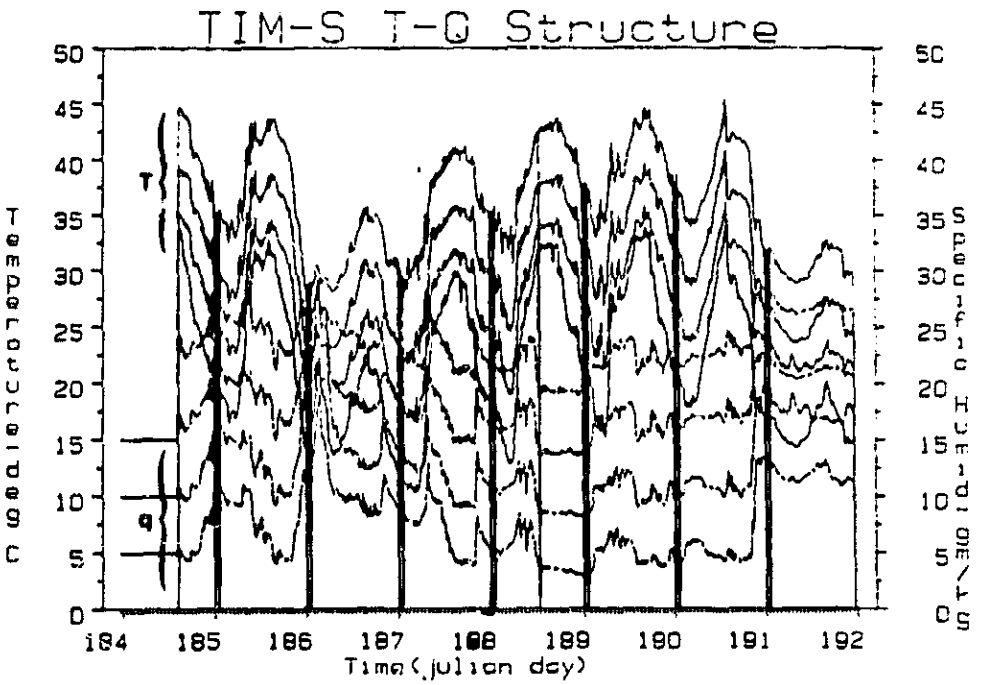

Figure 23. Time series of temperature profile [T(z)] and specific humidity profile [q(z)] at four tower levels (0.2, 2, 4, 8 m) during summer. The 2, 4, 8 m traces are increased by 5, 10, and 15 des or gm·kg^{-1} in order to provide separation.

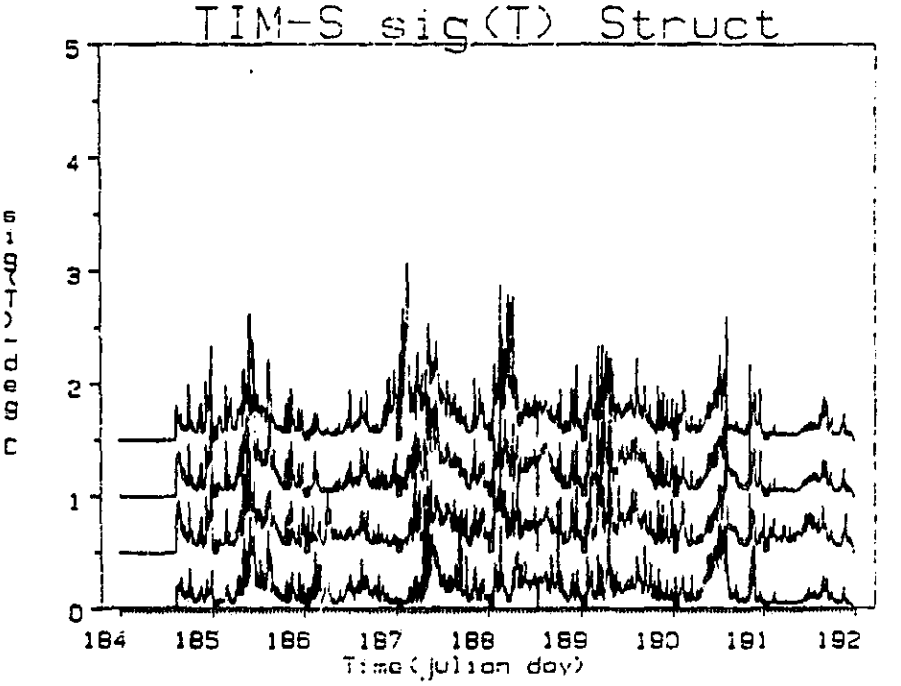

Figure 24. Time series of standard deviations of T(z) over the integration period ("local sigma") at the four tower levels during summer. The sampling rate is one hz; the integration period is ten minutes.

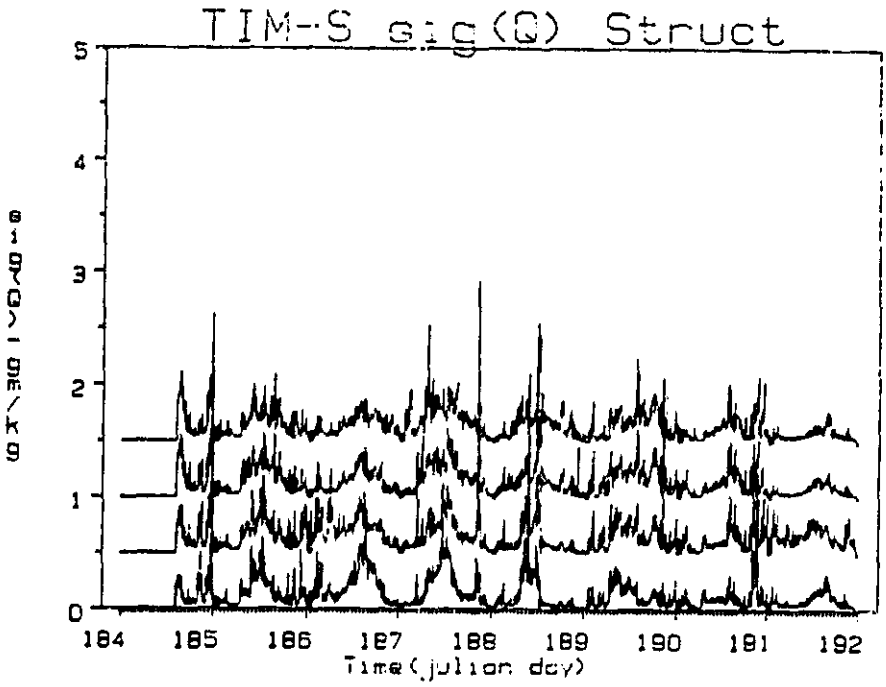

Figure 25. As in Fig. 24 but for q(z).

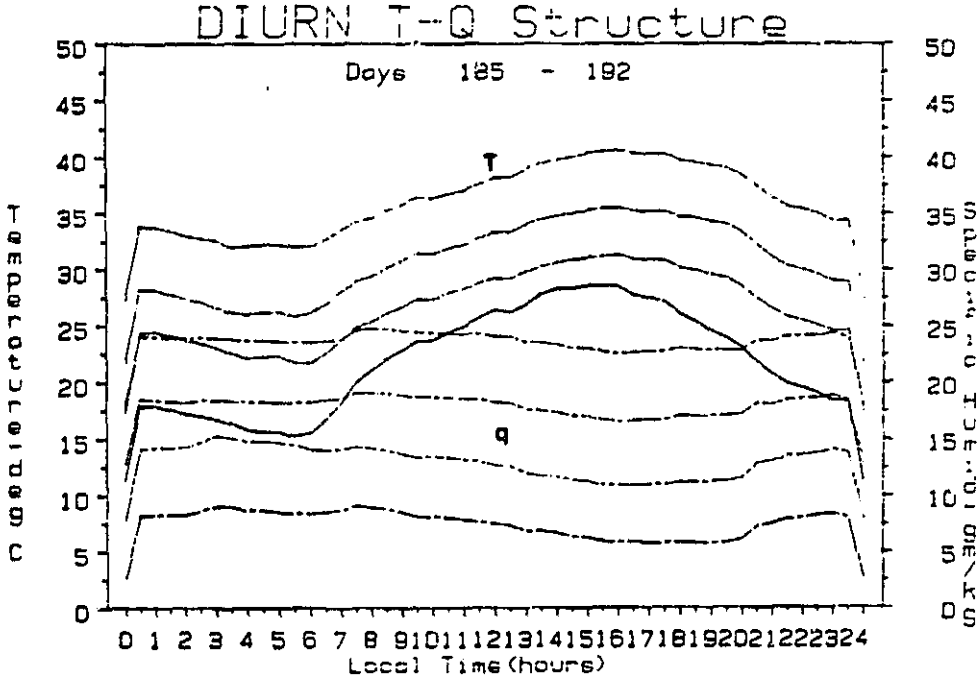

Figure 26. Diurnally-averaged T(z) and q(z) profiles during summer. The plotting procedure is equivalent to that used in Fig. 23 (the q(z) plots are dashed).

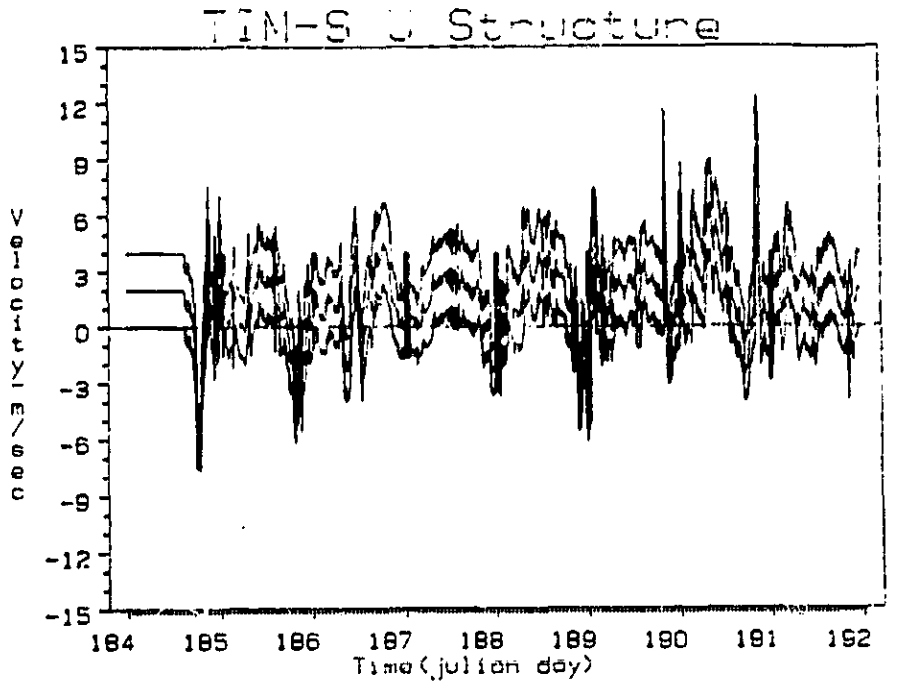

Figure 27. Time series of u-component of wind at three levels (2, 4, 8 m) during summer. The upper two traces are separated by 2 and 4 $m \cdot sec^{-1}$.

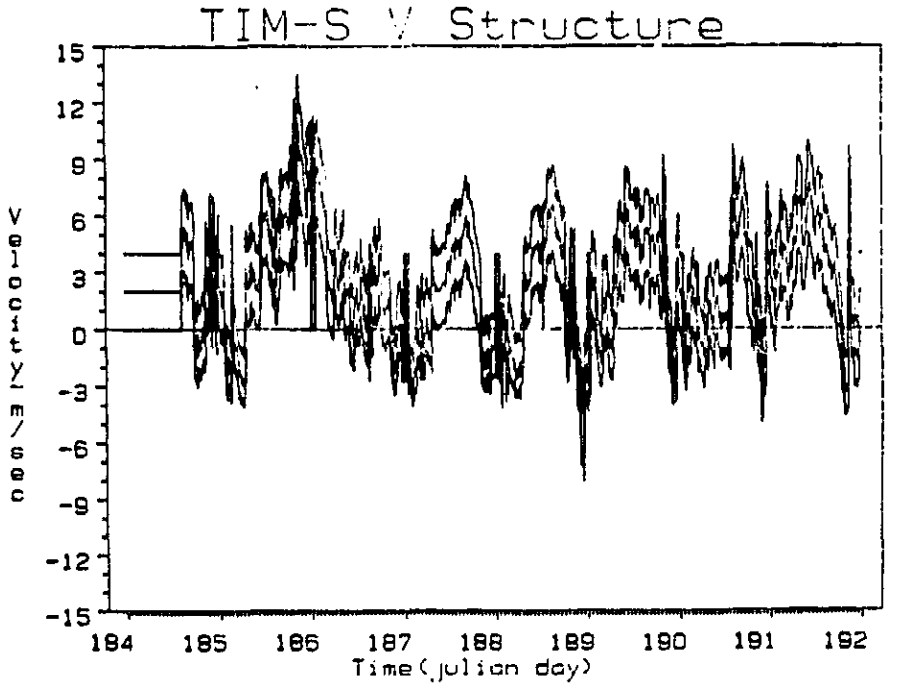

Figure 28. As in Fig. 27 but for v-component of wind.

3.0 ROCKY MOUNTAIN MONITORING EXPERIMENTS: INTRODUCTION

Two monitoring experiments were conducted in the Rocky Mountains near Fort Collins, Colorado. The first took place between March 13 and July 17 (JD 73-199) in a mountain valley called Pingree Park, 60 km west of Fort Collins. The second experiment was conducted between July 31 and Sept. 3 (JD 213-247) at a mountain top site called Storm Peak, near Steamboat Springs, Colorado, 240 km west of Fort Collins. Details of the physical settings for each experiment are given in the next section (3.1). Representative data collected at each site are described in Section 3.2 along with preliminary comparative analyses of the surface energy budget in each area. Section 4.0 gives a brief critical review of the performance of the monitoring system and describes some improvements that are presently being made.

3.1 Experimental Settings

a. Pingree Park

This site was in a mountain valley at an elevation of 2750 m. Views of the site are shown in Fig. 29. The valley was oriented southwest to northeast, opening to the northeast, and had elevations generally exceeding 4000 meters to the west. Monitoring occurred near the southeast edge of the valley. The instruments were situated on the crest of a broad moraine which rose approximately 10 meters above the valley floor. The site was in a 5-year old clear-cut, approximately 200 meters long and 100 meters wide. The soil in the area was rather coarse and sandy with a large portion of loose rock and several cm of plant litter covering most of the surface. Vegetation around the monitors (Fig. 30a) was rather minimal; consisting of sparse grass with a few small evergreen and aspen trees. The soil cover directly beneath

Figure 29a. Pingree Park monitoring site, looking toward south-southeast. The radiation station is just to the right of the tower near the center of the photo.

ORIGINAL PAGE
COLOR PHOTOGRAPH

Figure 29b. View of Pingree Park wind tower looking south-west.

Figure 30a. Ground cover beneath the downward looking radiometers at Pingree Park.

Figure 30b. Ground cover over the Pingree Park soil probes. The pit in which the probes were inserted is approximately 30 cm to the left of the point where the sensor leads emerge from the surface litter in the center foreground.

the downward looking radiometers and over the soil probes are shown in Fig. 30b. Weather during the 126 day experiment was characterized by a wet (snowy) spring followed by an abnormally rapid melt off and a comparatively dry summer.

b. Storm Peak

This site was on an exposed ridge top at an elevation of 3200 meters. The east-west oriented ridge was generally void of trees (Fig. 31). The soil at the site was similar to that of Pingree Park but the surface cover was limited to a thin mixture of low tundra flowers and grass. The previously forested area had burned approximately 20 years before and little regrowth had occurred. Strong winds had effectively removed virtually all dead plant litter and hence the soil surface had both more green vegetation and more bare soil than the Pingree Park site (Fig. 32). Weather during the 34-day study was generally wet, especially during the last 20 days. However, several three to five day dry spells allowed intermittent drying of the surface. Data capture was effectively 100 percent for both monitors except for when wind-driven fog occasionally saturated the hygristor elements on the tower system.

3.2 Results

A rather large quantity of data was collected. This section begins with a brief description of the data set and efforts to fulfill our data sharing obligations with our Chinese counterparts. This discussion is followed by a summary of the basic meteorology at each site and a comparative analysis of the observed components of the energy balance. The last portion of this section contains an analysis of the latent and sensible heat fluxes for each site. As with the Gobi results, these

Figure 31a. View of the Storm Peak site looking east-southeast. The monitoring stations were placed on the crest of the grassy ridge in the background to the right.

Figure 31b. View of the Storm Peak wind tower looking west-southwest.

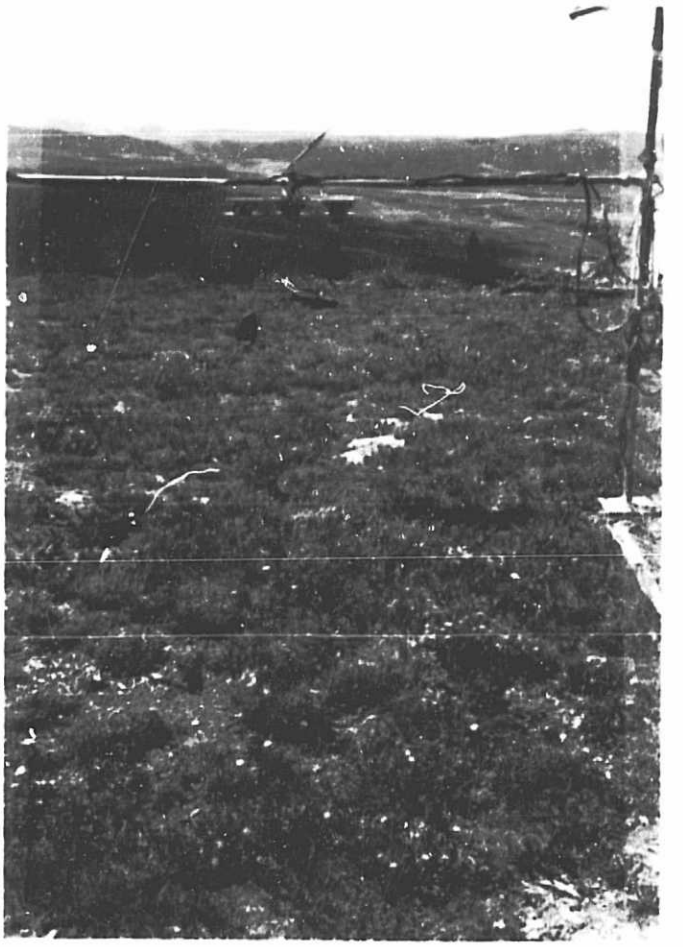

Figure 32. View of the downward radiometer at the Storm Peak site looking west.

analyses are preliminary and may change somewhat as we become more familiar with the data.

a. Data

In general data capture was very good but some data loss did occur. These occurrences are summarized in Table 1. The radiation and wind tower data loggers recorded 88 and 98 observed or derived parameters respectively for each averaging period. These parameters and the basic data format are listed in Tables 2 and 3. Each sensor was scanned every two seconds and averages or related statistics were computed and recorded ever 15 minutes by the radiation station and every 5 minutes by the wind tower station.

Because the Chinese were unable to directly read the data cassettes into their computer, all Chinese data were first sent to Colorado State University for reformatting into a suitable data structure. All U.S. and Chinese cassettes were read into our computer, tested for errors and missing data and then processed into a complete preliminary data set. The data were then rewritten onto standard nine-track tapes. After several unsuccessful attempts a rather cumbersome data structure compatible with the Lanzhou computer was devised. The final data set (requiring ten 2400 foot reels of nine-track tape) was then sent to Lanzhou during December 1984 and January 1985.

b. Meteorology of the Pingree Park and Storm Peak Sites

The valley setting of the Pingree Park site lead us to anticipate a recurrent diurnal wind circulation dominated by daytime up-valley and nighttime down valley flow, especially during the sumer season. This flow was not observed. Typical winds for the winter (JD 73-80) and summer seasons (JD 172-189) are shown in Fig. 33 (the tic marks on the

Table 1. Various problems with the data collection systems caused the loss of data from time to time. These are summarized as follows, first for the radiation station and then for the wind tower.

Radiation Data Problems:

1. When temperatures fell below about -12°C, the cassette recorder tended to fail. These occurrences are limted to a few 5-10 hr periods prior to Julian Day (JD) 122.

2. Prior to JD 130 the rainfall gauge was filled with snow and did not function.

3. Prior to JD 159 the programming in the data logger had an error such that most of the rainfall data were not recorded properly. Only precipitation measurement signals occurring during the last 15 seconds of any one minute period were recorded. Fortunately little rainfall occurred in the Pingree Park area prior to JD 167. Unfortunately this same error was in the programming for the Gobi radiation data logger and could not be corrected.

Wind Tower Data Problems:

1. When temperatures fell below about -8°C the cassette recorder for the tower tended to fail. These periods of missing data tend to occur at the same time as those at the radiation station and are limited to brief periods prior to JD 122.

2. Between JD 73 and JD 80 several strong wind storms damaged the wind sensors. Only the W component sensors at the middle and top levels were undamaged. These problems were caused by strong resonant vibrations in the tower when winds exceeded 25 m/s. We noted that these vibrations did not occur when the U and V component arms were removed. Hence, because these wind storms occur frequently during the winter and spring, data were collected for the W component only between JD 80 and JD 167. The U and V components were restored on the middle level on JD 167 and on the top and bottom levels on JD 172. Also, serious damage to the top sensor required us to remove and repair it between JD 80 and 89. Lastly, between JD 139 and 145 the top level W sensor was damaged, apparently by a large bird attempting to sit upon it.

3. The temperature and humidity sensors on the lowest level were occasionally covered with snow, mostly between JD 89 and 122.

RADIATION STATION
CR-7S OUTPUT TABLE 2

01 101	02 JD	03 HHMM	04 TST	05 ND/MV	06 KD/MV	07 NU/MV	08 KU/MV
09 LD/MV	10 LU/MV	11 TsD/V	12 TsU/V	13 TdD/V	14 TdU/V	15 TsD/K	16 TsU/K
17 TdD/K	18 TdU/K	19 ND/W	20 KD/W	21 NU/W	22 KU/W	23 LD/W	24 LU/W
25 SD-ND/W	26 SD-NU/W	27 SD-KD/W	28 SD-KU/W	29 SD-LD/W	30 SD-LU/W	31 VD/W	32 VU/W
33 V*/W	34 AV/F	35 L*/W	36 Q*/W	37 TD/K	38 TU/K	39 N*/W	40 K*/W
41 AN/F	42 AK/F						
01 201	02 JD	03 HHMM	04 TST	05 WD	06 WS	07 MAX-WD	08 TMXHM
09 TMXSS	10 MAX-WS	11 TMXHM	12 TMXSS	13 MIN-WD	14 TMNHM	15 TMNSS	16 MIN-WS
17 TMNHM	18 TMNSS	19 SD-WD	20 SD-WS				
01 301	02 JD	03 HHMM	04 TST	05 M-ST1	06 M-ST2	07 M-ST3	08 M-ST4
09 M-SM1	10 M-SM2	11 M-SM3	12 M-SM4	13 M-AT	14 M-RH	15 SD-ST1	16 SD-ST2
17 SD-ST3	18 SD-ST4	19 SD-SM1	20 SD-SM2	21 SD-SM3	22 SD-SM4	23 SD-AT	24 SD-RH
25 BATT	26 RF						

JD = Julian Day
HHMM = Hour-Minutes
TST = Table Sampling Time (tenths of second)
ND = NIRSOL Downward Radiation
KD = TOTSOL Downward Radiation
NU = NIRSOL Upward Radiation
KU = TOTSOL Upward Radiation
LD = TOTIR Downward Radiation
LU = TOTIR Upward Radiation
Ts = Pyrgeometer Sink Temp
Td = Pyrgeometer Dome Temp
VD = KD - ND = VISSOL Downward Radiation
VU = KU - NU = VISSOL Upward Radiation
V* = VU - VD = VISSOL Net Radiation
N* = NU - ND = NIRSOL Net Radiation
K* = KU - KD = TOTSOL Net Radiation
AV = VU/VD = VISSOL Albedo
AN = NU/ND = NIRSOL Albedo
AK = KU/KD = TOTSOL Albedo
L* = LU - LD = TOTIR Net Radiation
Q* = K* + L* = Total Net Radiation
TU = $(LU/SIG)^{.25}$ = Upward EBBT
TD = $(LD/SIG)^{.25}$ = Downward EBBT
SIG = 5.67E-8 = Stefan Boltzman's Constant
K = Kelvin Degrees
F = Fractional Albedo
W = W/M^2
MV = Millivolts
V = Volts
WD = Wind Direction (degrees - 0 to 360)
WS = Wind Speed (m/sec)
M = Mean
SD = Standard Deviation
MAX = Maximum Value
MIN = Minimum Value
TMXHM = Time of Max (hour:minutes)
TMXSS = Time of Max (seconds)
TMNHM = Time of Min (hour:minutes)
TMNSS = Time of Min (seconds)
ST = Soil Temperature (Deg C)
SM = Soil Moisture (Bars)
AT = Air Temperature (Deg C)
RH = Relative Humidity (Percent)
BATT = Battery Level (Volts)
RF = Total Rainfall (mm)

For Soil Levels

1 = Top Level
2 = Second Level
3 = Third Level
4 = Bottom Level

TOWER STATION
CR-7W OUTPUT TABLE 3

01 201	02 JD	03 HHMM	04 TST	05 M-T0	06 M-q0	07 V-T0	08 V-q0
09 SD-T0	10 SD-q0	11 M-W1	12 M-U1	13 M-V1	14 M-T1	15 M-q1	16 V-W1
17 V-U1	18 V-V1	19 V-T1	20 V-q1	21 SD-W1	22 SD-U1	23 SD-V1	24 SD-T1
25 SD-q1	26 CV-WU1	27 CV-WV1	28 CV-WT1	29 CV-Wq1	30 CV-UV1	31 CR-WU1	32 CR-WV1
33 CR-WT1	34 CR-Wq1	35 CR-UV1	36 SH1	37 LH1	38 M-W2	39 M-U2	40 M-V2
41 M-T2	42 M-q2	43 V-W2	44 V-U2	45 V-V2	46 V-T2	47 V-q2	48 SD-W2
49 SD-U2	50 SD-V2	51 SD-T2	52 SD-q2	53 CV-WU2	54 CV-WV2	55 CV-WT2	56 CV-Wq2
57 CV-UV2	58 CR-WU2	59 CR-WV2	60 CR-WT2	61 CR-Wq2	62 CR-UV2	63 SH2	64 LH2
65 M-W3	66 M-U3	67 M-V3	68 M-T3	69 M-q3	70 V-W3	71 V-U3	72 V-V3
73 V-T3	74 V-q3	75 SD-W3	76 SD-U3	77 SD-V3	78 SD-T3	79 SD-q3	80 CV-WU3
81 CV-WV3	82 CV-WT3	83 CV-Wq3	84 CV-UV3	85 CR-WU3	86 CR-WV3	87 CR-WT3	88 CR-Wq3
89 CR-UV3	90 SH3	91 LH3	92 BATT	93 DEN	94 PRES	95 es1	96 es2
97 es3	98 es0						

JD = Julian Day
HHMM = Hours-Minutes
TST = Table Sampling Time (tenths of second)
M = Mean
V = Variance
SD = Standard Deviation
CV = Covariance
CR = Correlation
T(n) = Temperature at Level n (Deg C)
q(n) = Specific Humidity at Level n (gm/Kg)
W(n),U(n),V(n) = Orthogonal Wind Components (m/sec)
SH = Eddy Flux of Sensible Heat (W/m^2)
LH = Eddy Flux of Latent Heat (W/m^2)
BATT = Battery Level (Volts)
DEN = Density (KG/m^3)
PRES = Ambient Pressure (Kilo-Pascals)
es(n) = Saturation Vapor Pressure (Kilo-Pascals)

For Atmospheric Levels

0 = Surface Level (0 Meters)
1 = First Level (2 Meters)
2 = Second Level (4 Meters)
3 = Top Level (8 Meters)

abcissa indicate local midnight). The winter data in Fig. 33a show that the dominant down valley winds follow the valley axis at 210-240° (i.e., southwest). Upslope winds, when they occur, appear to center around 90° (east). The easterly flow on JD 78 was associated with a large low pressure system passing to the south and snow fell at the site. The strong winds on JD 74 were accompanied by gusts greater than 30 m/s which damaged the wind tower sensors. Intermittent up-valley winds can be observed briefly on a number of afternoons in the summer data. However, as shown in the diurnally-averaged data (Fig. 34b) the upslope winds do not occur regularly enough to significantly perturb the mean down-valley direction for any time of day.

The winds at the Storm Peak site, in contrast to Pingree Park, show pronounced diurnal cycles of both speed and direction. Close inspection of Fig. 35 reveals abrupt late-afternoon shifts of wind direction from west or west-northwest to southeast. This shift was often accompanied by an equally abrupt increase in wind speed. Distinct occurrences of this shift can be observed on at least 24 of the 34 days of the measurement program. Diurnally-averaged wind speeds and directions for the first 13 days of the program are shown in Fig. 36. The vector-averaged winds in Fig. 36c, when compared with the normalized direction frequencies in Fig. 36b, further illustrate the close association between the shifts of speed and direction. Also, whereas maximum wind speeds at Pingree Park tend to occur during the day (Fig. 34a), strongest average winds at Storm Peak occurred during the nighttime hours (Fig. 36a). Details of Storm Peak winds for JD 217-219 are shown in Fig. 37.

During daylight hours the mean winds at Storm Peak were from the west; consistent with upslope flow following the east-west Yampa River

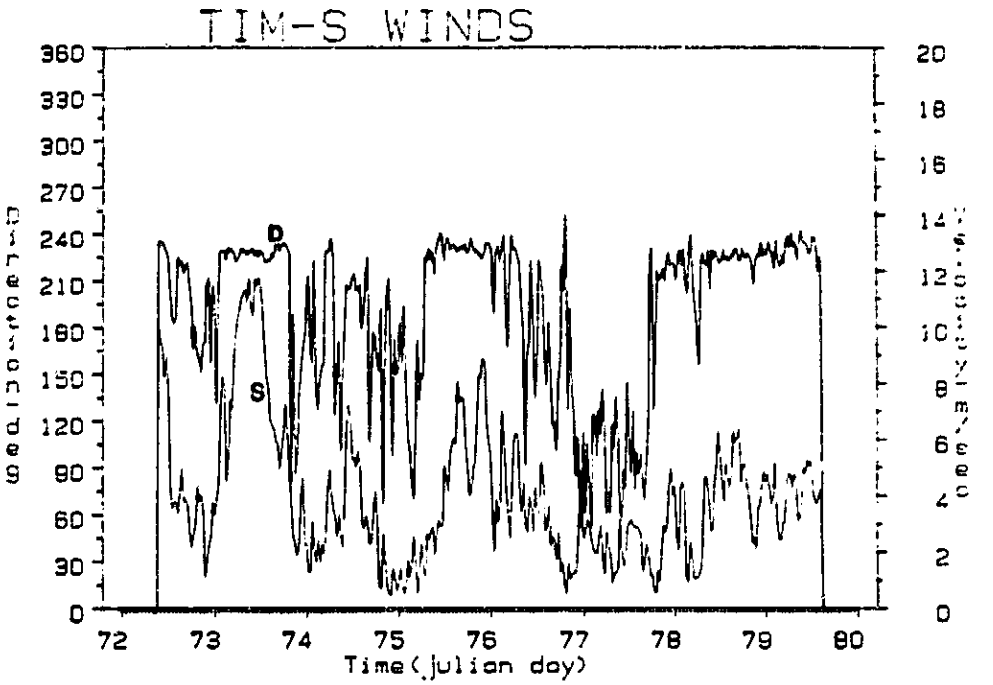

Figure 33a. Time series of wind speed and direction at Pingree Park for JD 73-80.

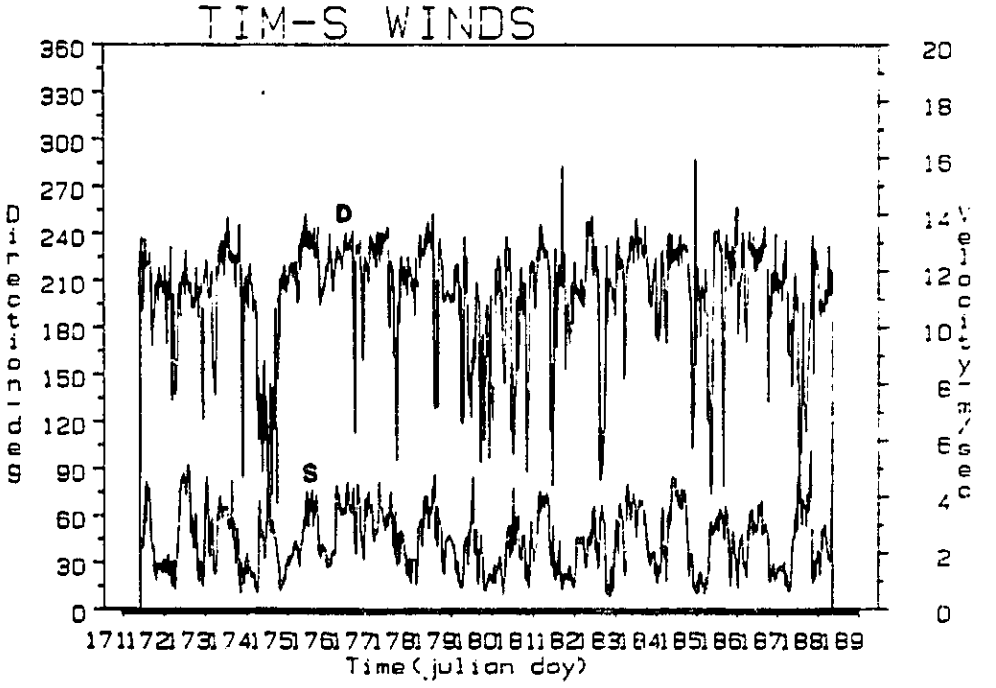

Figure 33b. As in Fig. 33a but for JD 172-189.

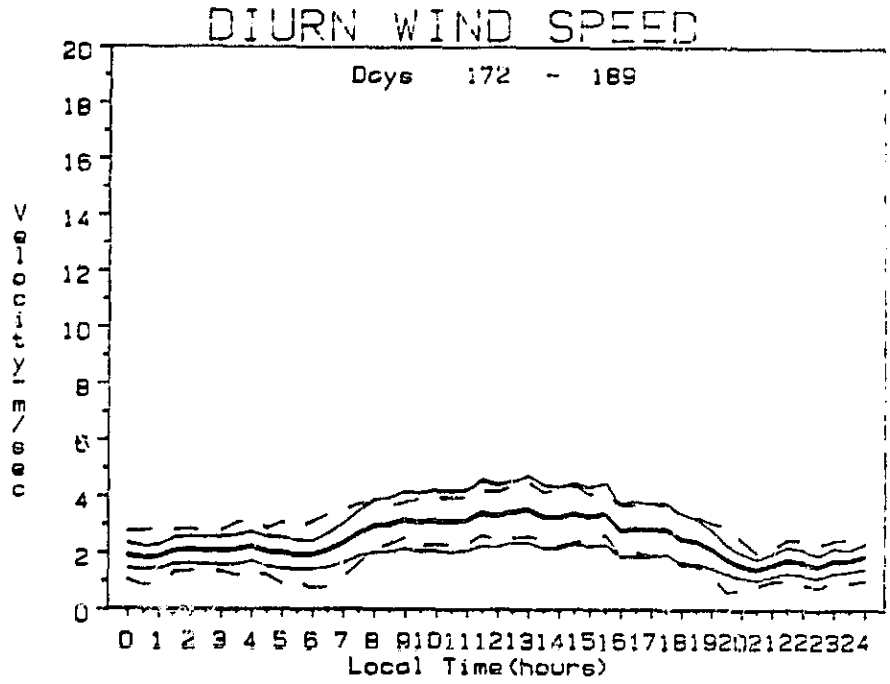

Figure 34a. Diurnal average wind speed at Pingree Park for JD 172-189.

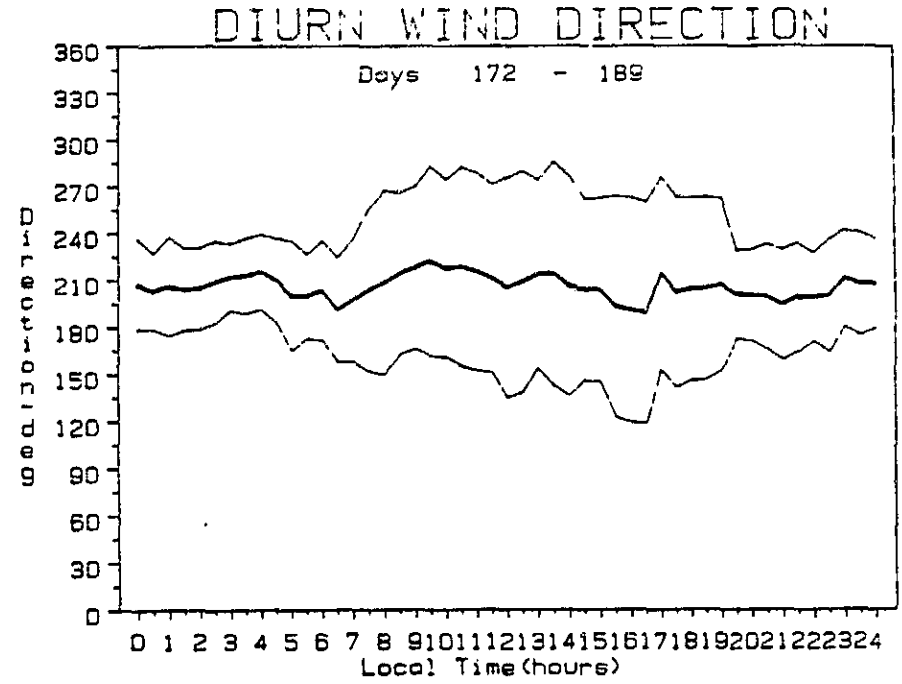

Figure 34b. Diurnal average wind direction at Pingree Park for JD 172-189. These values represent normalized vector averages wherein all speed values were set equal to 1.0 m/s.

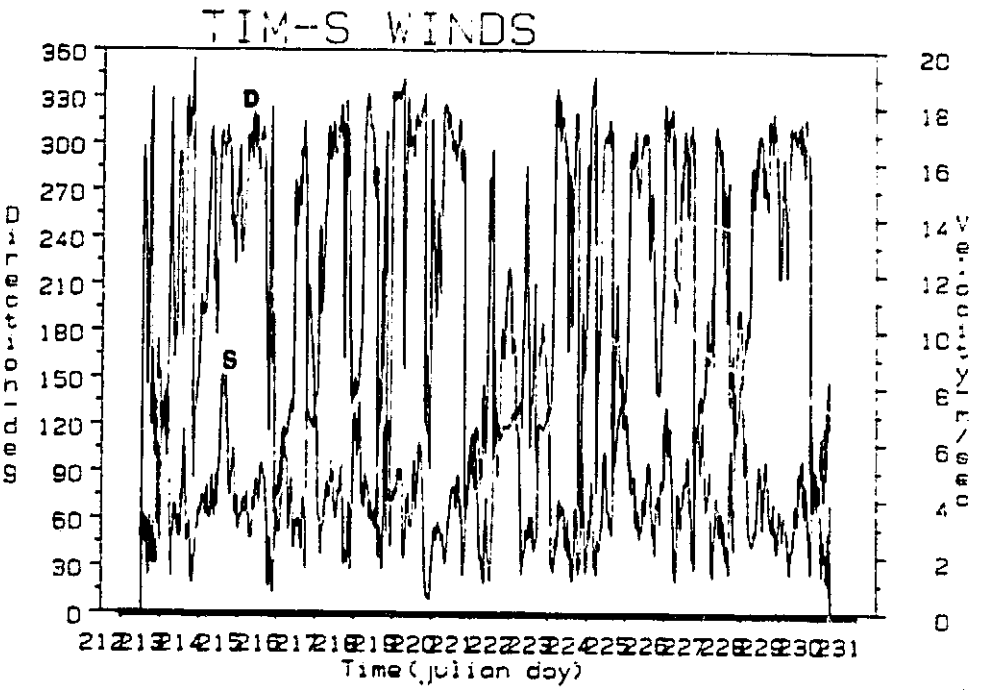

Figure 35a. Wind speed and direction at Storm Peak for JD 213-231.

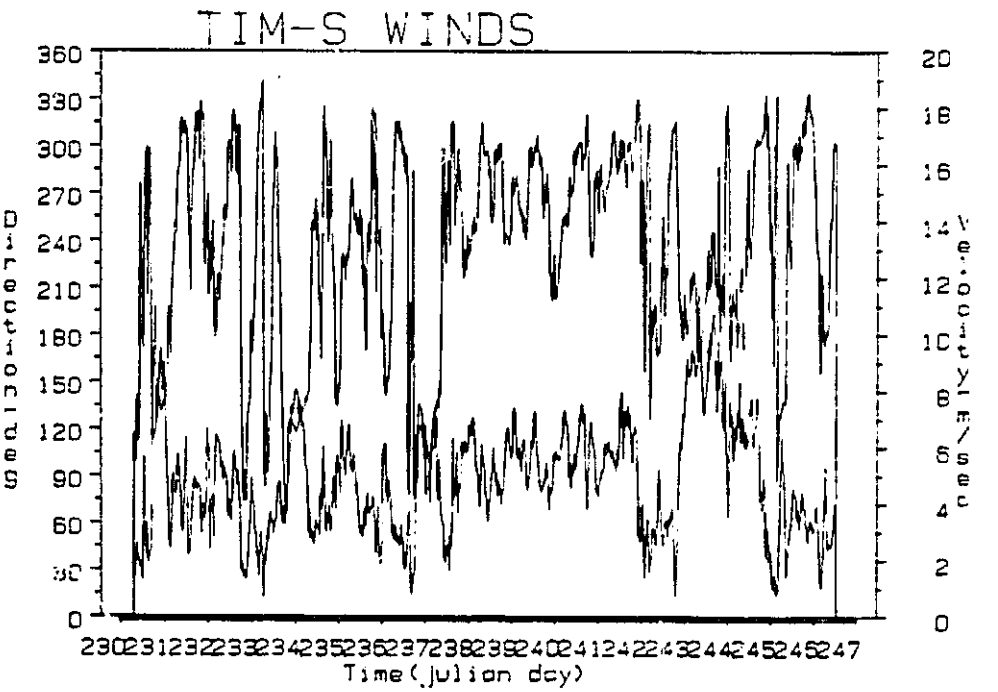

Figure 35b. As in Fig. 35a but for JD 231-247.

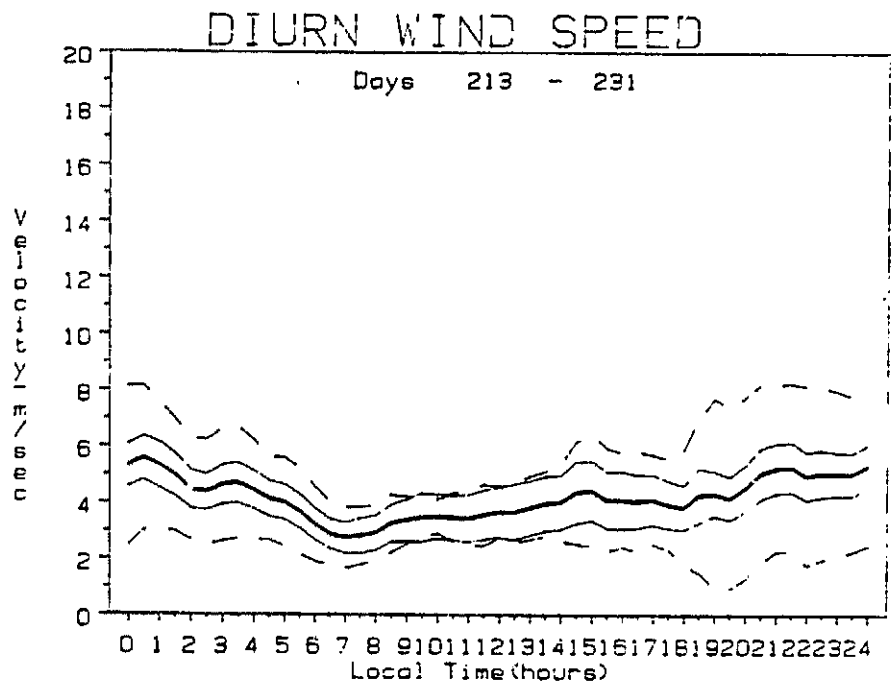

Figure 36a. Diurnal average wind speed at Storm Peak for JD 213-231.

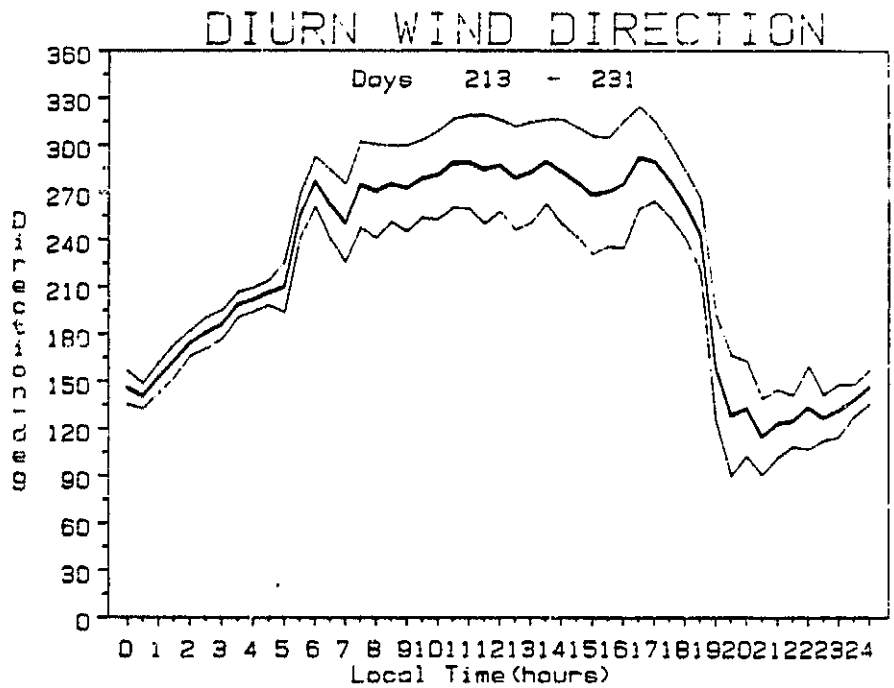

Figure 36b. Normalized vector average wind direction at Storm Peak for JD 213-231.

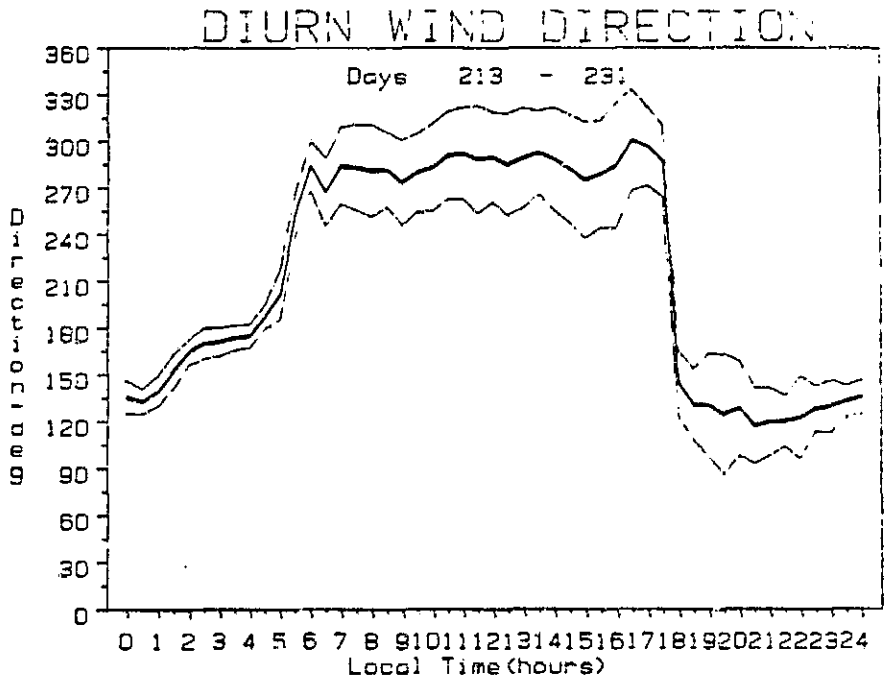

Figure 36c. Vector average wind direction at Storm Peak for JD 213-231.

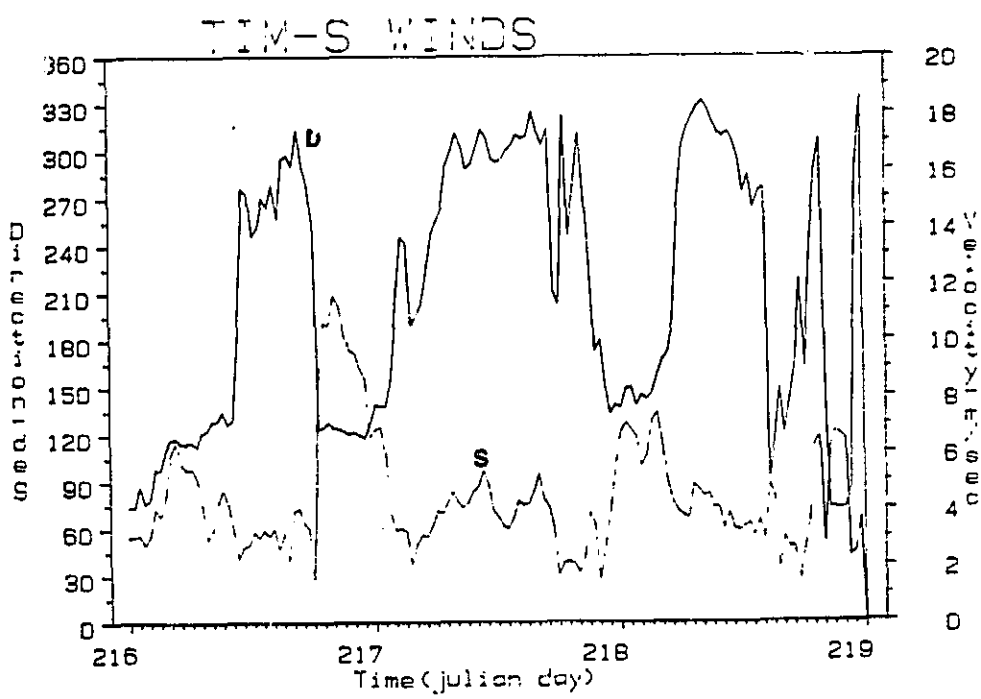

Figure 37. Wind speed and direction at Storm Peak for JD 217-219.

Valley which begins at the base of the montain and runs westward for nearly 200 km. The sudden shift to the southeast typically begins about one hour before sunset and, because the Storm Peak site is on a mountain top which dominates the surrounding terrain for 50 to 100 km, we cannot ascribe the brisk nocturnal winds to a simple slope flow. Moreover, nocturnal slope flows are characteristically intermittent in contrast to these abrupt wind maxima which slowly decrease over a period of five to ten hours.

Presently, the best explanation for these winds may be that offered by Reiter and Tang (1984) who show evidence for diurnal development of a series of meso-highs and lows over the major highland and basin areas of the western plateau. Simply stated, these winds are the result of strong heating over elevated terrain causing strong inflow of air by day and a reversal to a return outflow at night. Whereas daytime inflow is accompanied by strong vertical mixing and is easily observed in surface synoptic data, the main effects of the outflow occur above low-level inversions which develop rapidly after strong heating has ceased. Hence, because essentially all weather stations in the region are in locally controlled valley settings, these winds are not normally observed at the surface. Several additional observations support this analysis. First, the intensity of the southeast winds tends to be greatest when stationary upper level (500 mb) high pressure was centered over the region. Secondly, the Storm Peak site is located approximately 150 km northwest of the primary highland area in the region. Hence, the observed trends in speed and direction (Fig. 36) are consistent with an initial cross-isobaric outflow followed by a gradual adjustment to geostropic flow.

The diurnal range of summertime air temperature and humidity variations at the two sites are shown in Fig. 38. Whereas diurnal variations of air temperature at Pingree Park are frequently 20°C or more, the range at Storm Peak is typically less than 10°C. An important factor contributing to the warmest temperatures at Pingree Park is adiabatic warming of downslope westerly winds as they descend from the 4000 meter heights immediately to the west. The association between westerly winds and warm temperatures (and low humidity) can be observed by comparing Figs. 34b and 38a. The opposite adiabatic effect (cooling) contributes to the comparatively cool daytime temperatures and higher humidities at Storm Peak (Fig. 38b) where westerly winds abruptly rise nearly 1000 meters from the Yampa River Valley.

c. Comparative Energy Balance Components

Time series of the comparative radiative components for several cloud free days at each site are shown in Fig. 39. The spring data for Pingree Park (JD 104-107) show the influence of melting snow cover. The radiation station was situated on a local high point and the snow cover directly below the downward looking radiometers tended to be somewhat thinner than in the low sheltered area five to ten meters downwind to the east. Hence, the snow cover below the radiometers dissipated more rapidly and a strong diurnal bias appeared in the total reflectance curve. This is especially noticeable in the data for JD 107.

Diurnally-averaged data for radiant fluxes, albedo, EBB temperature, and net radiation are shown in Figs. 40 to 42. The fairly large differences between the incoming near infrared (NIR) and visible (VIS) flux (Fig. 40) are consistent with high altitude observations reported by Kondratyev (1969). These differences are strongest for the

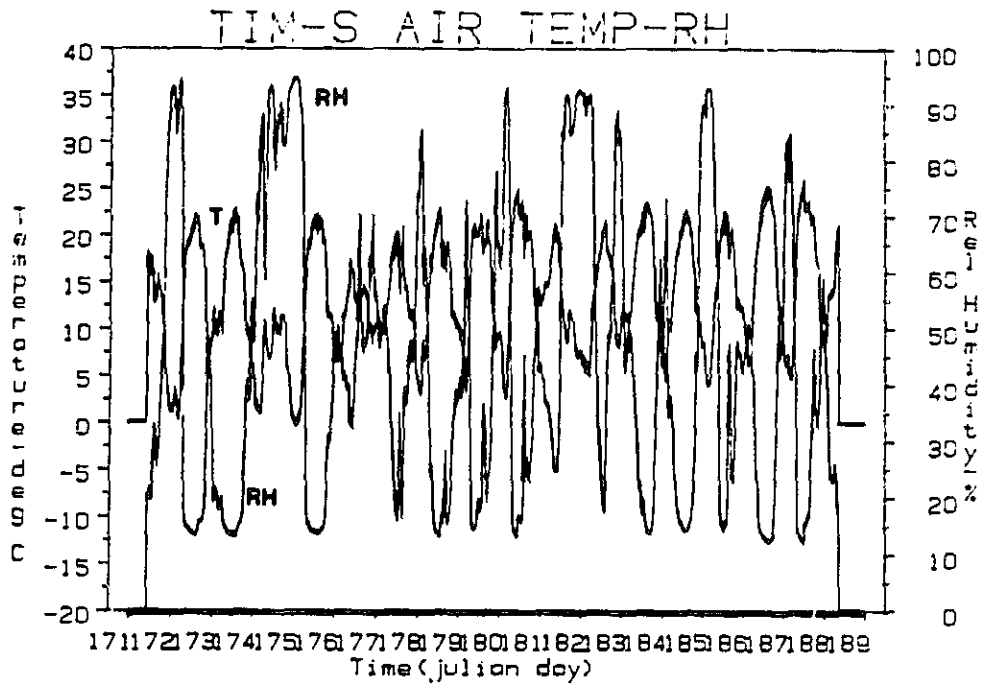

Figure 38a. Time series of air temperature and relative humidity at Pingree Park for JD 172-189.

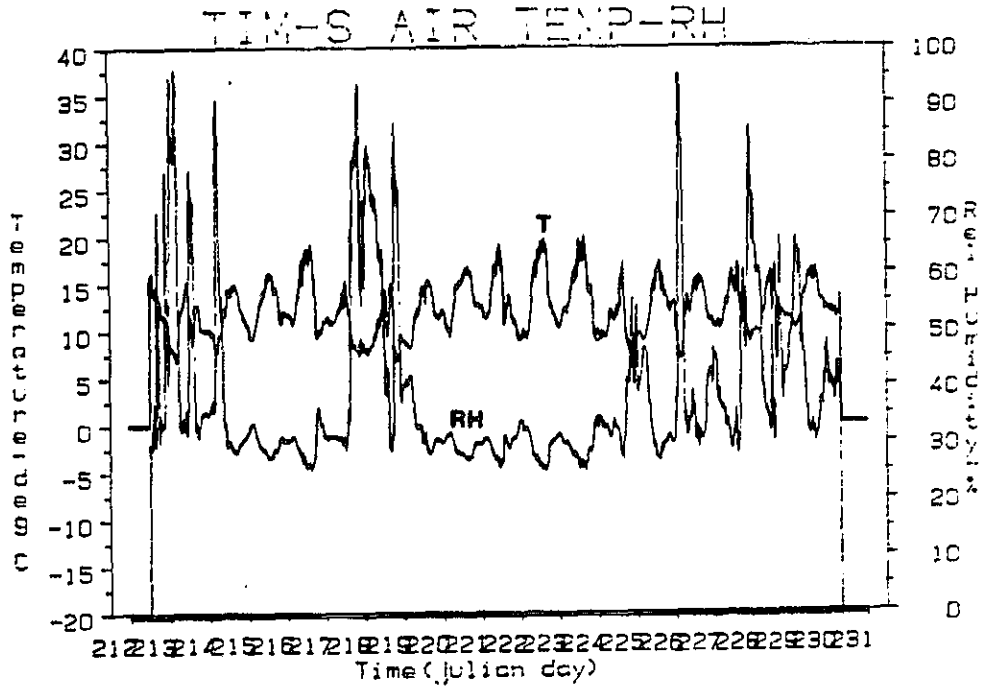

Figure 38b. As in Fig. 38a but for Storm Peak, JD 213-231.

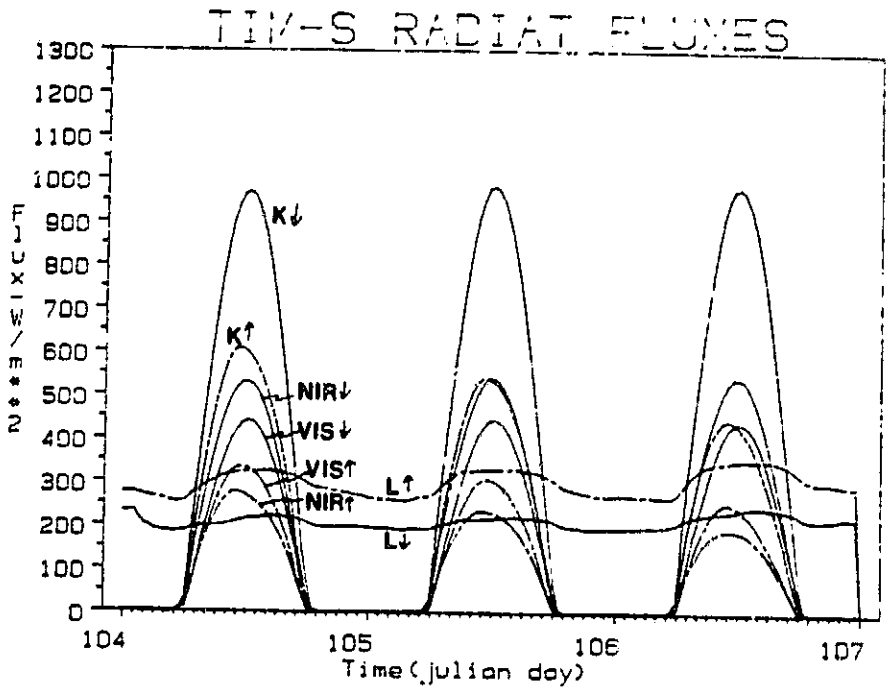

Figure 39a. Time series of solar and terrestrial radiation fluxes during three cloud free days at Pingree Park (JD 105-107).

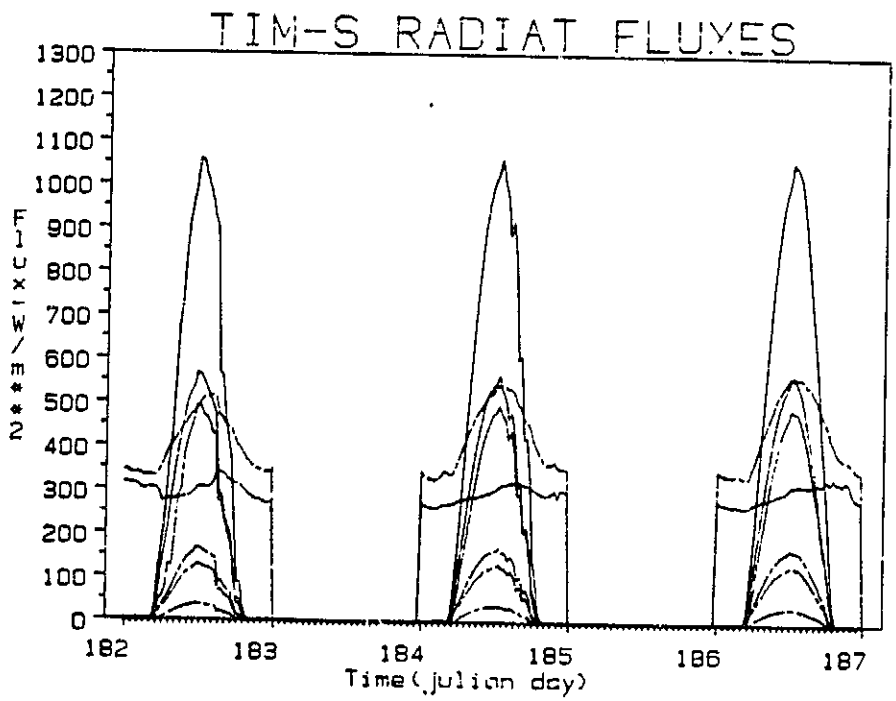

Figure 39b. As in Fig. 39a but for JD 183, 185 and 187.

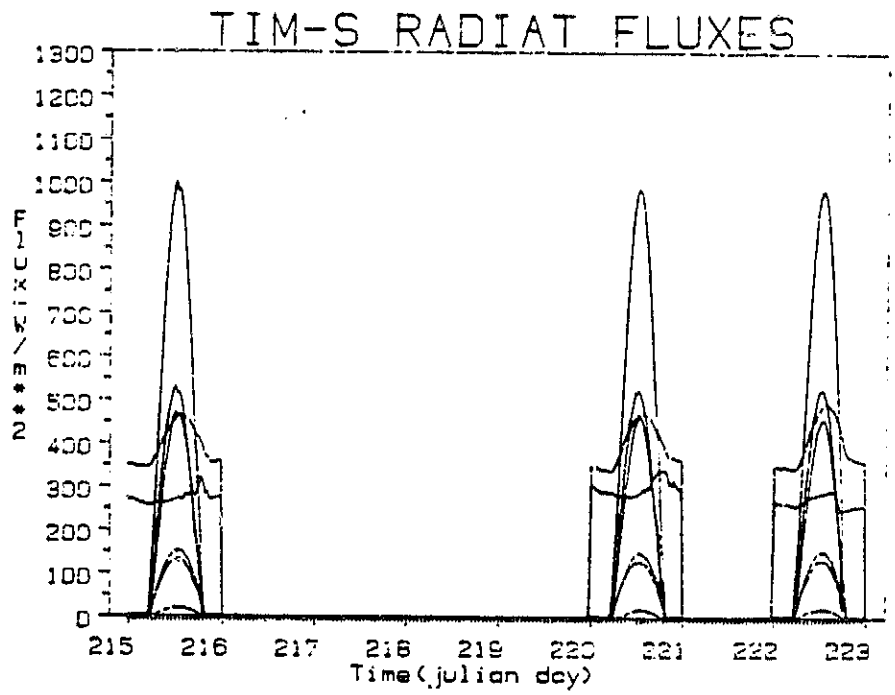

Figure 39c. As in Fig. 39a but at Storm Peak for JD 216, 221 and 223.

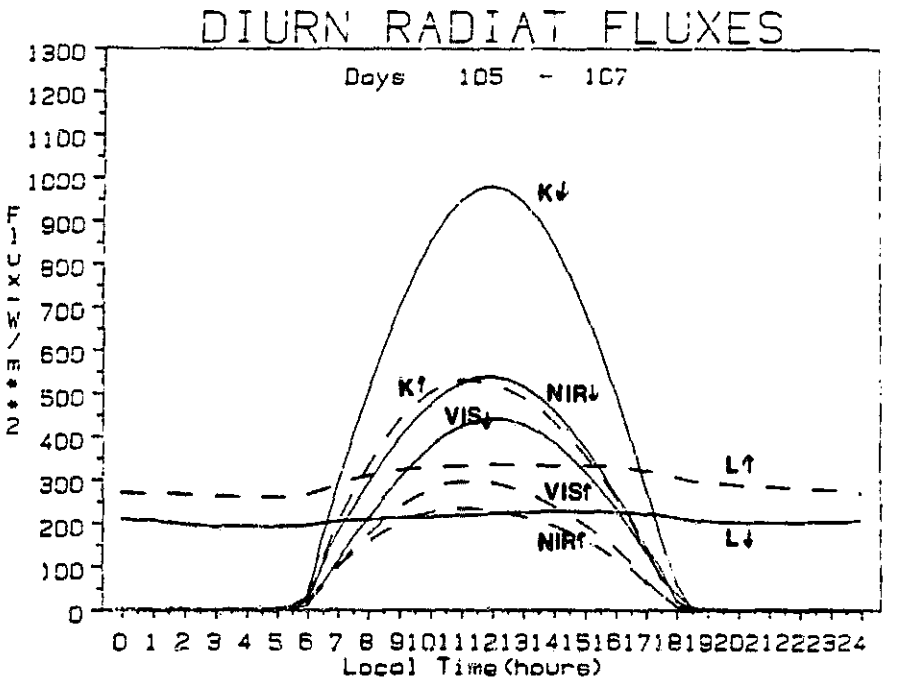

Figure 40a. Diurnal average solar and terrestrial radiation fluxes at Pingree Park for JD 105-107.

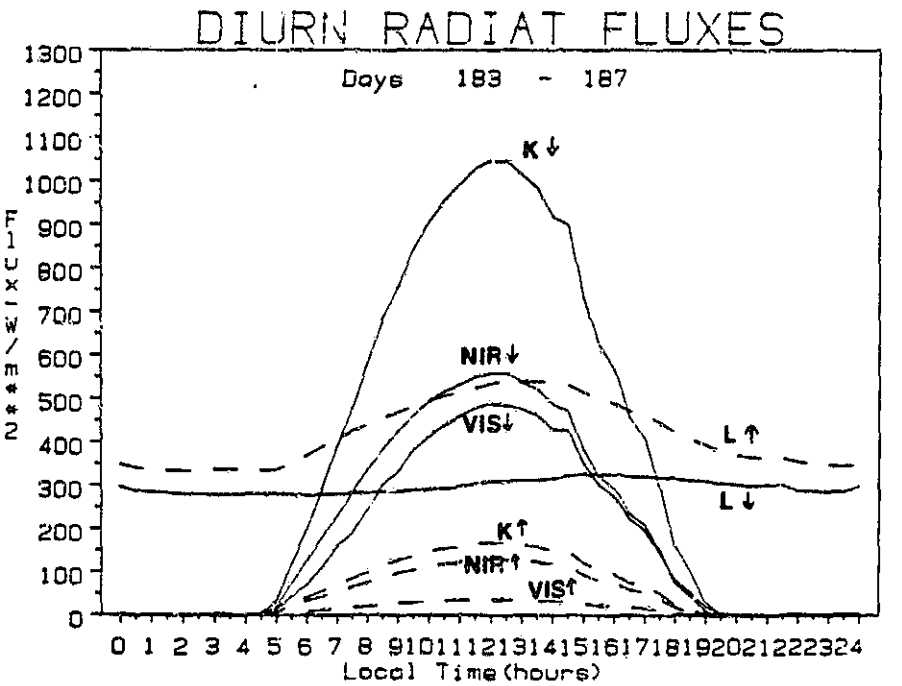

Figure 40b. As in Fig. 40a but for JD 183, 185 and 187.

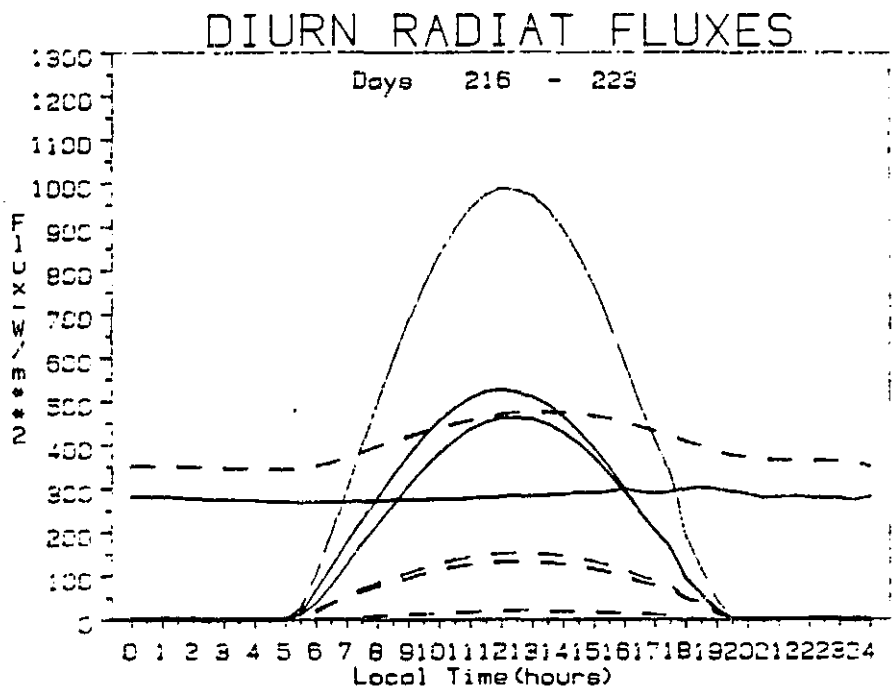

Figure 40c. As in Fig. 40a but at Storm Peak for JD 216, 221 and 223.

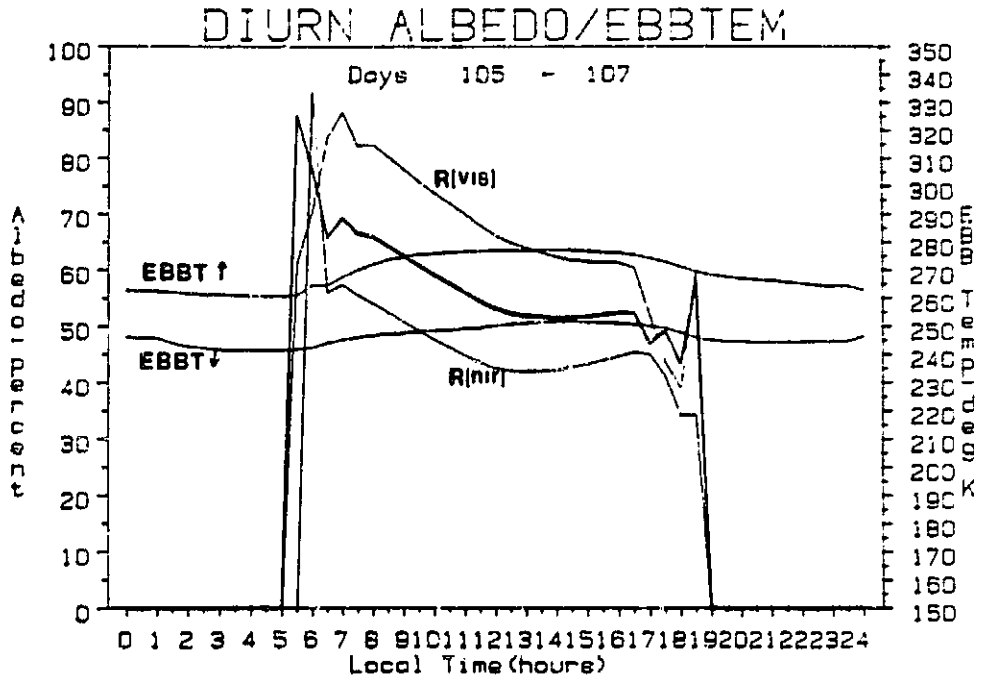

Figure 41a. Diurnally-averaged directional reflectance (albedo) and EBBT at Pingree Park for JD 105-107.

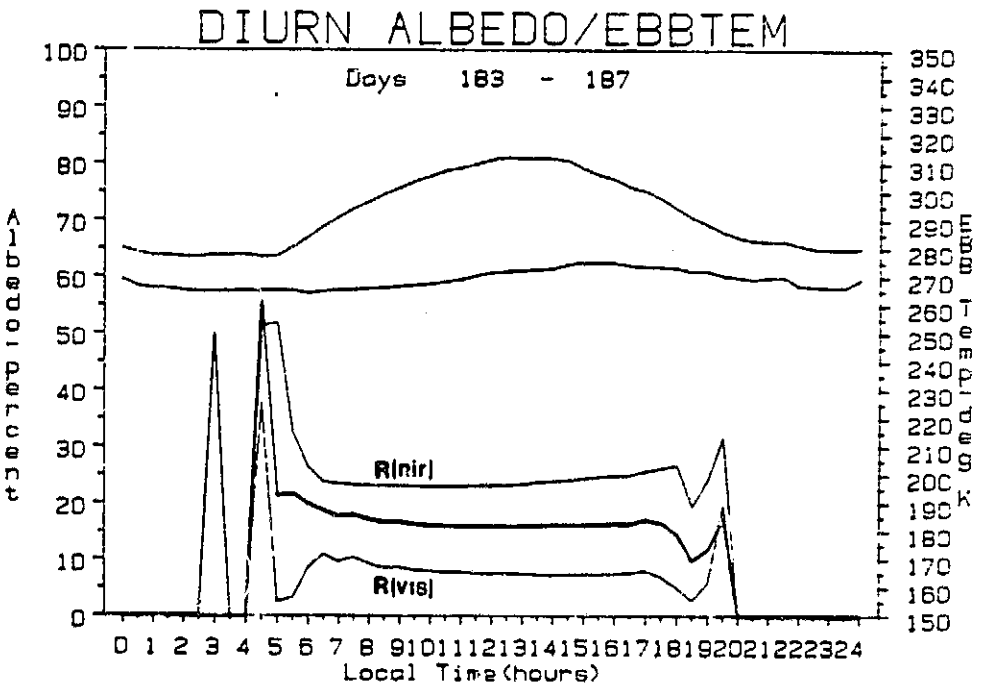

Figure 41b. As in Fig. 41a but for JD 183, 185 and 187.

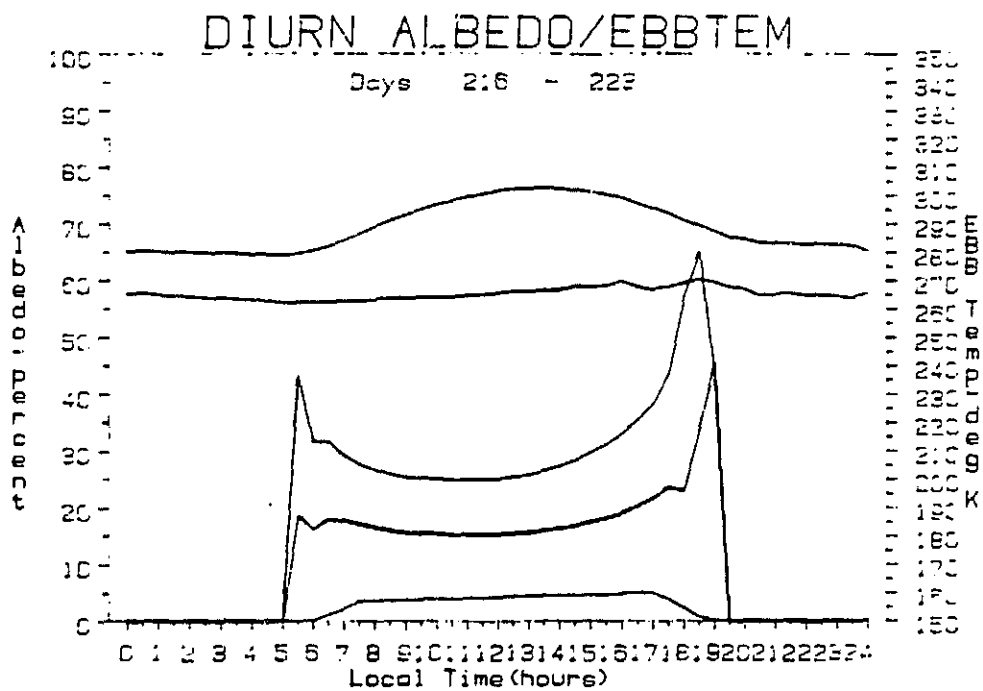

Figure 41c. As in Fig. 41a but at Storm Peak for JP 216, 221 and 223.

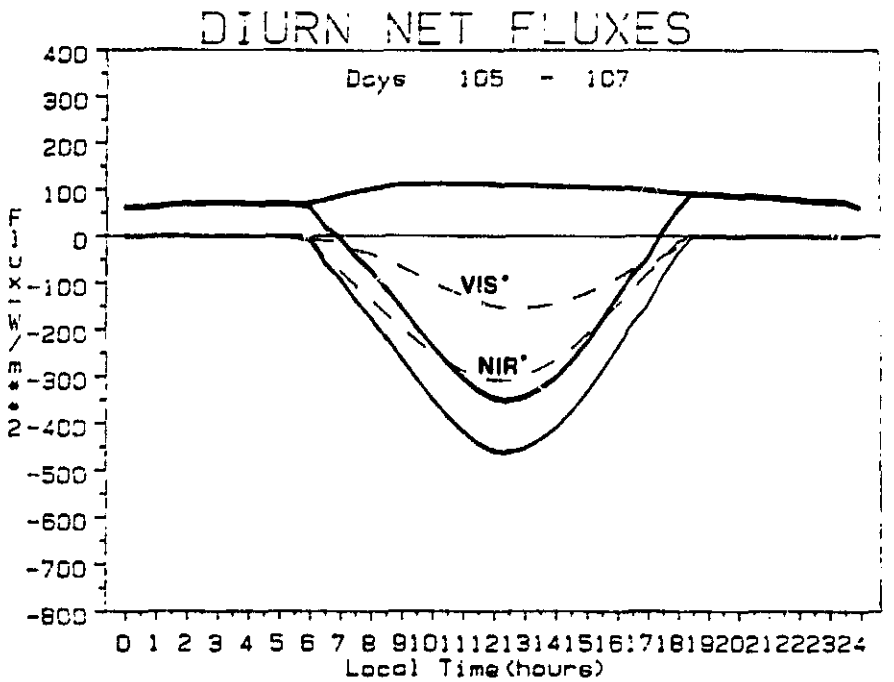

Figure 42a. Diurnally-averaged net radiation terms at Pigree Park for JD 105-107.

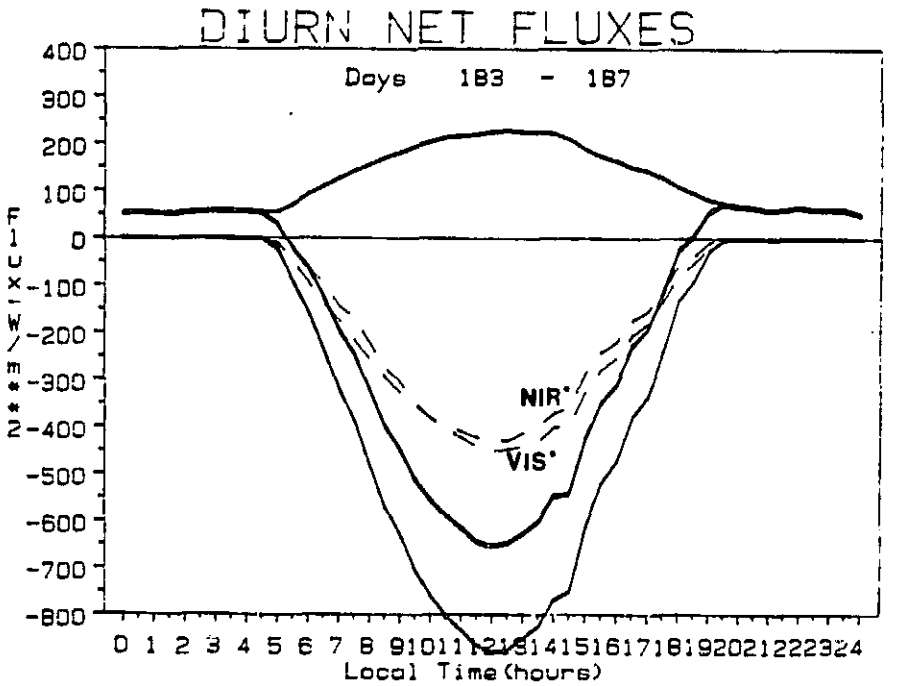

Figure 42b. As in Fig. 42a but for JD 183, 185 and 187.

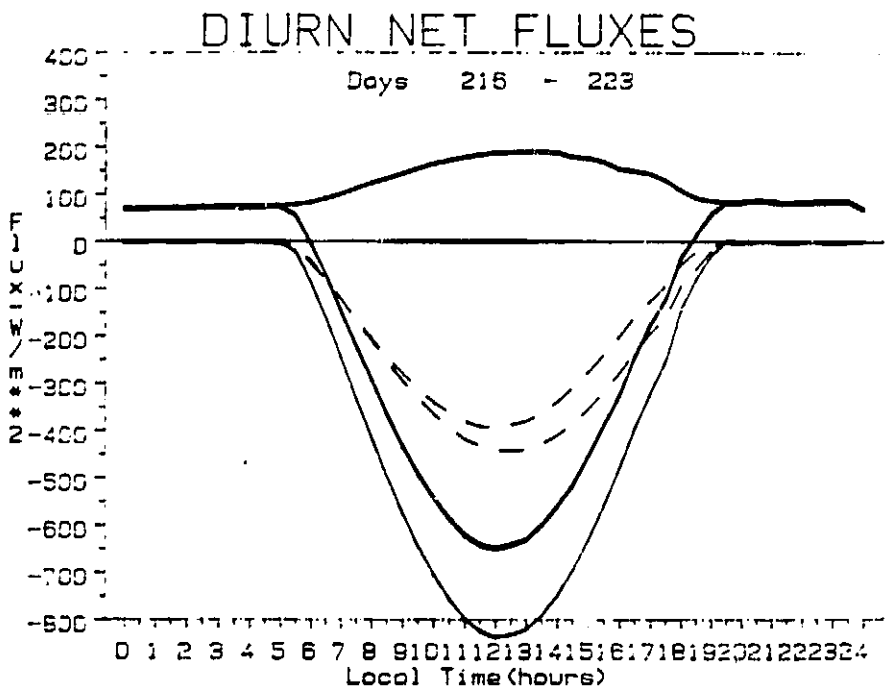

Figure 42c. As in Fig. 42a but at Storm Peak for JD 216, 221 and 223.

spring period (JD 105-107) when dry downslope winds and a dry overlaying winter air mass allowed a comparatively undepleted NIR flux to penetrate to the surface throughout the period. The summer data show a smaller difference between these two wave bands due to the presence of greater moisture throughout the atmosphere during the warm season. (For the same cloudless conditions, even smaller differences were observed in the Gobi, due primarily to the combined influence of moisture and lower elevation.) The cumulative effects of strong daytime convection over the mountains during the summer season lead to a comparatively moist afternoon boundary layer relative to morning conditions. This in turn results in greater absorption of incoming NIR flux during the afternoon and the notable decrease in the difference between incoming NIR and VIS during the day (Figs. 40b and c).

The snow cover represented in Figs. 39-42 (JD 105-107) was relatively old. The albedo of fresh snow cover for visible radiation was consistently greater than 90 percent and decayed to 60 to 70 percent as the snow aged. Observed snow albedos for near infrared radiation ranged between 60 to 70 percent. During the summer season the broadband (0.2-4.0μm) albedo was approximately 16 percent for both Pingree Park and Storm Peak. However, the comparative visible and near infrared albedos were 8 and 23 percent, respectively, at Pingree Park and 4 and 26 percent, respectively, at Mt. Warner. All of these albedo observations are consistent with widely reported values (Kondratyev et al., 1981; Kondratyev, 1969; McClatchey et al., 1971) for the surface cover elements in each area as described in the previous section.

Opposite trends in the directional bias of the near infrared albedo are observed in the summer data for the two sites shown in Fig. 41b and

c. Allowing that this bias is not due to radiometer alignment, the only common factor that might, in some way, explain this phenomenon is that the site at Pingree Park has notably more open exposure to the east whereas the Storm Peak site was more open to the west.

In Fig. 42a both the absorbed total solar radiation and the net radiative flux are strongly supressed by the snow cover. Although the summertime solar radiation absorbed at Pingree Park (Fig. 42b) exceeds that at Storm Peak (Fig. 42c), the net flux curves are effectively equal; this owing to stronger emitted surface long wave radiation at Pingree Park and, hence, the higher EBBT values in Fig. 41b.

Differing trends in soil temperature and moisture at the two sites provide another important contrast (Fig. 43). The thin layer of plant litter on the surface at Pingree Park was an effective barrier, inhibiting both thermal and moisture flux to the soil. Whereas the amplitude of the 2 cm temperature wave at Pingree Park rarely exceeded 7°C, variations of 20 to 25° occurred frequently at Storm Peak, even though the 2 cm soil thermometer at Storm Peak was placed directly under a small green plant and was at least partly shaded throughout the day. The insulating qualities of the surface litter at Pingree Park contributed to the notably higher EBBT values observed in Fig. 41b.

Soil moisture at Pingree Park did not depart from effective field capacity values at any time during the experiment. Because there was no indication of subirrigation at this site we must assume that the plant litter on the soil surface, in combination with minimal requirements for plant transpiration, effectively inhibited the loss of soil moisture. Strong variations in the soil moisture as Storm Peak are shown in Fig. 44 where the upper level dried out completely on several occasions

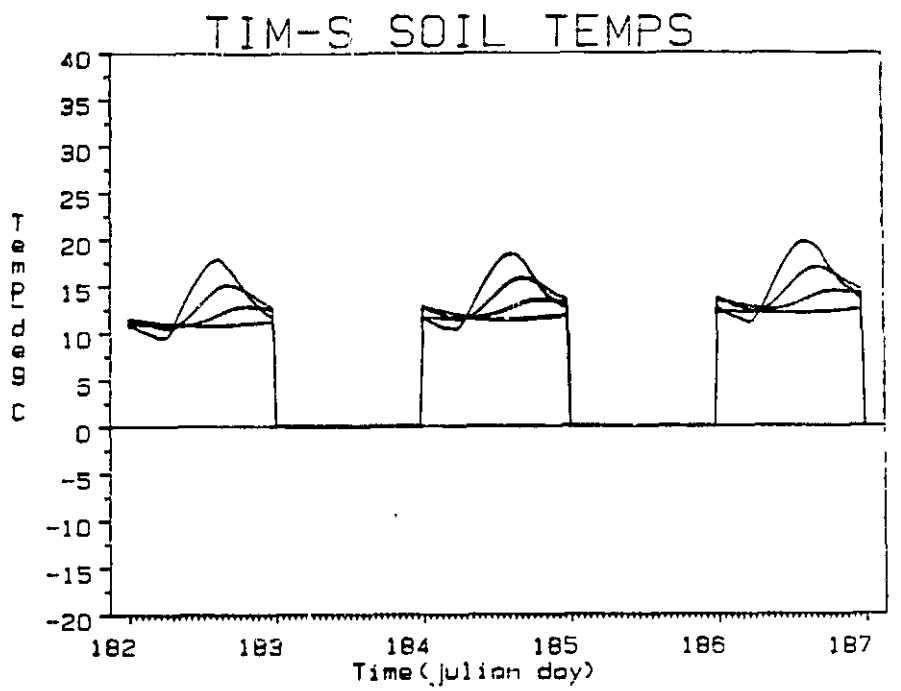

Figure 43a. Time series of soil temperature variation at Pingree Park for JD 183, 185 and 187.

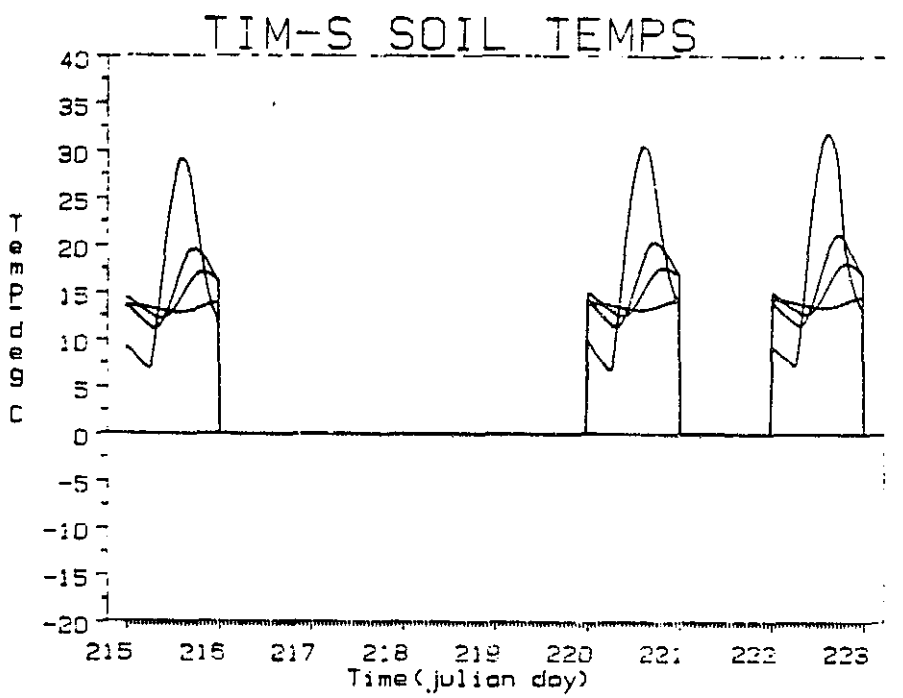

Figure 43b. As in Fig. 43a but at Storm Peak for JD 216, 222 and 223.

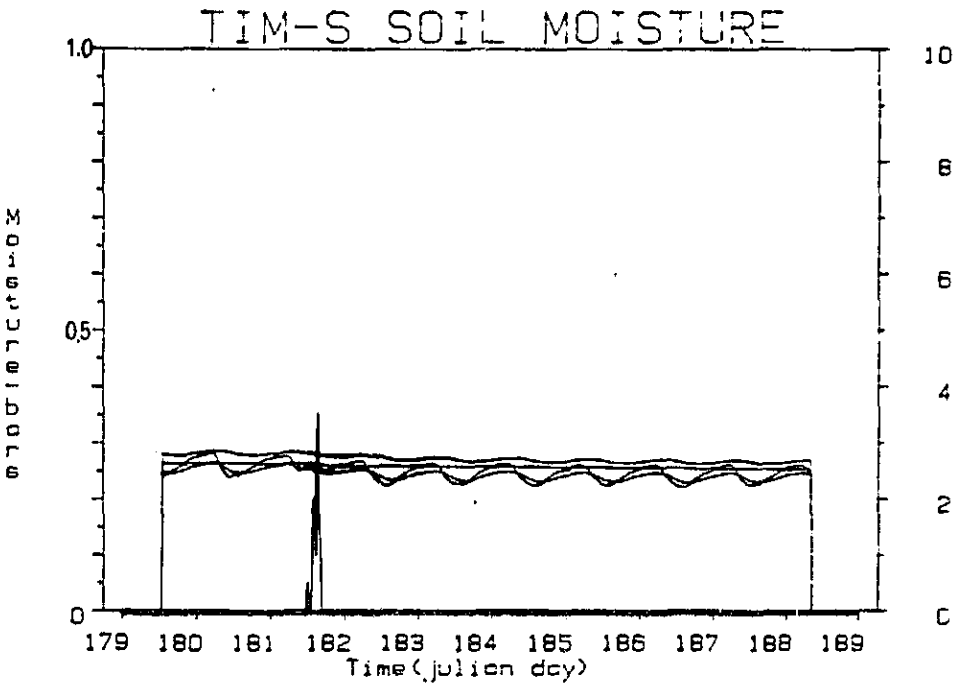

Figure 44a. Time series of soil moisture values at Pingree Park for JD 180-189. Note that the scale for the resistance potential on the left is expanded by a factor of ten relative to that in Figs. 20, 44b and 45b.

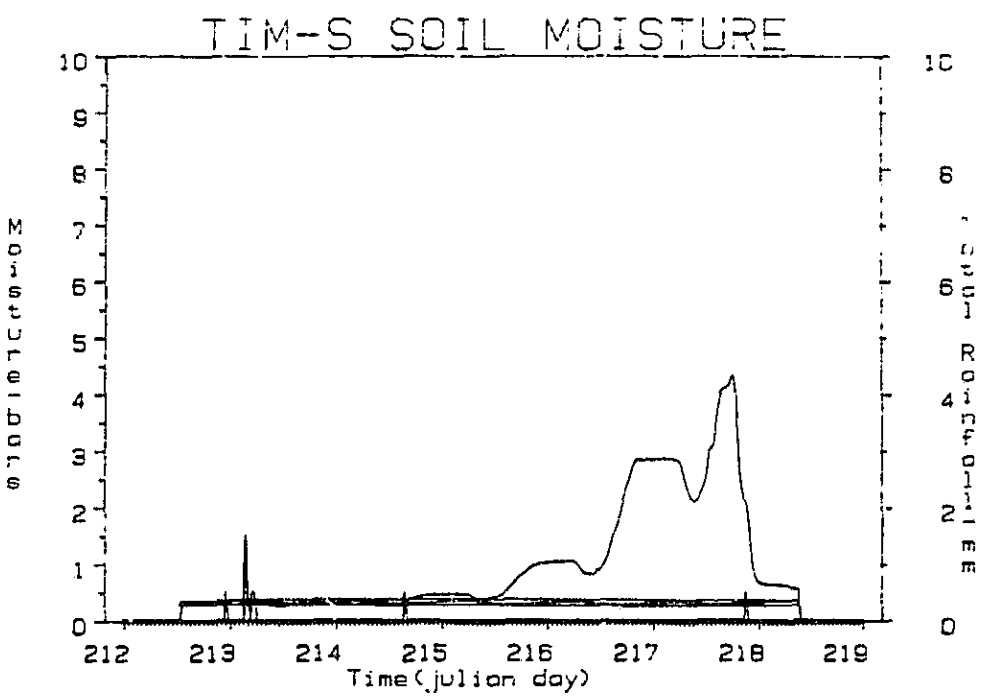

Figure 44b. As in Fig. 44a but at Storm Peak for JD 213-219.

during the study. The important contribution of distillation processes to the drying of the soil can be observed in Figs. 44 and 45. The upper soil appears to dry out in the late afternoon and evening, remains at a nearly constant value overnight and, beginning just after sunrise. becomes slightly wetter and reaches a maximum by midmorning (Fig. 45b). What occurs is that strong thermal drying of the surface in the afternoon is followed by an upward flux of water vapor from the warm subsoil when the soil surface cools rapidly after sunset. This process slows as an equilibrium is obtained between the surface, the soil and the air. As the soil surface warms after sunrise some of the accumlated moisture at the surface is lost to the atmosphere and some moves down to the now comparatively cool subsoil. The morning maximum of soil wetness at 2 cm in Fig. 45b coincides with the time of peak heating at this same level. The actual wetness maximum may occur somewhat earlier but appears slightly later due to the time constant of the soil moisture sensors. This same effect can also be observed in the Gobi data (Fig. 20) and at Pingree Park when the scale of the ordinate is greatly expanded (Fig. 44a).

A surface effect observed only at Pingree Park is thermal insulation by snow cover. During intermittent testing of the monitors between JD 60 and 73 little snow cover was present at the site and soil temperatures were observed to vary between -3 to -5°C. Warm downslope winds between JD 73-75 caused a rapid warming of the soil to 0°C all the way down to the 40 cm level. In the subsequent 58 day period (JD 73-132) soil temperatures at all levels remained at 0°C while recurrent snowfall kept 10 to 50 cm of snow cover over the probes and ambient air temperature varied from about -15 to +20C. Between JD 128 and 133 snow

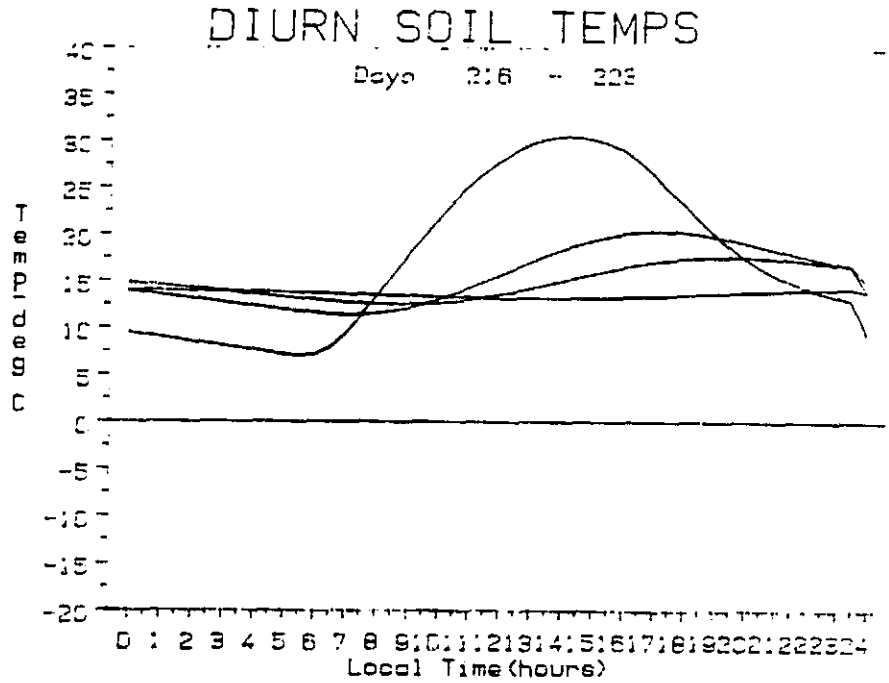

Figure 45a. Diurnal average of soil temperature at Storm Peak for JD 216, 221 and 223.

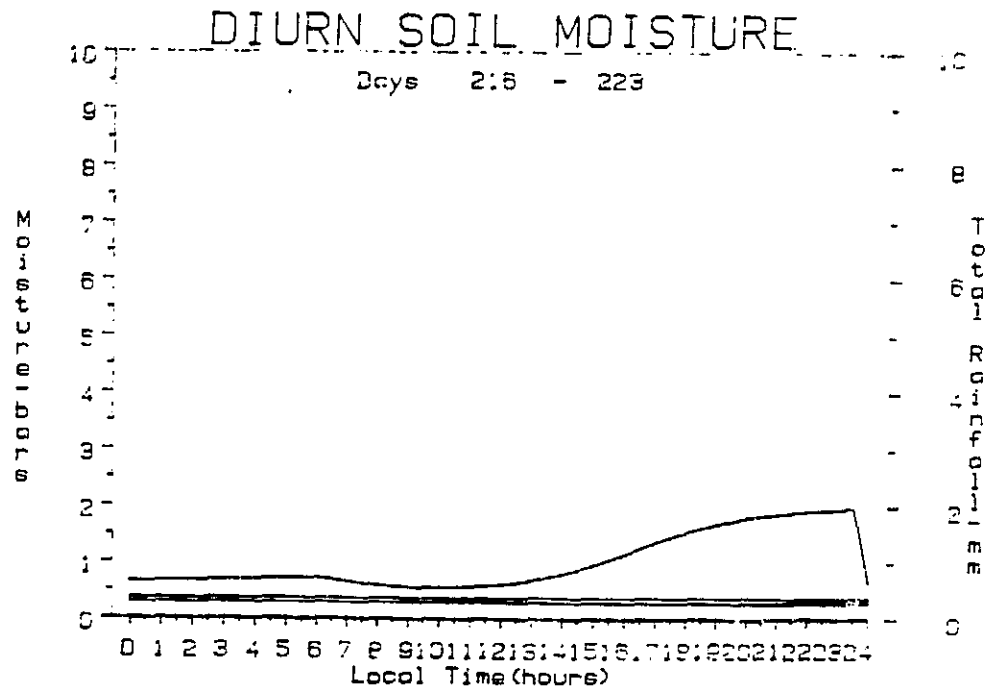

Figure 45b. As in Fig. 45a but for soil moisture.

cover at the site disappeared (Fig. 46) and within 5 days the soil thawed completely to 40 cm.

d. Estimates of Latent and Sensible Heat Fluxes

The turbulent flux data measured directly by the tower system appear to have some deficiencies which are described in the next section. Therefore, the results presented here were obtained using the bulk aerodynamic scheme described in the Appendix (Section A-3). Although this procedure, as noted previously, is rather crude it appears to be adequate for diagnosing the principal differences between the sites as well as short-term variations at each site.

The mean diurnal energy budgets for the three cloud free periods are shown in Fig. 47. The snow cover period (Fig. 47a) is interesting in that sensible heat fluxes are continuously negative with a daytime maximum of latent heat flux accompanying the melting and evaporation of snow. Soil heat flux beneath the snow is exactly zero for the period. Also, when nighttime surface (EBBT) temperatures fall well below freezing (Fig. 41a), the residual latent heat fluxes are negative, suggesting that the estimated drag coefficient of 1×10^{-3} may be a reasonable approximation of turbulent energy exchange for stable conditions in this mountain setting.

The important differences between the summertime surface energy balance at the two sites (Figs. 47b and c) are the notably larger values for the latent and soil heat fluxes at Storm Peak and the large sensible heat flux at Pingree Park. The morning maxima for the latent heat flux for both sites are at least "realistic" and the much smaller latent flux for Pingree Park is consistent with apparent conservation of soil moisture at that site.

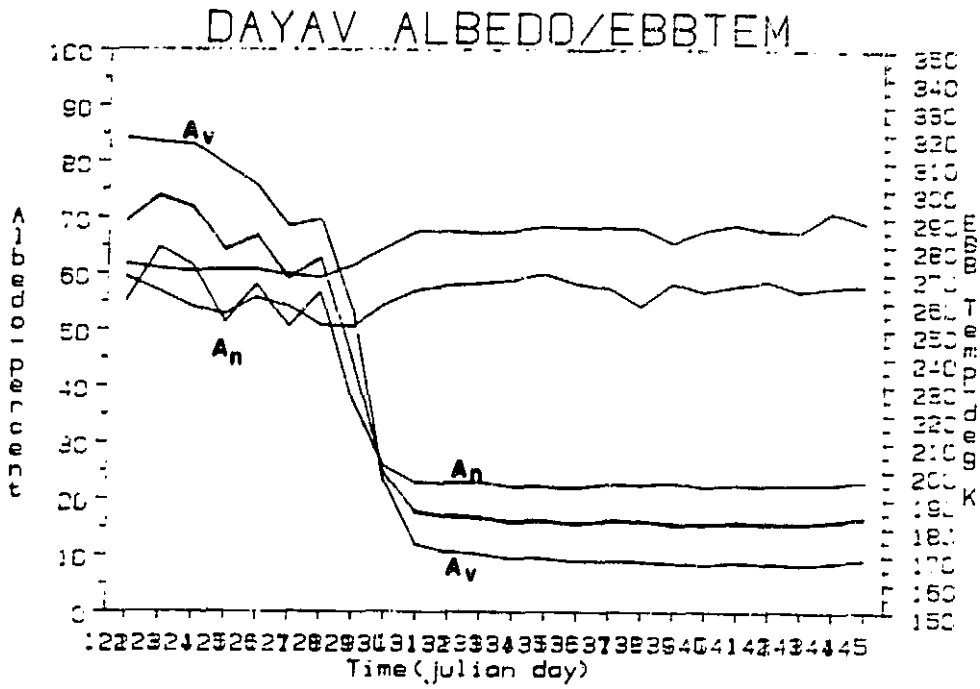

Figure 46a. Average daily albedo and EBBT at Pingree Park for JD 122-145.

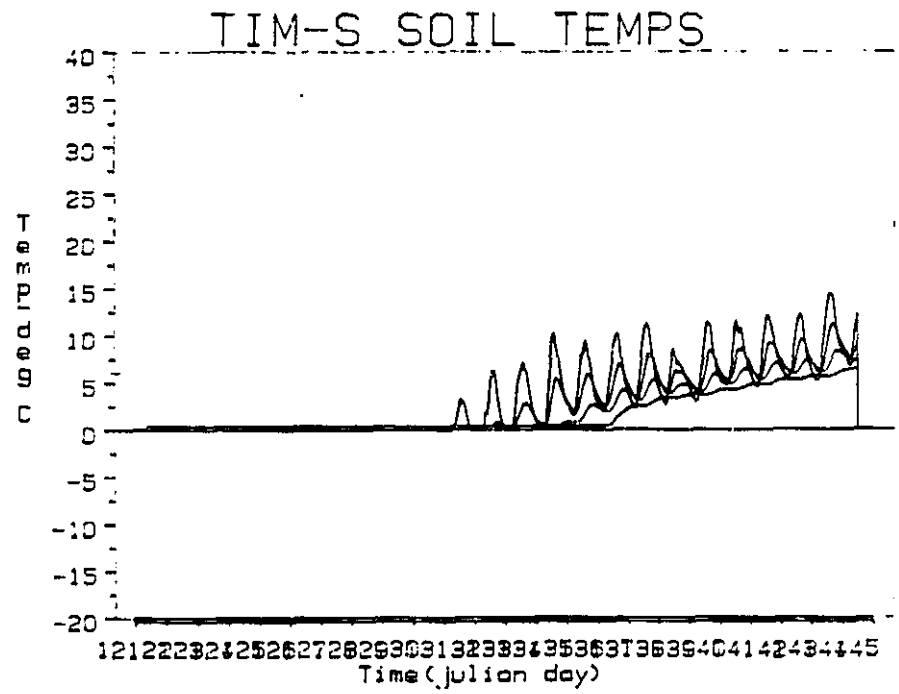

Figure 46b. Time series of soil temperature values at Pingree Park for JD 122-145.

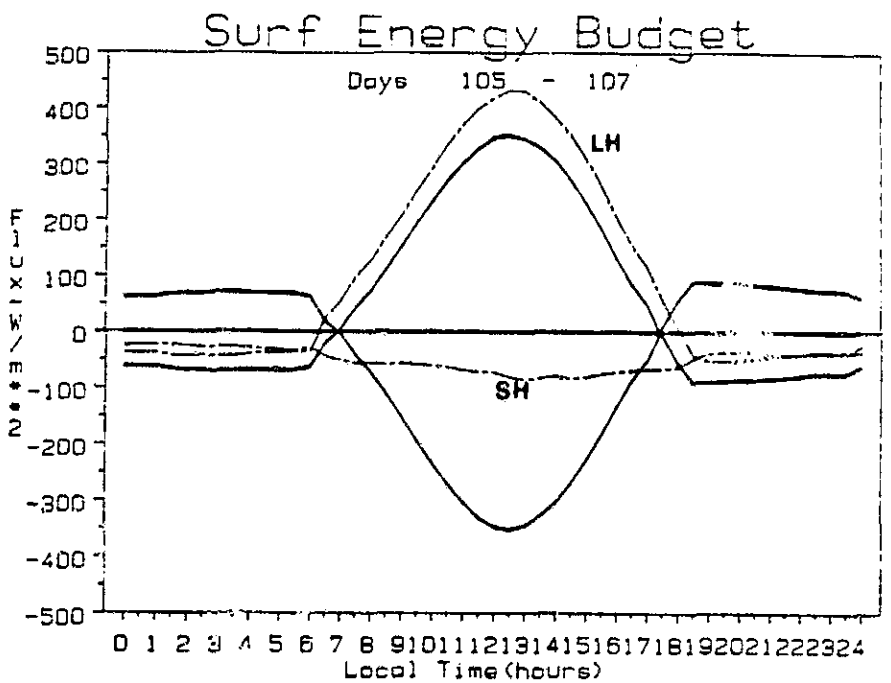

Figure 47a. Diurnal average of the surface energy budget at Pingree Park for JD 105-107.

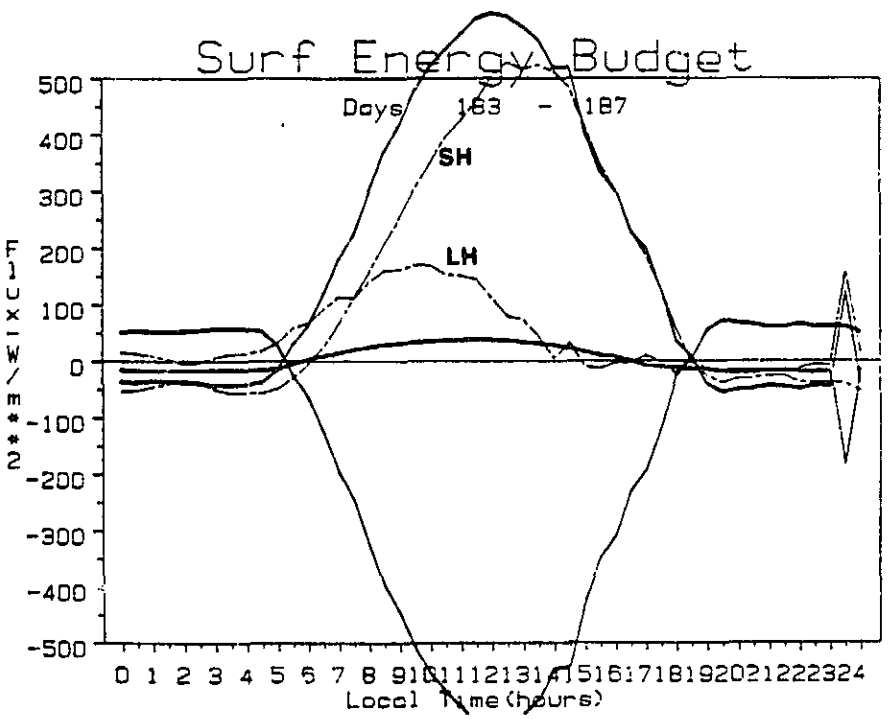

Figure 47b. As in Fig. 47a but for JD 183, 185 and 187.

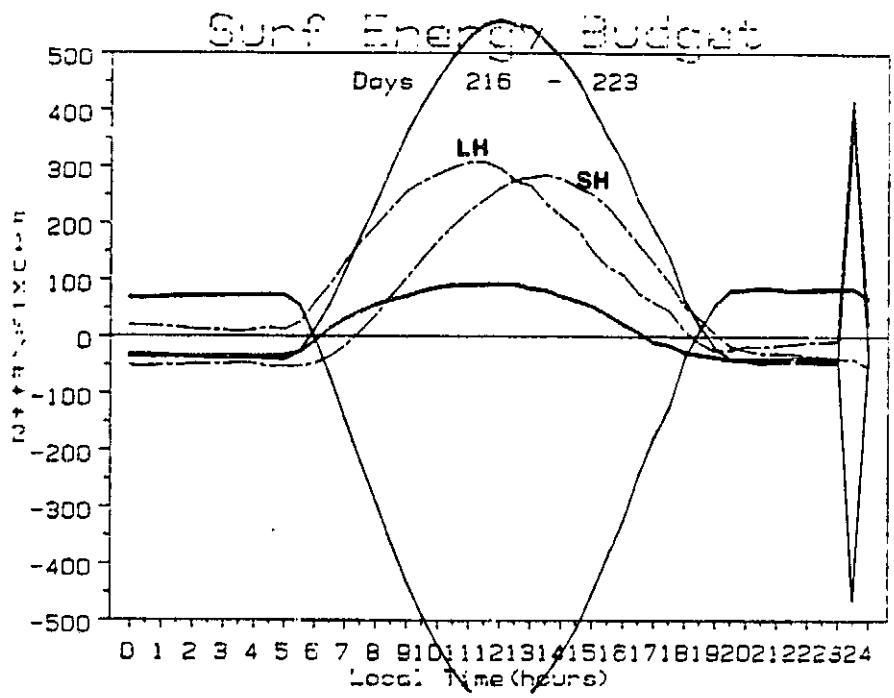

Figure 47c. As in Fig. 47a but at Storm Peak for JD 216, 221 and 223.

Longer-term diurnal averages of the summer fluxes for both sites, shown in Figs. 48 and 49, tend to confirm the representativeness of the values obtained for the cloud free days. The results for Pingree Park (Fig. 48) show little difference between the two averaging periods other than slightly diminished net fluxes for JD 172-180 due to greater cloudiness. The comparative periods for Storm Peak show distinct differences wherein the cumulative effects of a rainy spell during JD 225-240 lead to notably greater latent heat fluxes during the second part of the study (Fig. 49).

Another interesting trend was detected by this analysis for the May melt-off period described previously. In Fig. 50 we show the mean diurnal energy balance for JD 122-130 (with snow) and then for JD 130-139 (without snow). Although snow cover beneath the radiometer was completely gone by JD 131, the soil in the area was saturated with meltwater. Hence, the partitioning of energy between latent and sensible fluxes after JD 130 (Fig. 50b) is again at least a reasonable estimate of the likely integrated values for the site.

4.0 CRITIQUE OF THE ENERGY BALANCE MONITORING SYSTEM

In view of the results presented above, assessment of the performance of the system is straightforward. The system appears to be highly reliable and is at least adequate for the purposes intended. Also, operation of equipment of this sort in an exposed mountain top location during the convective season with no lightning damage is an important and perhaps fortuitous achievement.

a. Tower Station

The notable weakness of the observation programs was the failure of the eddy correlation measurements to obtain reasonable values for the

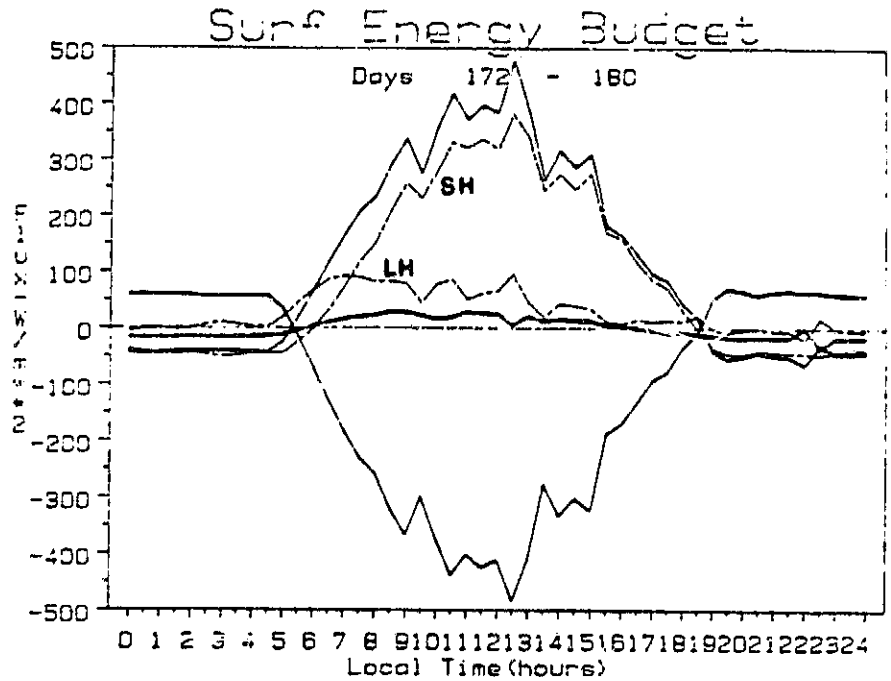

Figure 48a. Diurnal average of the surface energy budget at Pingree Park for JD 172-180.

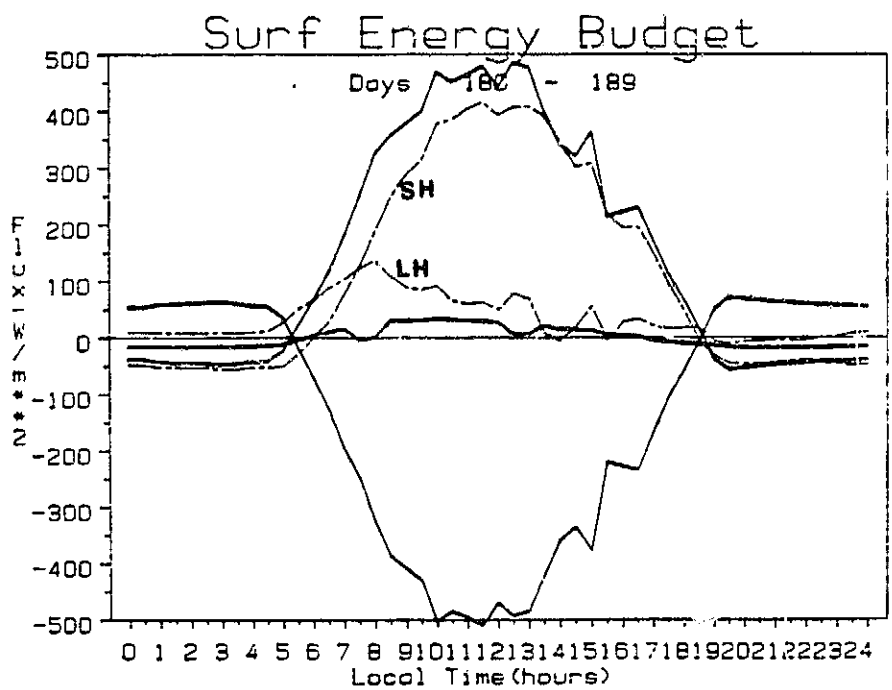

Figure 48b. As in Fig. 48a but for JD 180-189.

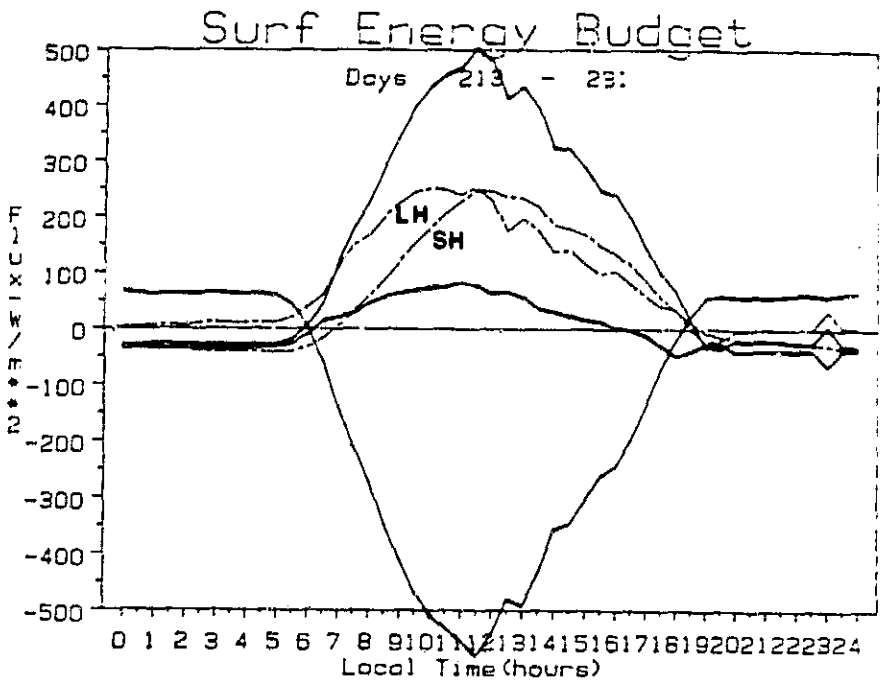

Figure 49a. Diurnal average of the surface energy budget at Storm Peak for JD 213-231.

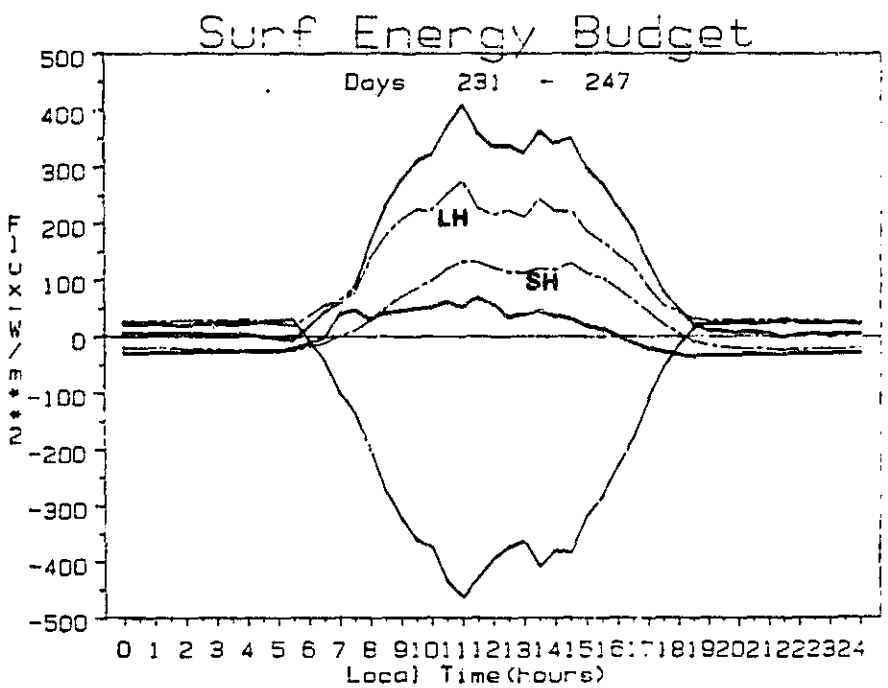

Figure 49b. As in Fig. 49a but for JD 231-247.

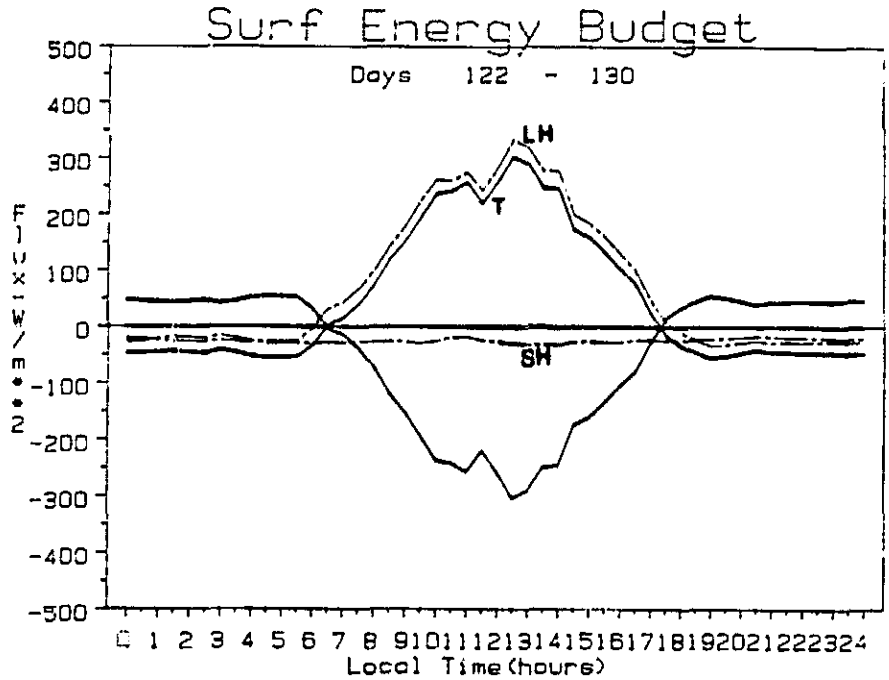

Figure 50a. Diurnal average of the surface energy budget at Pingree Park for JD 122-130.

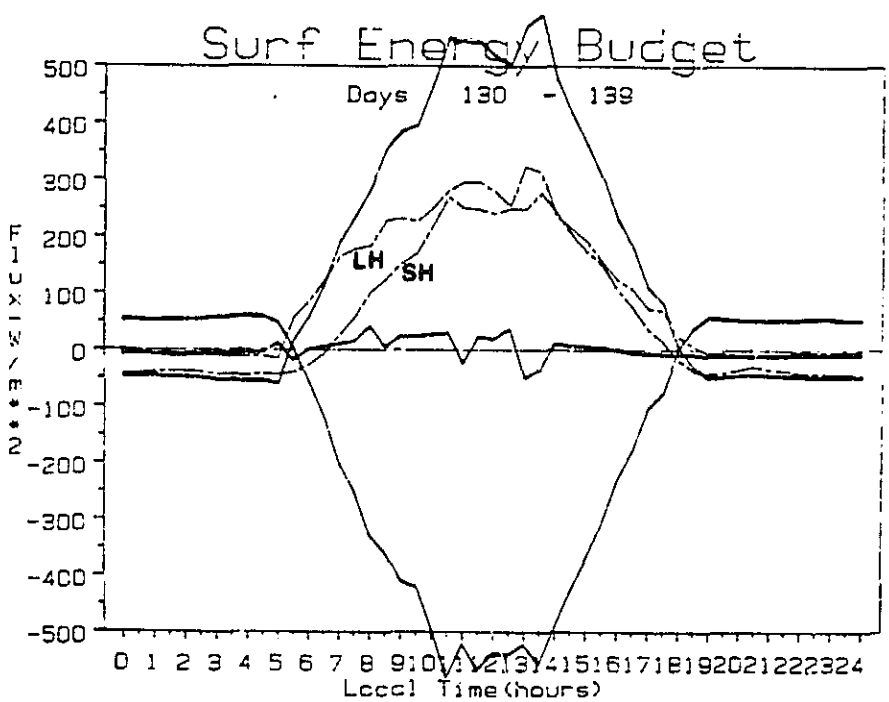

Figure 50b. As in Fig. 50a but for JD 130-139.

turbulent fluxes. Figure 51 shows the eddy correlation fluxes obtained for the cloud free (JD 183, 185 and 187) study at Pingree Park. These values are approximately one third and one tenth of the latent and sensible heat fluxes respectively, estimated by the residual method (Fig. 47b).

The difference in the comparative magnitudes of the apparent errors for sensible and latent heat provides an important clue as to the reasons for the failure of the turbulent flux measurements. Initially we feared that the problem was due primarily to a lack of sensitivity of the UVW wind monitors. However, aerodynamic damping and thermal inertia effects of the large aluminum housings for the temperature and humidity (T-q) sensors (see Fig. 29) were also suspected as being contributing factors. The problem, it appears, is due primarily to these shelters. Recently, during brief periods of favorable weather we have operated the system in a configuration such that temperature and humidity values from two separate sets of T-q sensors were correlated with wind fluctuations from a single set of wind sensors. One set of T-q sensors was housed in the same shelter configuration used for the previous experiments. The other set was attached directly to the wind instrument in such a way that it was protected from direct sunlight and surface infrared radiation but was otherwise completely exposed. The sensible and latent flux values for the exposed sensors were typically three to four times larger than those obtained for the sensors in the shelter (Fig. 52). The difference was due primarily to larger amplitudes for the T' and q' values of the exposed sensors. However, we suspect that having the T-q sensors closer to the anemometers also contributed to this difference in that the correlations as well as the covariances between w' and the T' and q' values were consistently stronger for the exposed sensors.

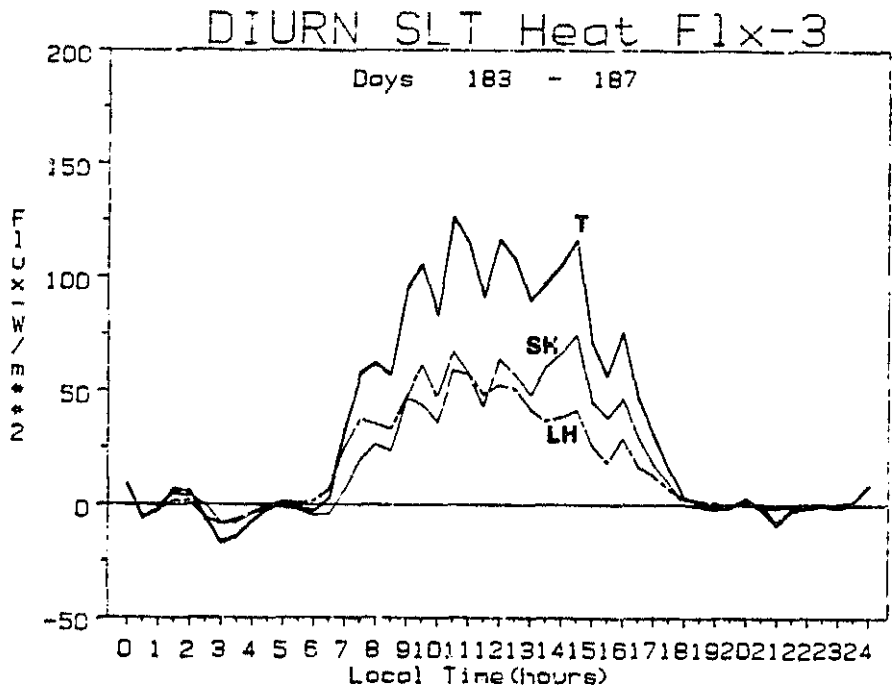

Figure 51. Diurnal average eddy correlation fluxes of sensible and latent heat measured at the top (eight meter) level of the tower at Pingree Park for JD 183, 185 and 187.

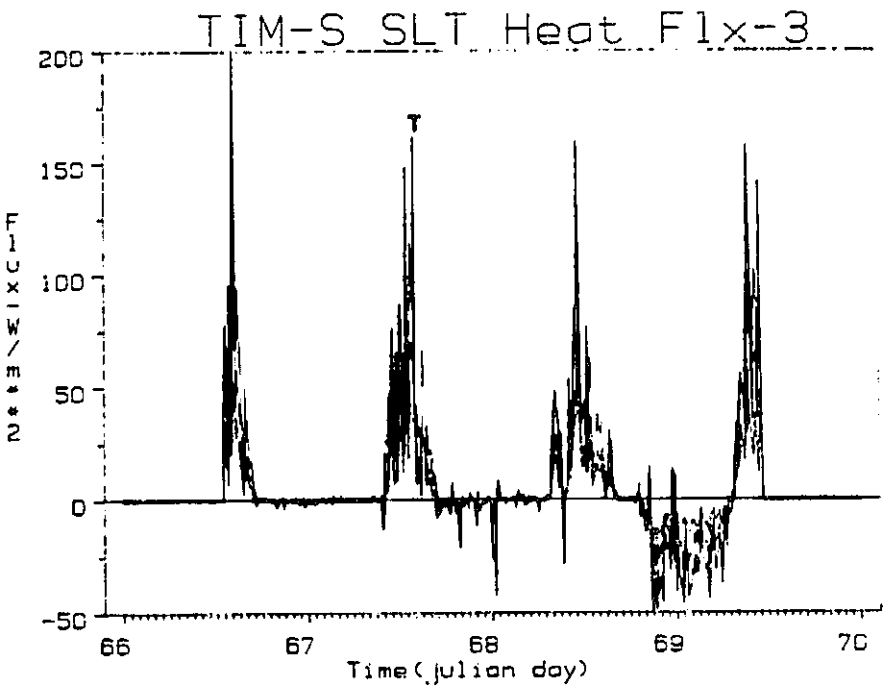

Figure 52a. Time series of "unsheltered" eddy correlation fluxes of sensible and latent heat.

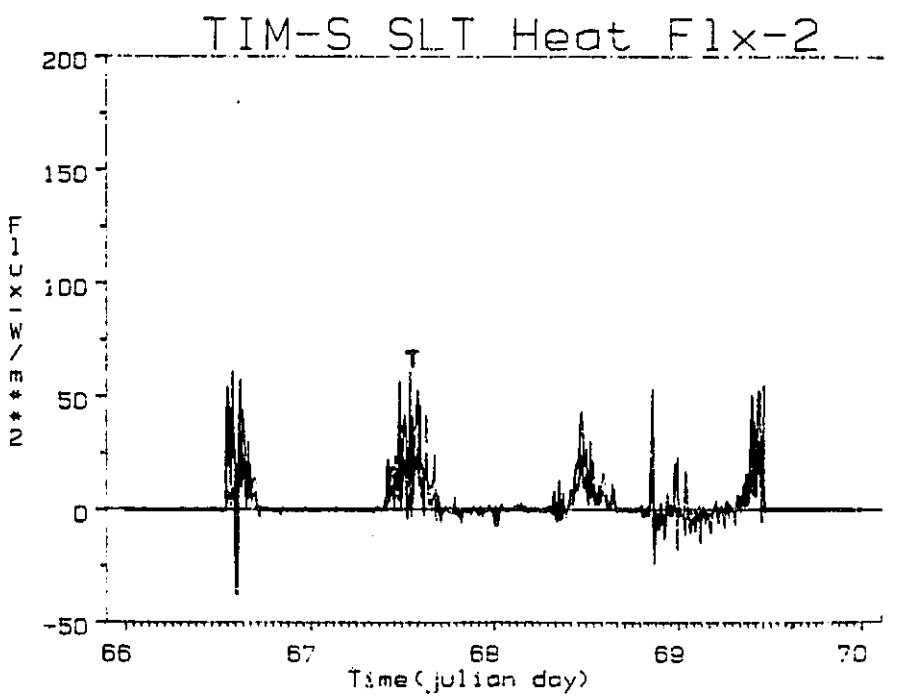

Figure 52b. As in Fig. 52a, using the same wind measurements but with the thermometer and hygristor in the shelters used during the monitoring experiments.

Allowing that conditions near the surface during these tests were rather dry, windy, and only slightly unstable, the near equality of the differences for both sensible and latent heat (i.e., four to one) for the two sensor configurations seems reasonable. We suspect that for highly unstable conditons, when the temperatures of transient thermal eddies differ sharply from the mean shelter temperatures, the comparatively larger difference between the sensible heat fluxes in Figs. 51 and 47b (i.e., ten to one) will be shown to be due to the additional effects of the thermal inertia of these shelters.

Several remedial actions have already been taken. We are testing alternative shelters for the T-q probes which are more open and have minimal thermal mass. These shelters, which will be attached directly to the wind monitors, are small and should cause little or no interference with the wind measurements.

It has become apparent that lack of sensitivity of the UVW wind sensors also contributed to the low turbulent flux values. In most cases the observed values for the turbulent fluxes increased systematically in going from the lowest level to the top of the tower. This difference was related to a systematic increase in the values obtained for w'. The Gill anemometers cannot detect the higher frequency components of wind spectra taken near the earth's surface. Hence, for the lower levels on our tower, a significant portion of the turbulent energy was not detected. To correct this problem we have acquired taller towers such that flux measurements will be made at 5, 10 and 20 meters rather than the prior levels of 2, 4 and 8 meters. In addition we intend to calibrate the tower flux system in a series of side-by-side studies at the nearby Boulder Atmospheric Observatory tower (operated by

the National Center for Atmospheric Research, near Boulder, CO) during April 1985.

Other changes in the tower observation program include the following: Instead of computing and storing the large number of derived parameters shown in Table 3 we intend to simply record the raw data values (at least for key observation programs). Although this will require more frequent site visits to change data cassettes, acquisition of such data will allow after the fact analysis of turbulent spectra, variable averaging times, and calculation of additional turbulent parameters. The latter include advection terms such as $\overline{u'T'}$ and $\overline{u'q'}$ which, in view of the inhomogeneous surroundings of most of our monitoring sites, will be most useful. In addition, correction of wind data for minor misalignments of the sensors and estimating fluxes parallel and vertical to the surface on sloping terrain can be done more adequately with raw data.

b. Radiation Station

We anticipate one minor change to the radiation station. This involves the addition of two temperature soil probes to allow better estimates of the soil heat fluxes.

References

Businger, J.A., 1973: Turbulent transfer in the atmospheric surface layer. In: Workshop in Micrometeorology, Am. Meteorol. Soc., Boston, Mass.

De Bruin, H.A.R. and A.A.M. Holtslag, 1982: A simple parameterization of surface fluxes of sensible and latent heat during daytime compared with the Penman-Monteith concept. J. Appl. Meteorol., 21: 1610-1621.

Kondratyev, K. Ya, 1969: Radiation in the Atmosphere. Academic Press, New York.

Kondratyev, K. Ya., V.I. Korzov, V.V. Mukhenberg and L.N. Dyachenko, 1982: The short-wave albedo and the surface emissivity. In: Land Surface Processes in Atmospheric General Circulation Models. P.S. Eagleson, ed. Cambridge University Press.

McClatchey, R.A., R.W. Fenn, J.E. Selby, F.E. Volz and J.S. Garing, 1971: Optical properties of the atmosphere. Air Force Cambridge Research Laboratories. Bedford, Mass.

Pielke, R.A., 1984: Mesoscale Meteorological Modeling. Academic Press, New York.

Priestly, C.H.B. and R.J. Taylor, 1972: On the assessment of surface heat flux and evaporation using large-scale parameters. Mon. Wea. Rev., 100:81-92.

Reiter, E.R. and M. Tang, 1984: Plateau effects on diurnal circulation patterns. Mon. Wea. Rev., 112:638-651.

APPENDIX A

INSTRUMENTATION AND DATA COLLECTION PROCEDURES

A.1 THE RADIATION STATION

The sensor package the Radiation System consists of the following:

1. Two (upward and downward looking) Eppley Precision Spectral Pyranometers (PSP) with WG-295 quartz outer and inner hemispheres for broadband (0.2-4.0 μm) solar radiation monitoring,
2. Two (upward and downward looking) Eppley Precision Spectral Pyranometers (PSP) with R68 Schott colored glass outer hemispheres and WG-295 quartz inner hemispheres for near-infrared (0.7-4.0 μm) solar radiation monitoring,
3. Two (upward and downward looking) Eppley Precision Infrared Radiometers (PIR) with silicon domes and dome-sink calibrating thermistors for broadband (2.0-50.0 μm) terrestrial radiation monitoring,
4. A CSI temperature-relative humidity probe (thermistor/hygristor element) enclosed in a radiation shelter for ambient state parameter monitoring,
5. A CSI cup anemometer and wind vane pair for ambient wind monitoring,
6. A set of 4 CSI soil temperature probes (thermistors) for subsurface heat storage monitoring,
7. A set of 4 CSI soil moisture blocks for subsurface soil moisture storage monitoring, and
8. A tipping rain gauge for ambient precipitation monitoring.

All of the above sensors operate in a transducive mode in conjunction with a CSI CR-7 data logger control module. The sensors are individually wired through detachable cable couplers to the CR-7 analog input interface. The CR-7 control module, in conjunction with an excitation card, then provide the necessary impulses along the transducer circuits at a sampling interval selected by the station operator. The control module incorporates arithmetic registers and a digital memory to which statistical compilations of the raw data samples are sent at every integration time step. The integration time steps for each individual sensor are programmable and selectable by the station operator just as the impulse sampling time is programmable and selectable.

The CR-7 programming panel is easily accessed, simple to operate (16 keys), and includes a powerful software capability which enables the insertion of calibration factors, statistical transforms, and a variety of interrogation and display-readout procedures such that the final data products are processed and recorded in the preferred physical units and in reduced statistical form (e.g. means, variances, standard deviations, minimum-maximum values). These features are important because they allow on-site, real-time interrogation of the direct sensor outputs and derived parameters in the conventional physical units to which we are accustomed and provide a means to initiate scientific analysis in the field immediately (requiring only a six-pound cassette tape playback printer).

To those who have worked in the field, the latter point is especially important if the experimental design is still in a state of flux. Since the sampling times, integration times, calibration constants and derived parameters are all under operator control through the programming panel, a few minutes spent plotting up actual data may

motivate making corrections or improvements to the data processing or sensor deployment configurations. Of course, if the field scientist is so inclined, there is nothing to prevent carrying along more powerful data analysis systems such as the now popular inexpensive microcomputer systems incorporating disk packs, CRT displays, and hard copy printers and plotters.

The Radiation Station is easy to assemble and disassemble and can be deployed by two people in approximately one and one-half hours with a minimum of tools. The total system which includes sensors, data logging and recording electronics, cabling, frame members, mounting brackets, wires, ground supports, setup tools, expendables, the solar panel, and a fiberglass enclosure for environmentally sealing the data logger can all be placed in three standard size military footlockers (the frame members break down into 3-foot sections) for easy transport. The transport issue should not be dispensed with lightly if one is considering making measurements in difficult environments.

Maintenance of the system is trivial. The upward radiometer domes require periodic cleaning if "sticky" air pollutants are present. Cassette tapes require replacement after a length of time which is mostly dictated by the selected integration-output interval and total number of derived parameters. Integration times of on the order of 30 minutes allow for up to two months of data recording on a single 60 minute cassette tape. Finally, the battery packs need to be rigorously recharged from wall power every 2 or 3 months (more frequently if cloudiness is excessive). The only nuisance factor in maintaining the system is the fact that the soil moisture blocks have limited lifetimes, particularly in silty soils and must be replaced periodically (1-6 months).

The system is not designed for extreme wintertime conditions, particularly in the presence of glaze or rime ice. However, system degradation is not total under icing conditions; only the hygristor elements and the rain gauge are incapacitated. The hygristor elements are effectively destroyed by undergoing a freeze-thaw cycle. The radiometers, of course, become ineffective if ice would adhere to any portion of the domes.

The Radiation Station is designed to retrieve:

I) The full complement of the radiative exchange terms, i.e.

1) Upward and downward UV-VIS, near-IR, and broadband ($K\uparrow$, $K\downarrow$) solar fluxes,

2) Surface reflectance in the UV-VIS, near-IR, and broadband spectrums,

3) Upward and downward broadband ($L\uparrow$, $L\downarrow$) fluxes and equivalent flux temperatures,

4) UV-VIS, near-IR, broadband solar, and broadband IR net fluxes, and

5) Total radiative net flux (Q) at the surface which is a principal term in the surface heat exchange equation:

$$Q = K\downarrow - K\uparrow + L\downarrow - L\uparrow \qquad (1)$$

II) The subsurface heat storage term (S) which is obtained from an integration process:

$$S = c_s \cdot \bar{\rho}_s \int_{d_o}^{o} \frac{dT(z,t)}{dt}\, dz \qquad (2)$$

in which c_s is the heat capacity of the soil, and $\bar{\rho}_s$ is the mean soil density. A temperature function [T(z,t)] is developed by fitting the

subsurface thermistor data with a wave-like function. The lower limit of integration (d_o) is defined to be that level at which there are no discernable temperature waves or trends with respect to the time scale of investigation.

III) The subsurface moisture storage term (SM) which is used to diagnose the surface evaporation (E) and thus the latent heat (LH) exchange:

$$E = - \frac{dSM}{dt}$$

$$LH = \ddot{\rho}_s \cdot L \cdot E \qquad (3)$$

in which L is the latent heat of evaporation.

IV) The sensible heat term (SH) which is diagnosed from I, II, and III above

$$SH = Q - S - LH \qquad (4)$$

V) A measure of the total rainfall (R) which is a useful parameter in land surface studies for its own sake and, in addition, for providing an independent but qualitative check on the soil moisture monitors. There is not a direct relationship between SM and R, i.e.

$$R \neq \frac{dSM}{dt} \qquad (5)$$

because of horizontal surface transport (runoff) and subsurface transport (percolation) processes.

VI) Finally, measures of the ambient air temperature (T), relative humidity (RH), and wind ($\vec{V}$) conditions which are used in conjunction with the radiation and rainfall parameters to interpret the changes and discontinuities taking place in the energy budget process and needed in surface flux parameterization formulations.

A.2 THE TOWER STATION

The second part of the surface energy budget system is the Tower Station. This component of the system is designed to monitor temperature, moisture, and winds at four levels, as indicated in Fig. 2 (winds are measured at three levels, but not directly at the surface). The electronics module on the Tower Station (another CR-7) has a specially prepared "firmware" card, a programmable read only memory (PROM), which is designed to operate as an eddy flux processor. That is, it compiles sums, sums of squares, and sums of cross products used in the calculation of variance-covariance and correlation matrices at each of the three upper levels. These matrices are the essential ingredient in the computation of the eddy heat, moisture, and momentum fluxes. In addition, mean values are collected at all four levels.

As with the Radiation Station, the sampling times and integration times are operator selectable. The integration time can be thought of as the bar operator in, for example, the expression for vertical heat flux $\rho c_p \langle \overline{w'T'} \rangle$. The eddy flux module for the CR-7 was specifically prepared by Campbell Scientific Inc. based on our own design specifications. In the present configuration, the software overhead required during a sampling interval limits the maximum sampling rate to once per second. We have done studies to show that this sampling resolution does not appear to present any problems in resolving the turbulent heat exchange process.

The sensor package on a Tower Station consists of the following:

1) Three sets of R.M. Young Inc. u-v-w low threshold propeller anemometers mounted at 2, 4, and 8 meters.

2) A set of 4 CSI temperature-specific humidity probes (thermistor/hygristor elements) enclosed in metallic radiation shelters coated with a glossy white paint. These units are mounted at 0.2, 2, 4, and 8 meters. The tower has been designed such that the T-q probes can be aligned at 60°, 120°, or 180° angles with respect to the anemometers. With this sensor configuration and the capabilities of the eddy flux software module, the following parameters are then calculated at the upper three levels:

   1) Means, variances, and standard deviations of T, q, u, v, and w,

   2) A five-way variance-covariance matrix including the heat and moisture variances ($\overline{T'^2}$, $\overline{q'^2}$), the eddy heat and moisture flux terms ($\overline{w'T'}$, $\overline{w'q'}$), and the components of a Reynolds matrix ($\overline{u'^2}$, $\overline{v'^2}$, $\overline{w'^2}$, $\overline{u'v'}$, $\overline{u'w'}$, $\overline{v'w'}$). The associated correlation matrix is also calculated. The horizontal heat and moisture flux terms are not calculated by the processor.

In addition the means, variances, and standard deviations of T and q are calculated at the near-surface level.

The deployment of this system is relatively simple and straightforward (setup time is approximately three hours for two people). All of the equipment can be placed in three footlockers with the exception of the tower itself which breaks down into three 10-foot sections. A CSI solar panel is used to recharge the data logger and recording electronics battery pack. The only maintenance requirements are the removal of the styrofoam anemometer propellers in excessively high winds, and

the periodic rigorous recharging of the electronics battery pack. As in the case of the Radiation Station, the Tower Station has not been designed for icy and snowy conditions which render the anemometers and hygristors useless.

As with the Radiation Station, the sensors are simple, inexpensive, and as a result are not expected to achieve maximum precision. In particular the hygristor elements used on the tower have relatively slow response times in comparison with state-of-the-art technology. Therefore, we do not expect that the direct measures of vertical moisture flux will be extremely accurate.

A.3 SIMULTANEOUS USE OF THE TWO STATIONS

The two stations used in tandom have been designed to have the capability to monitor the sensible and latent heat fluxes in three independent modes. The Radiation Station, because it does an excellent job of monitoring the radiation budget, is able to produce by the residual method (mode 1), the sensible and latent heat terms whose accuracy is dictated by uncertainties in calculating subsurface heat and moisture storage. There are uncertainties due both to limited vertical resolution [4 levels] and sensor inaccuracies [e.g. the soil moisture blocks, even when used under optimum conditions, are known to yield uncertainties on the order of 25 percent].

The Tower Station, on the other hand, provides the direct measurement method (mode 2) of $\langle\overline{w'T'}\rangle$ and $\langle\overline{w'q'}\rangle$. There are also uncertainties in these measurements. The anemometers, thermistors, and hygristors are not instantaneous response detectors; their response times are on the order of the maximum allowable sampling time (1 second) and longer and the different times are not necessarily consistent.

However, the Tower Station provides excellent measures of $\bar{T}$ and $\bar{q}$ at four levels and direct measurements of $\overline{w'u'}$, $\overline{w'v'}$ and $\overline{w'^2}$ at three levels (there are, of course, uncertainties in these covariance and variance terms because the anemometer response times are finite). These measures thus provide a means to apply <u>similarity theory</u> (mode 3) within the constant flux layer which avoids any direct measure of $\langle\overline{w'T'}\rangle$ and $\langle\overline{w'q'}\rangle$. For instance, in the case of the eddy heat flux (F_H) for a non-neutral stratified surface layer (i.e., bouyant production):

$$F_H = c_p \bar{\rho}_o \overline{w'T'} = c_p \cdot \ddot{\rho}_o U^*T^* \qquad (6)$$

where

$$U^* = (\overline{v'w'})^{\frac{1}{2}} \qquad \text{for forced convection} \qquad (7)$$

$$\doteq (\overline{w'^2}/1.35)^{\frac{1}{2}} \qquad \text{for free convection}$$

and T^* can be diagnosed iteratively from:

$$T^* = (\bar{T} - \bar{T}_o)/F_t(\xi, z_o, z) \qquad (8)$$

where for the stable case ($\xi \geq 0$):

$$F_t = (0.74/k)\cdot[\ell n(z/z_o) - \Psi_H(\xi)]$$
$$\Psi_H(\xi) = 1 - \phi_H/0.74 \qquad (9)$$
$$\phi_H = 0.74(1 + 6.35\xi)$$

and for the unstable case ($\xi < 0$):

$$F_t = (0.74/k) \cdot [\ell n(z/z_o) - \Psi_H(\xi)]$$
$$\Psi_H(\xi) = \ell n[(1+0.74\cdot\phi_H^{-1})/2] \qquad (10)$$
$$\phi_H = 0.74\cdot(1-9\xi)^{-\frac{1}{2}}$$

and the Monin-Obukhov stability parameter (ξ) is given by:

$$\xi = - z/L = - g \cdot k \cdot (z+z_o) \overline{w'T'}/(\theta_o \cdot U^{*3}) \qquad (11)$$

In the above expressions, z is height, U* and T* are the friction velocity and scaling or flux temperature; z_o is the roughness length, ($\simeq$0.03 - 1.0 cm for bare soils and tundra) where:

$$\begin{aligned} \bar{V}(z) &= \frac{U^*}{k} [\ell n(z/z_o)] \qquad \text{for neutral case} \\ &= \frac{U^*}{k} [\ell n(z/z_o) - \Psi_m(\xi)] \text{ for stratified case} \end{aligned} \qquad (12)$$

and

$$\begin{aligned} \Psi_m(\xi) &= 1 - \phi_m \qquad \text{for } \xi \geq 0 \\ &= 2\, \ell n[(1 + \phi_m^{-1})/2] + \ell n[(1 + \phi_m^{-2})/2] \\ &\quad - 2 \tan^{-1} [\phi_m^{-1} + \pi/2] \qquad \text{for } \xi < 0 \end{aligned} \qquad (13)$$

$$\begin{aligned} \phi_m &= 1 + 4.7\xi \qquad \text{for } \xi \geq 0 \\ &= (1 - 15\xi)^{-\frac{1}{4}} \qquad \text{for } \xi < 0 \end{aligned} \qquad (14)$$

and T_o and $\bar{T}$ are the mean temperatures at z_o and z, respectively; θ_o is the potential temperature at the top of the transition layer; k is von Kármáns constant ($\simeq$ 0.35); and [F_t, Ψ_H, Ψ_m], ϕ_H, ϕ_m and L are Paulson's expressions, the nondimensional temperature gradient, the nondimensional wind shear, and the Obukhov length respectively [see Businger (1973) or Pielke (1984) for a discussion of the above formulations].

This three-mode approach to estimate the critically important vertical transports of sensible and latent heat allow a variety of permutations in cross-checking and intercomparison to arrive at the best possible estimates of surface storage and heat-moisture conduction.

Additionally, we have a fourth option of using, and independently assessing, either simplified techniques such as the bulk aerodynamic

C - 2

method (i.e. drag coefficient theory) or parameterization techniques such as the Priestley and Taylor (1972) model. In drag theory, surface sensible and latent heat terms are approximated by:

$$SH = C_D \cdot \rho \cdot c_p \cdot \bar{U}(T_s - T) \tag{15}$$

$$LH = C_D' \cdot \rho \cdot L \cdot \bar{U}(q_s - q)$$

where C_D and C_D' are empirical heat and moisture drag coefficients, $\bar{U}$ is the mean surface wind, and the difference terms in parentheses are the surface-air gradients of temperature and moisture directly at the surface. It is noted that over land surfaces, a moisture drag coefficient is best formulated in terms of a soil moisture factor (M) and a surface resistance term R_q such that $C_D' \cdot \bar{U} = M/R_q$. In the Priestley and Taylor (1972) method, only the net radiation term, air temperature, and the empirical coefficient related to surface moisture are used to estimate SH and LH; see DeBruin and Holtslag (1982):

$$SH = [\alpha(M) \cdot g(T)] \cdot [0.9 \cdot Q^*] \tag{16}$$

$$LH = [1 - \alpha(M) \cdot g(T)] \cdot [0.9 \cdot Q^*]$$

where $\alpha(M)$ is an empirical coefficient related to M and g(T) is related to the slope of the saturation-vapour-pressure/temperature curve.